

Chapter 3: Ocean case studies with socio-economic relevance

Section 3.1. Potential eutrophication of European waters using satellite derived chlorophyll following the UN Sustainable Development Goal 14 framework

Authors: Vittorio E. Brando, Silvia Pardo, Shubha Sathyendranath, Ben Howey, Peter Land, Thomas Jackson, Rosalia Santoleri, Michela Sammartino, Simone Colella, Karina von Schuckmann, Dany Ghafari, Emily Smail, Keith VanGraafeiland, Sathyadev Ramachandran, Veronica P. Lance, and Menghua Wang

Statement of main outcome: This section presents a satellite-based map of potential eutrophic and oligotrophic areas in the European Seas for the year 2020, together with time series of potential eutrophication in the past 23 years (1998–2020) averaged over Exclusive Economic Zones (EEZs) of each European country. The map and time series of potential eutrophication were generated on the basis of a comparison of the per-pixel chlorophyll-a data from remote sensing in the reporting year with the corresponding chlorophyll-a climatological 90th percentile (P90) established for a 20-year baseline (1998–2017). The results showed few scattered potential eutrophic areas, while extensive coastal and shelf waters indicate a potential oligotrophic status. The distributions point to localities that should be on a watch to determine the in situ nutrient levels and whether the chlorophyll-a trend is sustained into the future. The time series of the potential eutrophication at the EEZ level showed low percentages across the area with some remarkable high potential eutrophic events occurring in the first decade of the study period, followed by an overall reduction in potential eutrophication from 2013 onwards. Furthermore, for several European countries, the eutrophication indicator at the EEZ level was often nil or never exceeded 1% of the EEZ area. Results are then compared with those from the Sustainable Development Goal (SDG, set by the United Nations General Assembly) 14 global satellite-derived eutrophication indicator (target 14.1).

Products used:

Ref. No.	Product name and type	Documentation
3.1.1	ATL OC-CCI REP dataset OCEANCOLOUR_ATL_CHL_L3_REP_OBSERVATIONS_009_067	PUM: http://marine.copernicus.eu/documents/PUM/CMEMS-OC-PUM-009-ALL.pdf QUID: http://marine.copernicus.eu/documents/QUID/CMEMS-OC-QUID-009-066-067-068-069-088-091.pdf
3.1.2	ARC REP dataset OCEANCOLOUR_ARC_CHL_L3_REP_OBSERVATIONS_009_069	PUM: http://marine.copernicus.eu/documents/PUM/CMEMS-OC-PUM-009-ALL.pdf QUID: http://marine.copernicus.eu/documents/QUID/CMEMS-OC-QUID-009-066-067-068-069-088-091.pdf
3.1.3	MED OC REP dataset OCEANCOLOUR_MED_CHL_L3_REP_OBSERVATIONS_009_073	PUM: http://marine.copernicus.eu/documents/PUM/CMEMS-OC-PUM-009-ALL.pdf QUID: https://catalogue.marine.copernicus.eu/documents/QUID/CMEMS-OC-QUID-009-038to045-071-073-078-079-095-096.pdf
3.1.4	BS OC REP dataset OCEANCOLOUR_BS_CHL_L3_REP_OBSERVATIONS_009_071	PUM: http://marine.copernicus.eu/documents/PUM/CMEMS-OC-PUM-009-ALL.pdf QUID: https://catalogue.marine.copernicus.eu/documents/QUID/CMEMS-OC-QUID-009-038to045-071-073-078-079-095-096.pdf
3.1.5	BAL OC REP dataset OCEANCOLOUR_BAL_CHL_L3_REP_OBSERVATIONS_009_080	PUM: http://marine.copernicus.eu/documents/PUM/CMEMS-OC-PUM-009-ALL.pdf QUID: https://catalogue.marine.copernicus.eu/

(Continued)

Continued.

Ref. No.	Product name and type	Documentation
3.1.6	GLO OC REP dataset OCEANCOLOUR_GLO_CHL_L3_REP_OBSERVATIONS_009_065	documents/QUID/CMEMS-OC-QUID-009-080-097.pdf PUM: http://marine.copernicus.eu/documents/PUM/CMEMS-OC-PUM-009-ALL.pdf QUID: https://catalogue.marine.copernicus.eu/documents/QUID/CMEMS-OC-QUID-009-064-065-093.pdf

3.1.1. Introduction

Since the term eutrophication was first introduced in the middle of the twentieth century by Hutchinson (1969), its definition and interpretation have evolved with time (Karydis and Kitsiou 2019; Malone and Newton 2020). At present, cultural eutrophication is understood to be a process (and not a state) by which ‘increases in the supply of organic matter to an ecosystem that is fuelled by anthropogenic inputs of inorganic nutrients where increases in organic matter are most often due to excess phytoplankton production’, as recently defined by Malone and Newton (2020) elaborating and constraining the archetypal Nixon (1995) definition.

Anthropogenic activities, such as farming, agriculture, aquaculture, industry and sewage discharge, are the main sources of excess nutrient input in problem areas (Jickells 1998; Schindler 2006; Galloway et al. 2008). Eutrophication is an issue particularly in coastal marine ecosystems (Malone and Newton 2020) as well as estuaries, lakes and rivers (Smith 2003; Howarth and Marino 2006). The impact of eutrophication on aquatic ecosystems is well known: nutrient availability boosts plant growth – particularly algal blooms – resulting in a decrease in water quality (Howarth et al. 2000; Anderson et al. 2002). This can, in turn, cause death by hypoxia of aquatic organisms (Breitburg et al. 2018), ultimately driving changes in community composition (Van Meerssche and Pinckney 2019) or overall decrease in the biomass that the system can support. Eutrophication has also been linked to changes in sea water pH (Cai et al. 2011; Wallace et al. 2014) and depletion of dissolved inorganic carbon in the aquatic environment (Balmer and Downing 2011). Oligotrophication, the opposite of eutrophication, occurs where reduction in some limiting resource leads to a decrease in photosynthesis by aquatic plants,

which might in turn reduce the capacity of the ecosystem to sustain plants and higher organisms in it (Duarte et al. 2013; Williams et al. 2013; Agusti et al. 2017).

In Europe, eutrophication has been recognised as one of the problems to be addressed to improve water quality (e.g. OSPAR ICG-EUT 2017; Carvalho et al. 2019; EEA 2019a, 2019b). Various international conventions (e.g. OSPAR, Helsinki and Barcelona Conventions) and commissions (e.g. HELCOM) also highlight the importance of monitoring the ecological status of aquatic systems to enforce water directives, and the eutrophication status is one of the most basic properties to monitor over a long time series to quantify changes in water quality.

Whereas many methods and indices have been proposed to measure eutrophication, most methods adopt chlorophyll-a concentration by itself, or in combination with other variables, to estimate eutrophication (Anderson et al. 2017; Karydis and Kitsiou 2019). As a measure of phytoplankton biomass, the concentration of the pigment chlorophyll-a is one of the most commonly measured biological quantities in aquatic bodies, whether it be from in situ sampling methods or from satellite observations (Sathyendranath et al. 2019, 2020). If excess inorganic nutrients are delivered to a water body, any effect that might have on the ecosystem is likely to manifest itself first and foremost as an increase in phytoplankton abundance, and hence in chlorophyll-a concentration.

For European seas, long-term spatial and temporal trends of eutrophication of the Baltic Sea for the period 1901–2012 based on HEAT+ and a broad range of in situ-measured indicators are provided by Anderson et al. (2017). This approach was then extended for the first integrated assessment of the eutrophication status in Europe’s seas (EEA 2019b). However, due to the low spatial coverage of in situ data, especially in the Mediterranean Sea and the Black Sea, a fully harmonised multi-metric indicator-based eutrophication assessment tool occurred only in the Baltic Sea. Hence, the extent of problem areas is likely to be underestimated using only in situ data, especially in the Mediterranean Sea and the Black Sea.

Remotely sensed ocean colour data have been exploited to assess the potential eutrophication status of European regional seas (e.g. Gohin et al. 2008, 2019; Coppini et al. 2012; Cristina et al. 2015; Harvey et al. 2015; Attila et al. 2018) and global waters (Maúre et al. 2021). Most of the eutrophication studies cited

above use percentile-derived thresholds to classify water bodies according to their ecological status and emphasise the need for well-validated, high-quality satellite chlorophyll-a datasets (Baretta-Bekker et al. 2015; Van der Zande et al. 2019). Furthermore, following Maúre et al. (2021), the use of the term potential eutrophication is adopted in this study to refer to methods adopting only chlorophyll-a concentration by itself.

Monitoring eutrophication on a regular basis has recently become a responsibility of member states within the United Nations. The Sustainable Development Goal 14 (life below water), includes a target, 14.1 that aims ‘by 2025, prevent and significantly reduce marine pollution of all kinds, in particular from land-based activities, including marine debris and nutrient pollution’. The indicator for this target is broken into two components: 14.1.1a ‘Index of Coastal Eutrophication (including ICEP)’ and the Indicator 14.1.1.b ‘Marine plastic debris’ (UNEP 2021). As the custodian agency for indicator 14.1.1a, UNEP published a report titled ‘Understanding the state of the ocean: a global manual on measuring SDG 14.1.1, SDG 14.2.1 and SDG 14.5.1’ to provide guidance on monitoring techniques and data for these indicators

(UNEP 2021). The methodology for reporting on indicator 14.1.1a outlined by UNEP uses a progressive monitoring approach with three levels based on both globally and nationally derived data and supplemental data to report on SDG indicators (Figure 3.1.1) (UNEP 2021).

Level 1 sub-indicators utilise globally available data products and consist of a modelled indicator, the ‘Indicator for Coastal Eutrophication Potential (ICEP)’, and two remote sensing-based indicators, ‘Chlorophyll-a deviations and anomalies’ (UNEP 2021). The ICEP provides a modelled number indicating the risk of coastal eutrophication at a specific river mouth based on a global level analysis of basin level nutrient exports (total nitrogen, total phosphorus and dissolved silica) to river-mouths (Seitzinger and Mayorga 2016; UNEP 2021). Then, for Level 2 reporting, national level measurements of chlorophyll-a and other parameters (either in situ or satellite-derived) complement the global remote sensing and modelled data used in Level 1 to enable a more detailed assessment of eutrophication (UNEP 2021). Within UNEP SDG reporting context, eutrophication is defined as ‘excess nutrient loading into coastal environments from anthropogenic sources, resulting in excessive growth of aquatic plants, algae

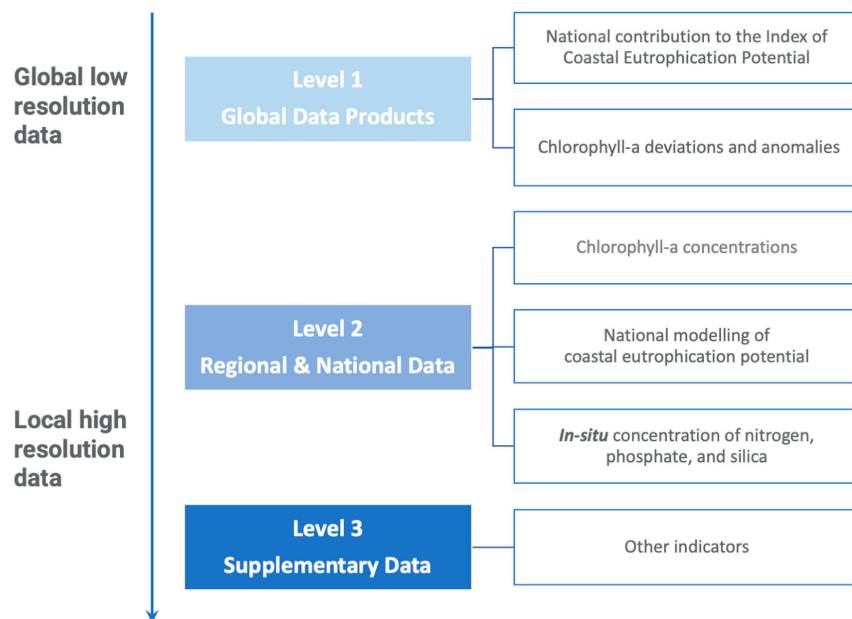


Figure 3.1.1. Summary of SDG 14.1.1a sub-indicators (reproduced with small modifications from UNEP 2021).

and phytoplankton', hence reformulating the Malone and Newton (2020) and the Nixon (1995) definitions. Furthermore, the Coastal Zone refers to 'national Exclusive Economic Zone (EEZ) (200 nautical miles from the coast) as outlined by the United Nations Convention on the Law of the Sea'.

This work presents a method to supplement the SDG reporting for 14.1.1a Level 2 sub-indicator chlorophyll-a concentration for European countries in a harmonised, consistent and integrated manner. By using satellite-derived chlorophyll-a data to generate a single variable indicator, we circumvent an issue related to the lack of sufficient data that has plagued previous reporting attempts for European seas (EEA 2019b) and global waters (Estoque 2020; Alamanos and Linnane 2021; Maúre et al. 2021). A time series of global daily satellite observations at 1 km resolution extending from 1997 to 2020 (product references 3.1.1 to 3.1.6) minimises temporal and spatial biases in the reporting of coastal eutrophication.

The need for high spatial and temporal monitoring necessitates the use of satellite data to provide a synoptic view. This fundamental requirement underpins our choice of method as well as the one recently adopted by UNEP (Anderson et al. 2017; Masó et al. 2020; Alamanos and Linnane 2021). We compare our proposed methods and results with those obtained by UNEP to identify complementarity, highlight differences, and suggest synergies for further improvement.

3.1.2. Method

The method developed in Pardo et al. (2021) for the North Atlantic Ocean in the 5th issue of the Copernicus Ocean State Report was extended to derive indicator time series for reporting on potential ocean eutrophication and oligotrophication (PE and PO) in the European regional seas at the EEZ level for consistency with the UNEP progressive monitoring approach (Figure 3.1.2(A)). Annual PE maps were derived for each year and basin using satellite-derived chlorophyll-a concentration from the corresponding CMEMS REP Ocean Colour datasets (product references 3.1.1 to 3.1.5).

Pardo et al. (2021) developed the PE and PO indicator suite based on the chlorophyll-a 10th and 90th percentiles (P10 and P90 henceforth). The metrics P10 and P90 are considered good indicators to define the baselines of the annual chlorophyll-a cycle, detect the bloom dynamics and to identify high chlorophyll-a episodes (e.g. Gohin et al. 2008; Park et al. 2010; Groetsch et al. 2016; Gohin et al. 2020; Pardo et al. 2021).

First, to derive the annual PE and PO maps using satellite-derived chlorophyll-a concentration provided in the CMEMS Ocean Colour regional products (product references 3.1.1–3.1.5), daily observations over the year were compared on a pixel-by-pixel basis with the corresponding P10 and P90 climatologies (1998–2017), as in Pardo et al. (2021). For each reporting year, individual pixel values were checked to see if they were above the P90 threshold, below the P10 threshold, or within the [P10, P90] range. If 25% of valid observations within the reporting year for a given pixel were above the P90 threshold, the pixel was flagged as potentially eutrophic condition. Similarly, if 25% of the observations for a given pixel were below the P10 threshold, the pixel was flagged as potentially oligotrophic condition. The method, originally developed for the North Atlantic Ocean (Pardo et al. 2021), was extended to all European regional seas: the Mediterranean Sea, the Black Sea and the Baltic Sea, and corresponding PE and PO maps have been derived using the relevant CMEMS Ocean Colour regional products (product references 3.1.2–3.1.5).

Then, new to this work, the PE maps were aggregated for each EEZ per year to derive the 1998–2020 time series for each European country of the Level 2 SDG 14.1.1a chlorophyll-a concentration sub indicator. To this aim, values from the annual PE maps for each EEZ polygon (VLIZ 2019) were then extracted from every year (Figure 3.1.2(A)). Annual EEZ mean values were then calculated by performing a spatial average (weighted by pixel area) over the extracted datasets. Finally, annual values for EEZ were presented as a 1998–2020 time series to show the development of the chlorophyll-a concentration sub indicator over time, with each data point representing a European country for a specific year. The EEZs for some countries lie across two basins and hence two different CMEMS regional products. In the case of France and Spain EEZs, the annual data point is a weighted average of the values computed with the North Atlantic and Mediterranean products (product references 3.1.1 and 3.1.3). The same approach was applied for Turkey across the Mediterranean and Black seas (product references 3.1.3 and 3.1.4). Instead, for Sweden the Baltic Product was used (product reference 3.1.5), while for Denmark and Germany only the North Atlantic product was selected (product references 3.1.1).

In the proposed level 2 chlorophyll-a concentration sub-indicator method for European waters, henceforth referred to as the 'proposed level 2 method', we have also specifically addressed the treatment of missing data (Figure 3.1.2(A)). In the computation of the baseline climatological P90 and P10 values, we imposed

the criterion that at least 5 years out of the 20-year baseline must contain valid data, for these metrics to be calculated. For a particular pixel and day of year, if the number of available observations fell below the threshold, then no further calculations were applied to that location. In computations for the reporting year, if no observations were available for a particular date and location, then it was not possible to calculate differences from the baseline P90 and P10 values for that location and date. In the reporting year, the number

of anomalous observations (<P10 or >P90) and the number of valid observations at that pixel for that year were then used to calculate the percentage of occasions when the thresholds were breached. The coverage threshold was set at 50% (half a year) for the reporting year.

Several considerations with respect to the desirable traits of an eutrophication indicator went into designing the proposed Level 2 method presented here. Since eutrophication implies a change from a baseline, it is

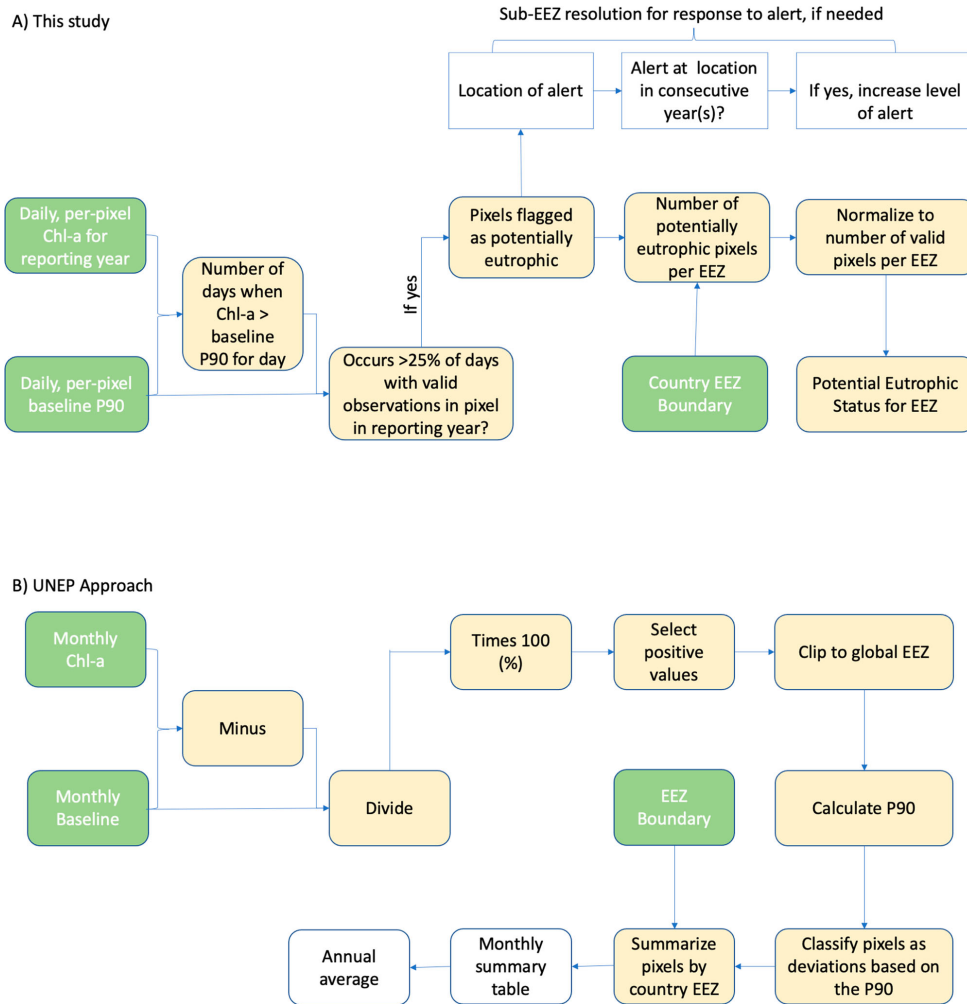


Figure 3.1.2. Schematics of the derivation of the SDG14.1.1a sub-indicator on the state of coastal eutrophication. (A) Schematic of the Level 2 approach for the derivation of the annual PE and PO maps and of the chlorophyll-a concentration sub-indicator per Exclusive Economic Zone. (B) UNEP Level 1 approach reproduced with small modification from UNEP (2021).

important to first establish a threshold against which change is measured. This threshold has to satisfy certain criteria. Most importantly, it has to account for natural variability at any given location, including seasonal and interannual variations, because of climate variability. Hence the threshold has to be based on a multi-year baseline, and we have chosen a 20-year baseline, to account for decadal variability. The threshold used here is site-specific, and varies with day of year. Since eutrophication implies an extreme event, we have not averaged over time (weekly or monthly), to avoid smoothing out of extreme events by the averaging process. Eutrophication is a reversible process: if the source of the excess nutrient is cut off, eutrophication can be reversed (EEA 2019a). Therefore, for monitoring the effectiveness of measures to improve water-quality, the observed level of eutrophication in one year must be compared against that in subsequent years. This requires a fixed threshold for every location, from one year to the next, and the threshold used here is invariant from one reporting year to the next. Eutrophication implies an increase, over and above the natural variability. Hence our threshold is the 90th percentile for each location, established for a fixed 20-year baseline. In a baseline-like year, we can expect 10% of the observations to exceed P90. Hence, we raise the potential eutrophication indicator flag for a location only if, in any given year, P90 is exceeded in 25% of the available observations. Since the method tests for deviations from the norm over the entire year, it captures both sporadic as well as sustained eutrophication events. We also had to decide whether eutrophication should be established over the growing season or over the entire year. We have opted to monitor for eutrophication over the whole year, to avoid any errors that might be caused from ambiguities in defining a growing season, which can of course vary with location and from year to year.

Within the context of the UN SDG 14.1.1, GEO Blue Planet¹ contributed to the drafting of the methodology for calculating the SDG 14.1.1a sub-indicators on chlorophyll-a deviations and anomalies (GEO Blue Planet 2021; UNEP 2021). The UNEP (2021) proposed method for the Level 1 chlorophyll-deviation sub-indicator based on satellite derived global chlorophyll-a (4 km OC-CCI data, product reference 3.1.6) is illustrated in a schematic manner in Figure 3.1.2(B). The UNEP (2021) method differs from the proposed Level 2 method in the basis and treatment of the P90 estimates and in several other details. Briefly, the UNEP (2021) method uses a fixed 5-year baseline (2000–2004), from which monthly mean chlorophyll-a values are calculated for every satellite pixel. For the reporting year, all local deviations from the corresponding reference

mean chlorophyll-a are calculated and noted as relative percent differences. The P90 is calculated for the distribution of positive relative percent deviations of all pixels from the global EEZ of all countries for the reporting month. Pixels with differences that exceed the global P90 for that month of the year are identified as having deviations. Monthly percentage of pixels within each country EEZ with chlorophyll relative percent difference values greater than P90 is then calculated, and averaged over the whole year, as the eutrophication index for that country for the reporting year. For comparison with the proposed Level 2 method, we present the UNEP (2021) results for the European Seas.

3.1.3. Results

Figure 3.1.3 presents the annual PE and PO map for 2020 based on CMEMS Ocean Colour regional datasets, visualising where the daily observations over the year were above the P90 or below the P10 thresholds. The indicator map highlights few scattered potentially eutrophic areas in 2020: in the Baltic Sea, the annual PE indicator identified a wide offshore area in the central Bothnian Sea, and also highlighted the coastal waters of the Skagerrak and Kattegat straits, confirming previous trends reported for these problem areas (Andersen et al. 2016); in the North Atlantic, areas in the coastal waters of the Norwegian Sea, the Iberian Shelf waters and in the Gulf of Biscay and in Southern Brittany were detected; in the Mediterranean and Black Seas eutrophic status was mainly identified in a narrow coastal strip.

Extensive coastal and shelf waters showed active PO status for 2020: in the North Atlantic large potentially oligotrophication areas were identified in the Iberian Shelf waters, Bay of Biscay, Strait of Gibraltar and the northern coast of Morocco; most of the offshore waters in the Western Mediterranean basin, the Northern Aegean Sea, as well as the western open waters, and the northern and southern coastal waters of Black Sea are classified as potentially oligotrophic. These chlorophyll-a reductions are coherent with the negative trend and anomalies reported in the regional seas (North Atlantic, Mediterranean and Black Sea) for 2020 (CMEMS OMI 2020).

The time series of the proposed Level 2 chlorophyll-a concentration sub-indicator method for European waters based on CMEMS Ocean Colour regional products is presented in Figure 3.1.4. The 1998–2020 PE time series shows low percentages across the EEZs with some remarkable PE events occurring in the first decade, with values ranging from 2–4% up to over 20%. In particular, Poland yielded 37.8% in 2008,

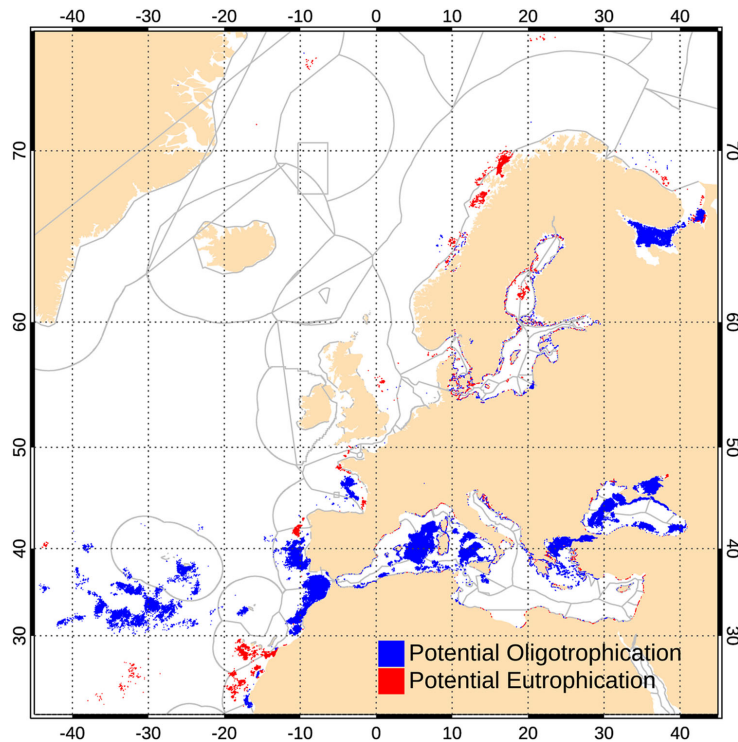


Figure 3.1.3. 2020 annual PE (red) and PO (blue) European method indicator map calculated using the CMEMS Ocean Colour regional products (product references 3.1.1–3.1.5). Active PE flags indicate pixels where more than 25% of the valid observations were above the 1998–2017 P90 climatological reference. Active PO flags indicate locations where more than 25% of the valid observations were below the 1998–2017 P10 climatological reference.

Bulgaria 25.1% in 2001, Latvia yielded 17.1% in 2008, while Belgium was the only EEZ with two consecutive years above 5%, having reached 15.8% and 23.5% in 2001 and 2002 (Figure 3.1.4). In 2008, four Baltic countries (Lithuania, Latvia, Poland and Sweden) yielded PE values above 7%, thus capturing the extended spring bloom that occurred across the central and southern Baltic Sea and that lasted more than 40 days as reported by Brando et al. (2021).

For several countries, the PE at the EEZ level was often nil or never exceeded 1% of the EEZ area (i.e. Albania, Croatia, Cyprus, Faroe Islands, Greece, Greenland, Iceland, Ireland, Italy, Malta, Monaco, Montenegro, Norway, and the United Kingdom, Figure 3.1.4). Furthermore, from 2013 onwards, most European countries yielded a PE lower than 2%, with the exceptions of Slovenia in 2013–2014 (3.7 and 2.7%) and Spain in 2018 (2.8%). The overall reduction in the PE observed in the second decade of the time series is

consistent with the findings by Friedland et al. (2021) based on ensemble analyses for all European seas. These PE results are also coherent with the improvement from 2008 to 2017 in eutrophication status across offshore and outer coastal waters of the Greater North Sea reported for the OSPAR Maritime Area (OSPAR ICG-EUT 2017), as well as with the decrease in eutrophication risk recently reported by Gohin et al. (2019) using both in situ and satellite chlorophyll-*a* data. Furthermore, the PE results for the Baltic countries are consistent with the pattern reported in the integrated annual classification of eutrophication status in the Baltic Sea that described as a time of trend reversal, recovery and oligotrophication in the whole Baltic Sea-wide assessment, particularly in the last decade (Anderson et al. 2017; EEA 2019a, 2019b).

Figure 3.1.5 presents the time series (1998–2019) of the UNEP (2021) Level 1 chlorophyll-*a* deviation sub-indicator computed from the OC-CCI global

SDG 14.1.1a L2 - CMEMS Regional algorithms

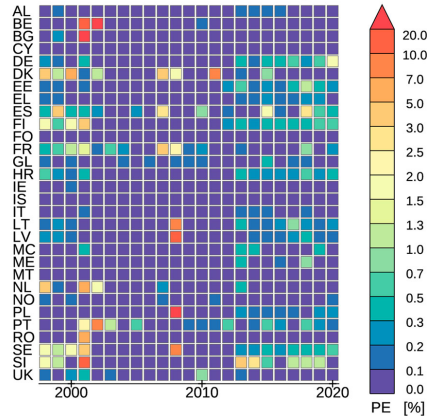


Figure 3.1.4. Time series (1998–2020) of the PE for European waters based on CMEMS Ocean Colour regional products (product ref. 3.1.1–3.1.5), extending the time series 1998–2019 published in Eurostat (2021). Annual EEZ mean values for each European country were calculated by performing for each year a spatial average (weighted by pixel area) of the annual PE map. AL: Albania, BE: Belgium, BG: Bulgaria, CY: Cyprus, DE: Germany, DK: Denmark, EE: Estonia, EL: Greece, ES: Spain, FI: Finland, FO: Faroe Islands, FR: France, GE: Georgia, GL: Greenland, HR: Croatia, IE: Ireland, IS: Iceland, IT: Italy, LT: Lithuania, LV: Latvia, MC: Monaco, ME: Montenegro, MT: Malta, NL: Netherlands, NO: Norway, PL: Poland, PT: Portugal, RO: Romania, SE: Sweden, SI: Slovenia, UK: United Kingdom.

chlorophyll-*a* concentrations. The overall ranges differ substantially from Figure 3.1.4 as values of the sub-indicators are not directly comparable, but most of the patterns are coherent. Some remarkable chlorophyll-*a*-deviation events occurring are captured also in Figure 3.1.4. In 2008, five Baltic countries (Poland, Lithuania, Latvia, Sweden and Denmark) yielded values above 8% (with Poland, Lithuania, Latvia exceeding 20%), thus capturing the extended spring bloom that occurred in the Baltic Sea (Brando et al. 2021) and already identified in Figure 3.1.4. Furthermore, in 2001 Belgium and Romania yielded 17.1% and 13.9%, respectively, while Portugal reached 17.0% in 2002, and Spain 12.9% in 2015. Minimal chlorophyll-*a* deviations were identified with the UNEP (2021) method for seven countries yielding less than 2% for most of the time-series (Albania, Cyprus, Croatia, Greece, Italy, Malta and Montenegro, Figure 3.1.5).

Consistent with Figure 3.1.4 and with the literature discussed above (Anderson et al. 2017; Gohin et al. 2019; EEA 2019a, 2019b; Friedland et al. 2021), also in Figure 3.1.5, it is possible to observe a potential reduction of eutrophication status for the second decade

SDG 14.1.1a L1 - UNEP

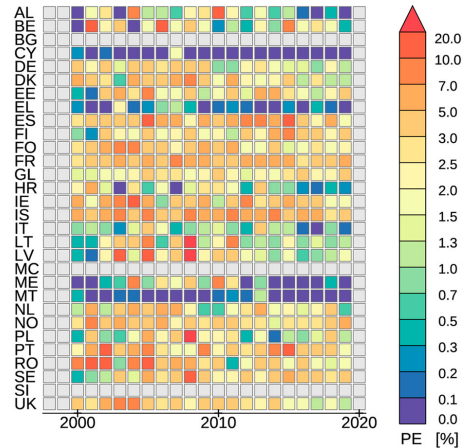


Figure 3.1.5. Time series (2000–2019) of the UNEP (2021) SDG 14.1.1a Level 1 chlorophyll-*a* deviation sub-indicator based on OC-CCI global chlorophyll-*a* data (product ref. 3.1.6). Grey boxes identify missing data: reporting was not computed for 1998, 1999 and 2020 (list of countries as for Figure 3.1.4).

across all European seas. However, it is important to note that the UNEP (2021) method is based on percent differences from the baseline means, and P90 data are calculated from all positive percent differences. This implies that the indicator calculated in this manner may yield some positive values because of natural variability in the system. Therefore, the UNEP (2021) method may identify more potential eutrophication events than the proposed Level 2 method for European waters.

3.1.4. Conclusions

This study presented the refinement and further developments for contributing to the reporting of eutrophication status in the European seas as introduced by Pardo et al. (2021), harnessing the advantages in temporal and spatial coverage offered by remotely sensed ocean colour. We have also carried out some simple comparisons with the UNEP (2021) method's level 1 sub-indicators.

Several areas were identified as potentially eutrophic or oligotrophic in the 2020 indicator map. However, differentiating transient versus sustained eutrophication and oligotrophication processes may be of interest for management and policy decisions. The time series of the indicator is therefore important to evaluate whether long-term changes are occurring. The PE proposed here

provides an estimate of yearly anomalies compared with the regional P90 and P10 climatologies for each EEZ, but it offers no information regarding the spatial location and significance of potential eutrophication and oligotrophication episodes. For understanding of spatial significance, the geographical distribution of the PE and PO, which are provided at the resolution of individual pixels, must be mapped.

The analysis of the time series of the PE over the period from 1998 to 2020 enabled the detection of several eutrophic events occurring mostly in the first decade, followed by an overall reduction in the PE from 2013 onwards. For several European countries, the PE at the EEZ level was often nil or never exceeded 1% of the EEZ area.

For comparison, the chlorophyll-*a* deviation sub-indicator described in the UNEP (2021) method based on OC-CCI global chlorophyll-*a* data was calculated for European EEZs. The overall ranges and patterns differ substantially from those retrieved with the proposed level 2 method for European waters as the values of the sub-indicators are not directly comparable, but most of the patterns are coherent.

Reconciling with literature the time series of the PE (retrieved with either method presented here) at an individual EEZ level is problematic, as most papers report phytoplankton phenology, trends and occurrence of eutrophication at the basin or sub-basin level (Colella et al. 2016; Anderson et al. 2017; Malone and Newton 2020; Brush et al. 2021; Friedland et al. 2021) or for focused coastal marine ecosystems (Zingone et al. 2010; Agusti et al. 2017; Breitburg et al. 2018).

Attempting to monitor eutrophication using only remote sensing chlorophyll-*a* fields has several limitations. Eutrophication is a process resulting from the supply of excess nutrients, and the remote sensing does not measure nutrients but rather estimates phytoplankton concentration. For this reason, the use of the term potential eutrophication (Maúre et al. 2021), was adopted in this study to refer to satellite-derived eutrophication indicators. An increase in chlorophyll-*a* may indicate an early manifestation of the eutrophication process in the marine ecosystem. The proposed level 2 chlorophyll-*a* concentration sub-indicator method does not identify the cause of eutrophication, but does provide an alert that increased phytoplankton growth has occurred at the surface, which could indicate eutrophication. We suggest that agencies or organisations utilise the satellite eutrophication indicators to identify areas of potential eutrophication and follow up to investigate the occurrence further, to establish nutrient status and potential causes or sources of nutrient inputs. These methods are capable

of providing information about where events occurred within the resolution of the satellite data, nominally 1×1 km in this instance. The benefit of satellite data is the ability to gain a synoptic view of potential eutrophication by examining changes in chlorophyll-*a* in space and time, and the ability to gather data in areas that lack sufficient in situ monitoring. The choice of exploring daily events leaves the method vulnerable to missing data. No analysis or reporting is possible when the number of observations is statistically insufficient either in the baseline years or in the reporting year.

Sustainable stewardship of EEZ may also require information on the level of deviation from P90 and not simply the exceedance of the P90 threshold. Mitigation efforts might also require higher temporal resolution in reporting, such that responsible agencies and organisations are alerted the instant the anomaly occurs. A benefit to using methods based on publicly available remotely sensed chlorophyll-*a* data from the world's operational satellite missions is that low latency observations of chlorophyll-*a* concentrations can be monitored for supplemental information in the interim prior to the calculations of relative indicators.

We conclude that the potential eutrophication and oligotrophication indicators within the proposed level 2 chlorophyll-*a* concentration sub-indicator method for European waters are an essential component, but not sufficient in isolation, to meet our responsibilities towards sustainable ocean stewardship enshrined in the SDG 14 targets. We acknowledge that indicator methods should continue to evolve with potential improvements to the reporting structure that CMEMS might consider in the coming years. In particular, future work will need to assess the sensitivity of the proposed method to: (i) the monitoring time-window, i.e. over the whole year rather than just the growing season; (ii) the number of valid observations for each year used to calculate the percentage of occasions when the thresholds were breached; (iii) the spatial variability of the exceedance of the thresholds when integrating over EEZs; and (iv) the propagation of the chlorophyll-*a* concentrations retrieval uncertainties to the potential eutrophication and oligotrophication indicators.

Acknowledgements

The scientific results and conclusions, as well as any views or opinions expressed herein, are those of the author(s) and do not necessarily reflect those of NOAA or the U.S. Department of Commerce.

Section 3.2. Trends in nutrient and chlorophyll *a* concentrations from FerryBox transect time series in the Baltic Sea

Authors: Samu Elovaara, Sebastian Ehrhart, Seppo Kaitala, Petri Maunula, Jukka Seppälä

Statement of main outcome: The Baltic Sea is heavily eutrophicated because of high, mainly anthropogenic, nutrient inputs from the catchment area. Eutrophication causes ecological and socio-economic impacts so measures to reduce nutrient loads have been implemented. Such policies depend on accurate and abundant monitoring data to implement environmental status indicators reliably. Unattended FerryBox monitoring extends measurements of nutrient concentrations beyond fixed monitoring sites and alleviates the temporal bias of measurements caused by regular monitoring cruises. Our results from a FerryBox transect between Finland and Germany, crossing various sub-basins of the Baltic Sea, capture the seasonal cycle of nutrient concentrations, differences among major regions and individual anomalies on fine spatial and temporal scales. Our data show that inorganic nitrogen (N) and phosphorus (P) concentrations, the nutrients mainly controlling eutrophication, have not decreased during the monitoring period (2007–2020) despite nutrient load reduction efforts. Phosphate and total P concentrations have instead increased slightly in the Gulf of Finland. Dissolved silicate (DSi) concentrations have increased during the past four years in most of the observed sea areas. While DSi concentration does not control eutrophication as much as N and P, it is intimately related to diatom productivity, and through diatoms to sedimentation of organic matter. Thus, better incorporation of DSi into environmental indicators might be warranted. Monitoring the ecological status of the seas would benefit from a multi-platform sampling strategy, as not all scales can be adequately covered by a single platform. FerryBox measurements provide information on fine scale trends in surface waters, as shown here, and should be combined with more traditional monitoring data to better assess the state of our seas.

Products used:

Ref. No.	Product name and type	Documentation
3.2.1	INSITU_GLO_BGC_REP_OBSERVATIONS_013_046	PUM: https://resources.marine.copernicus.eu/documents/PUM/CMEMS-INS-PUM-013.pdf

(Continued)

Continued.

Ref. No.	Product name and type	Documentation
		QUID: https://resources.marine.copernicus.eu/documents/QUID/CMEMS-INS-QUID-013-046.pdf

3.2.1. Introduction

Nutrient inputs into the Baltic Sea have been high for decades and most regions of the Baltic Sea are affected by eutrophication (Rönnberg and Bonsdorff 2004; Fleming-Lehtinen et al. 2008; Andersen et al. 2017). Eutrophication remains one of the main environmental problems, despite many measures attempting to reduce nutrient inputs (HELCOM 2018a). Conditions unaffected by eutrophication are not expected to be reached unless Baltic Sea Action Plan nutrient reduction targets are met. Even if targets were met some basins would remain eutrophicated for decades to hundreds of years (Murray et al. 2019). Therefore, a more detailed understanding of the regional differences, seasonality and long-term changes in the eutrophication process is needed.

Seasonal dynamics between surface water inorganic nutrient concentrations and phytoplankton biomass in the Baltic Sea follows a predictable pattern. Dissolved inorganic N, mainly nitrate (NO₃), inorganic P, mainly phosphate (PO₄), and DSi (SiO₄) accumulate during winter (Snoeijs-Leijonmalm et al. 2017). In spring, increased irradiance and stratification initiate propagation of phytoplankton which drains NO₃, PO₄ and DSi pools simultaneously as phytoplankton biomass, most handily measured using chlorophyll *a* (Chl *a*), starts to increase. In most parts of the Baltic Sea NO₃ is depleted first resulting in the decline of the spring bloom, leaving excess PO₄ in the water column (Raateoja et al. 2011). During the summer, NO₃, and PO₄ remain low, as the thermocline prevents nutrient transfer from deeper layers and abundant phytoplankton communities take up surplus N and P. Later, as irradiance and temperature decrease towards winter, the growing season is terminated and free NO₃, PO₄ and DSi start to accumulate again in the surface waters.

Phytoplankton production in the Baltic Sea is generally N-limited, with some exceptions like the northern low-saline regions (Tamminen and Andersen 2007) and freshwater lagoons (Pilkaityte and Razinkovas 2007), which are influenced by the high inorganic N:P

ratio of riverine water (Savchuk 2018). Denitrification of inorganic N (Deutsch et al. 2010; Dalsgaard et al. 2013) and flux of inorganic P from anoxic sediments and deep waters (Conley et al. 2009) maintain low inorganic N:P ratios and N-limitation during the growing season in most regions.

DSi enters the sea mainly through weathering and is taken up by diatoms during the spring bloom. DSi concentrations in the Baltic Sea are assumed to have decreased significantly during the last century due to damming and eutrophication in the catchment area (Humborg et al. 2008). While DSi concentration decreases considerably during spring, diatom growth has not yet been considered Si-limited in the main basins of the Baltic Sea (Wasmund et al. 2013). However, parts of the Baltic Sea, like the Gulf of Finland and the Gulf of Riga, have been predicted to become silica limited based on previous measurements (Danielsson et al. 2008). Traditional diatom-dominated spring blooms have increasingly been substituted by blooms of non-siliceous dinoflagellates in the Gulf of Finland and the northernmost basins of the Baltic Sea (Klais et al. 2011) which may affect DSi cycling and have wide-reaching biogeochemical ecological consequences (Spilling et al. 2018).

During summer, low inorganic N:P ratios enhance the formation of blooms of filamentous diazotrophic cyanobacteria. These blooms are an annually occurring feature of the Baltic Sea, producing a peak of phytoplankton biomass after the spring bloom and yet another input of N in the surface water, by fixing atmospheric nitrogen (Ohlendieck et al. 2000). These blooms benefit from eutrophication and have in recent decades started to appear earlier and increased in intensity (Kahru and Elmgren 2014). They now contribute significantly to N-input even in the less eutrophicated Bothnian Sea (Olofsson et al. 2021). As some of these species produce toxins, cyanobacterial blooms are considered to be one of the primary nuisances of eutrophication.

To understand and mitigate eutrophication, nutrient dynamics must be examined at relevant spatial and temporal resolution and coverage. Traditional research vessel-based measurements are performed at fixed sampling sites, which enables the generation of long time series at those locations, but often with low temporal resolution. For example, the Finnish national monitoring cruises visit open sea stations four times per year at most (Rantajärvi et al. 2020) and timing of these cruises cannot easily be adjusted to match key events in pelagic ecosystems. To analyse shifts in the seasonality or areal patterns, more detailed observations are needed. Spatial coverage of

measurements can be expanded cost-efficiently using automated FerryBox sampling systems installed on commercial vessels, so-called ships of opportunities (SOOP). SYKE Alg@line network, which is part of the Finnish national FINMARI RI consortium (<https://www.finmari-infrastructure.fi/ferrybox>), has been using SOOPs since 1993 (Rantajärvi 2003) and currently employs FerryBox systems on two regularly operating ferries; Finnmaid (Finnlines) operates between Helsinki and Travemünde twice a week and Silja Serenade (Tallink) operates between Helsinki and Stockholm daily. The nutrient measurement data collected by these ferries have been included in CMEMS products since June 2021 (product ref. 3.2.1).

In this study, we analysed climatologies of nutrient and Chl *a* concentrations and their trends in different regions of the Baltic Sea using data collected by FerryBox on the Finnmaid ferry (product ref. 3.2.1) during the period 2007–2020. We visualised the differences in seasonal nutrient and Chl *a* concentrations on a north–south gradient characterised by increasing salinity and average temperature. The study demonstrates the use of sustained FerryBox data in analysing spatial and temporal trends in nutrient concentrations, at scales unachievable using traditionally collected data.

3.2.2. Methods

Data (product ref. 3.2.1) were collected using the FerryBox installed on the ferry Finnmaid. The system consists of a thermosalinograph, fluorometers for chlorophyll, phycocyanin and chromophoric dissolved organic matter, taking measurements every 20 s, and a temperature-controlled water sampler (Ruokanen et al. 2003). The water inlet is at a nominal depth of 5 m. Discrete water samples (24 samples from pre-selected transects) are collected at predetermined locations (as the route is not always the same, water sampling is triggered at fixed longitudinal positions) approximately twice per month and analysed at the SYKE laboratory (Raateoja et al. 2018). Nutrient concentrations (Total N, Total P, NO₃, PO₄ and SiO₄) were measured approximately once per month using Lachat QuickChem 8000 flow injection analyser (up until 26.10.2020) and with Skalar SAN++ continuous flow analyser (26.10.2020 onwards) based on Grasshoff et al. (1999). NO₂ concentration is included in NO₃ concentration. Chl *a* was measured from each sample, extracted using 96% ethanol, and measured fluorometrically, as described in HELCOM (2017). Salinity and temperature were measured continuously within FerryBox using SBE45 MicroTSG thermosalinograph

(Seabird) and SBE38 temperature sensor (Seabird), respectively, and the data corresponding to water sampling times was extracted.

Data consist of weekly to monthly sampling sets from 2007 to 2020 on a transect from Travemünde to Helsinki (Figure 3.2.1, Product ref. 3.2.1). Finnmaid took different routes over the years. The route with the most measurement data, passing east of the island of Gotland, was selected. All other routes were discarded from this study. As the sampling positions were not exactly the same for all cruises, they were grouped into zones with a radius of roughly 5 km (hereafter referred to as zones). Zones were created by applying a nearest neighbour cluster search in python (DBSCAN from sklearn, <https://github.com/scikit-learn/scikit-learn>) resulting in 24 zones. The centres of the zones were assigned coordinates (Figure 3.2.1). The total number of sampling events for each zone varies between 266 and 343, i.e. 19–25 samples per year for each zone.

The seasonality within each zone was approximated by binning the values by month of the year and calculating the mean of each bin. This gave an average annual cycle that was subtracted from the 14-year time series

of each zone, leaving the long-term trend per zone provided other cyclic effects are absent. The long-term trend within each zone was then fitted with a linear model to estimate the typical annual change of a variable in each zone.

3.2.3. Results

Monthly means of total N, total P, NO_3 , PO_4 , SiO_4 , and Chl *a* concentrations, temperature and salinity in the surface water capture seasonality and the regional differences covered by the FerryBox transect (Figure 3.2.2). The salinity gradient characterising the Baltic Sea is prominent with higher salinity at the Bay of Mecklenburg and Arkona Basin and lower salinity at the Gulf of Finland (Figure 3.2.2(b)). Chl *a* concentrations (Figure 3.2.2(h)) and winter accumulation of NO_3 (Figure 3.2.2(e)) and PO_4 (Figure 3.2.2(f)) are higher in the Gulf of Finland compared to the central and southern Baltic Sea, pointing to more severe eutrophication in the Gulf of Finland. NO_3 (Figure 3.2.2(e)) is depleted after the spring Chl *a* peak (spring bloom), which occurs earlier in the southern part of the transect (Figure 3.2.2(h)) and remains depleted throughout the transect until October–December. Spring consumption of PO_4 (Figure 3.2.2(f)) and DSi (Figure 3.2.2(g)) does not result in full depletion of their pools. Thus, the availability of DSi remains high throughout the year in most regions, especially in the southern Baltic Sea. Depleted NO_3 and availability of PO_4 and DSi suggest that the region covered by the transect is primarily N-limited during the growing season. Summer cyanobacterial blooms are visible in Chl *a* concentration in June–July especially in the Gulf of Finland (Figure 3.2.2(h)). Based on the depletion and accumulation of NO_3 , PO_4 and DSi, and the occurrence of Chl *a* peaks, the average growing season is approximately 2 months longer in the southernmost end of the transect than in the north.

Based on the monthly means, anomalous years were detected showing both extreme events and general trends during 2007–2020 (Figures 3.2.3 and 3.2.4). The record warm summer of 2018 and beginning of 2020 are visible in the increased water temperature throughout the transect (Figure 3.2.3(a)). Intrusions of high saline water are seen as spikes in the southernmost study area (Figure 3.2.3(b)). Exceptionally high DSi concentrations were measured throughout the transect since 2017 (Figure 3.2.3(g)). DSi concentrations increased at an average yearly rate of $0.3\text{--}0.5 \mu\text{mol L}^{-1} \text{y}^{-1}$ at each zone except zone 1 compared to the monthly means (Figure 3.2.4(e)). Total P (Figure 3.2.4(b)) and PO_4 (Figure 3.2.4(d)) concentrations also increased during the period 2007–2020, especially in the northern

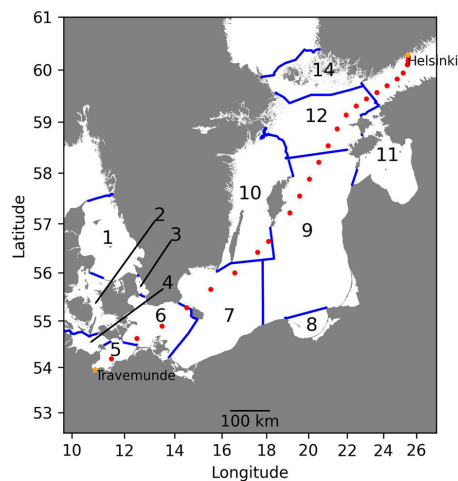


Figure 3.2.1. Map of the Baltic Sea (excluding northern sea areas) and the shipping route of Finnmaid used for the transect (product ref. 3.2.1). Red points mark the centres of the zones into which sampling locations were pooled. Numbers refer to sub-basins of the Baltic Sea, which are separated by blue lines. 1: Kattegat, 2: Great Belt, 3: The Sound, 4: Kiel Bay, 5: Bay of Mecklenburg, 6: Arkona Basin, 7: Bornholm Basin, 8: Gdansk Basin, 9: Eastern Gotland Basin, 10: Western Gotland Basin, 11: Gulf of Riga, 12: Northern Baltic Proper, 13: Gulf of Finland, 14: Åland Sea.

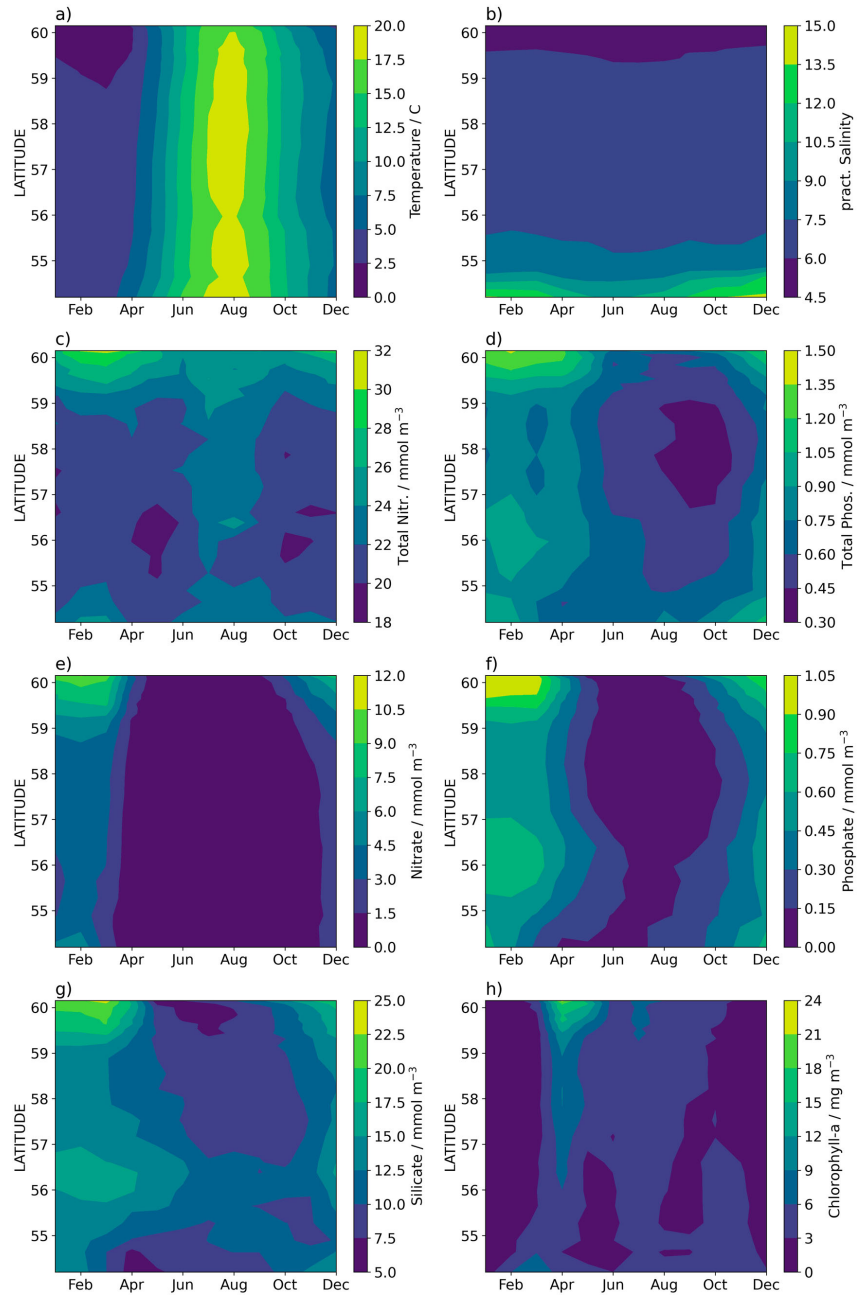


Figure 3.2.2. Monthly means of temperature (a), salinity (b) and concentrations of total N (c), total P (d), NO₃ (e), PO₄ (f), DSi (g) and Chl a (h) during the entire measurement period (2007–2020) calculated using in situ data collected by Finnmaid FerryBox (product ref. 3.2.1). Observations were grouped into 24 zones (see methods and Figure 3.2.1) which are presented using the latitude of the centre of the zones.

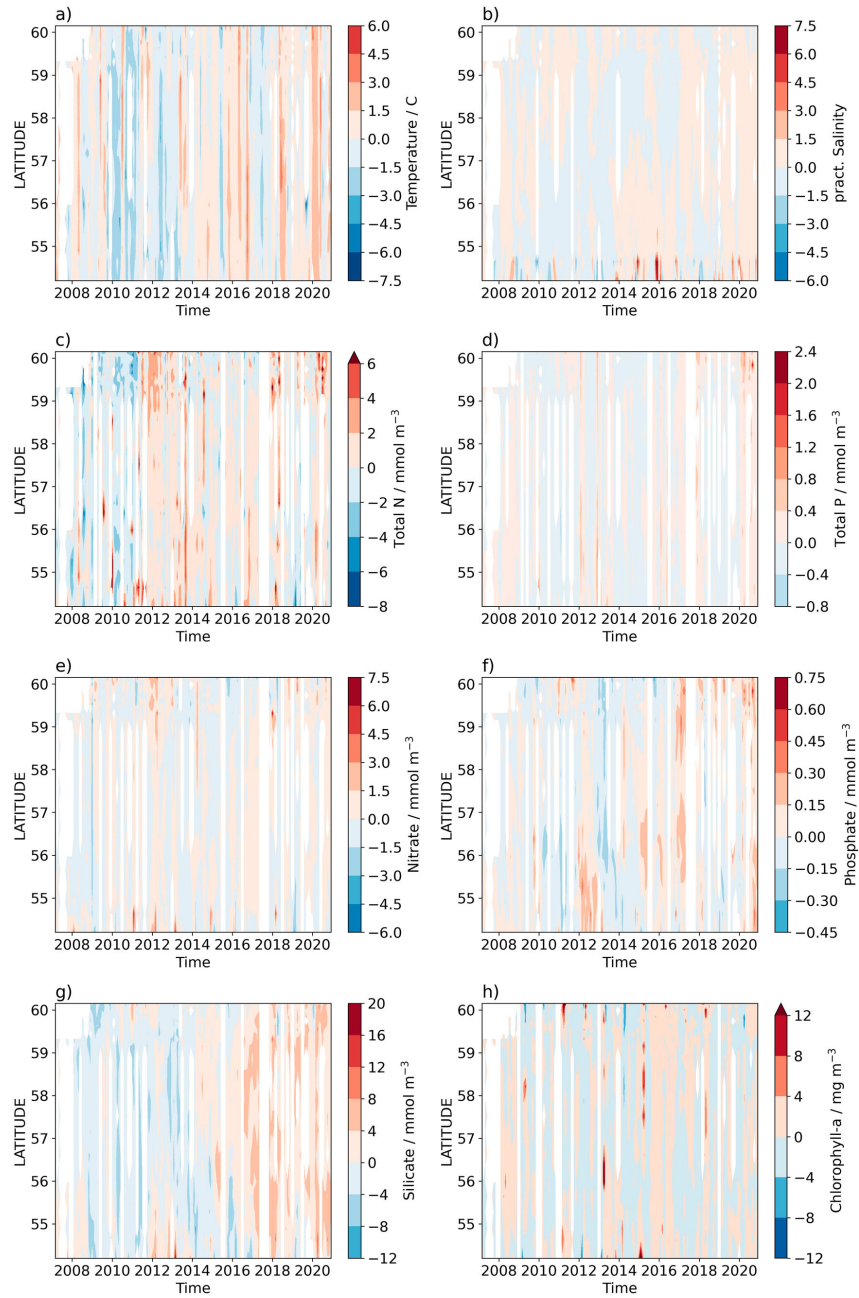


Figure 3.2.3. Deviation of temperature (a), salinity (b) and concentrations of Total N (c), Total P (d), NO_3 (e), PO_4 (f), DSi (g) and Chl a (h) from the monthly means (Figure 3.2.2) of the total measurement period (2007–2020) calculated using in situ data collected by Finnmaid FerryBox (product ref. 3.2.1). Observations were grouped into 24 zones (see methods and Figure 3.2.1) which are presented using the latitude of the centre of the zones.

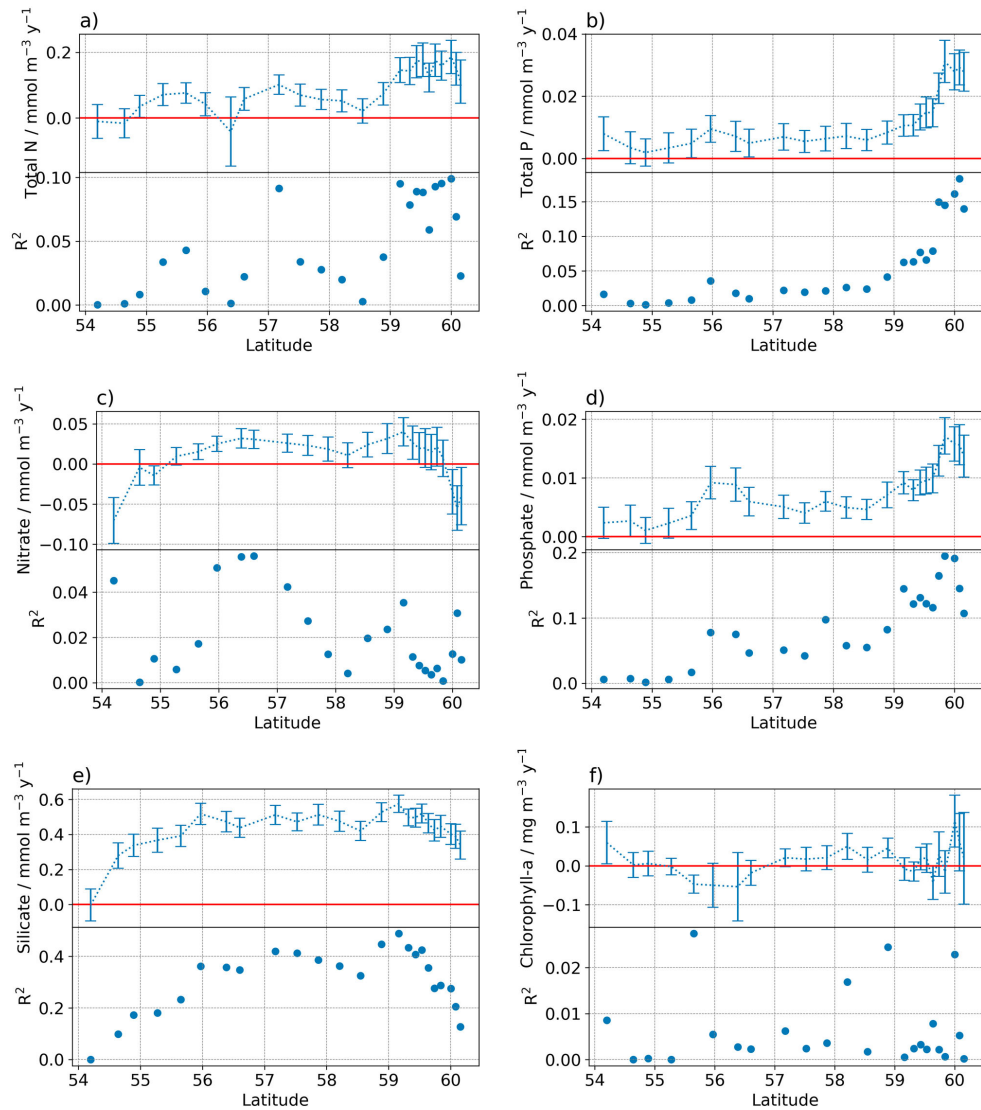


Figure 3.2.4. The upper sub-panel in each panel shows the average annual change from the monthly mean of total N (a), total P (b), NO_3 (c), PO_4 (d), DSI (e) and Chl *a* (f) during the total measurement period (2007–2020) as a function of the latitude, calculated using in situ data collected by the Finnmaid FerryBox (product ref. 3.2.1). Error bars show the standard error of the fitted long term trend (linear model). The lower sub-panel shows the adjusted R^2 for the linear fit used to derive the annual change.

zones. PO_4 concentrations showed high variation and extended periods (several months) of high and low anomalies were detected (Figure 3.2.3(f)). Prominent extended anomalies in the PO_4 concentration can be seen in the southern Baltic Sea (a positive anomaly in

2012 followed by a negative anomaly in 2013–2014, Figure 3.2.3(f)). Total N (Figure 3.2.4(a)), nitrate (Figure 3.2.4(c)) and Chl *a* concentrations (Figure 3.2.4(f)) have not changed significantly during the period 2007–2020. Greater interannual variations in

the concentrations in the northern area likely resulted in a tendency to higher standard errors of trends in that region.

R^2 of the linear fits was quite low for all variables (Figure 3.2.4), being highest for DSi (~0.4 for mid-latitude stations) and total P and PO_4 (close to 0.2 at higher latitudes). R^2 values were low because there was high variation in the data. As we investigated annual means, i.e. pooled measurements from all the months, the difference in variation among the different seasons (e.g. high values and variation in NO_3 concentration in winter and low in summer) is not included in the model and may contribute to low R^2 values.

3.2.4. Discussion

Unattended sampling using FerryBox systems on SOOP ferry lines generate vast amounts of data, compared to research vessel-based monitoring cruises. Sampling is cost-efficient and flexible, as the timing, location and frequency of sampling is often adjustable (but constrained by the ferry timetable). On the other hand, SOOP data provides samples from the uppermost surface layer only. So far, SOOP data is not fully exploited in monitoring programmes when assessing the trends of the state of the seas. However, as the use of automated systems for aquatic monitoring is increasing, we need to reconsider how they are included in the monitoring programmes and how to optimise the use of multiplatform data (García-García et al. 2019).

FerryBox monitoring can contribute to near real-time diagnosis of changes in pelagic marine ecosystems. Sustained FerryBox data can provide an overview of the spatial extent, timing and duration of events, their interannual variability, as well as long-term trends. This information provides a background for more detailed studies, providing guidance on their timing and positioning to match the events to be studied, e.g. phytoplankton blooms. FerryBox methods do not replace traditional research vessel campaigns which produce much more detailed insight into the ecosystem but supply auxiliary information on the time-space scales.

This study estimated trends in nutrient concentrations using SOOP data in the Baltic Sea. Despite the recent mitigation measures taken these trends are not abating, an observation also supported by HELCOM (2018b). We show that nutrient concentrations in the surface water have changed very little during the past 14 years, with two exceptions. First, there is an increase of total P and PO_4 in the Gulf of Finland, and second, there is an overall increase in the often overlooked DSi concentration.

The observed increase in DSi concentrations contradicts, in the short term, the prediction of decreasing DSi concentration in the Baltic Sea (Danielsson et al. 2008; Humborg et al. 2008). DSi concentration was very rarely below $2 \mu\text{mol L}^{-1}$ which is considered to be growth limiting for diatoms (Egge and Aksnes 1992). As PO_4 concentration has also increased in the Gulf of Finland, the inorganic Si:P ratio has not changed much. However, DSi concentration has increased relative to NO_3 , suggesting that the already N-limited Gulf of Finland has become relatively less silica limited. Changing Si:N ratios might affect relative nutrient limitation dynamics among diatom species (Spilling et al. 2010), thus affecting the composition of the phytoplankton community. We observed increased PO_4 concentrations mainly in the northern part of our study area and towards the end of our measurement period of 2007–2020. However, as shown by Kõuts, Maljutenko, Liu, et al. (2021), PO_4 concentrations for the entire region increased from 1995 to 2000 and have remained high ever since, while nitrate concentrations have decreased. This continuously increased PO_4 concentration relative to NO_3 concentration suggests that cyanobacterial blooms will be an issue for a long time to come, as cyanobacteria gain a competitive advantage in low inorganic N:P ratios (Graneli et al. 1990; Stal et al. 2003).

It is tempting to link the ongoing decrease in the occurrence of diatom-dominated spring blooms (Klais et al. 2011) to the observed accumulation of free DSi. Estimating the magnitude of change in the DSi concentration potentially caused by the community shift is beyond the scope of this study. However, if increased DSi concentration is an indicator of reducing diatom-dominated spring blooms it may also indicate other consequences of reduced diatom dominance on C cycling, such as decreased organic matter sedimentation (Spilling et al. 2018), which have been pronounced during recent years.

The increase of both DSi and PO_4 in the Gulf of Finland might also be related to sedimentation processes and introduction of deep water to the surface layer, as variation in benthic DSi and PO_4 fluxes in the Gulf of Finland show similar patterns (Tallberg et al. 2017). This suggests a tentative connection between sediment hypoxia and DSi release from the sediments. Hypoxic conditions have been persistent in many regions of the Baltic Sea since 2000 and will possibly become more common in the Gulf of Finland (Kõuts, Maljutenko, Elken, et al. 2021). Hypoxia-related DSi and PO_4 release rates thus, cannot be expected to decrease soon. Since P may also be transported from the bottom water of the northern Baltic Proper to the Gulf of Finland, all the way to surface water (Lehtoranta et al. 2017), the

increased PO_4 concentration in the Gulf of Finland should not be considered to have been caused solely by regional processes.

Throughout the study area, there has been no reduction in eutrophication, as shown by high Chl *a* concentrations and the lack of a trend in Chl *a* concentration. The data does not cover the most intense eutrophication period of the Baltic Sea as inputs of N and P have decreased since the 1980s (Gustafsson et al. 2012; HELCOM 2018a). Therefore, this data can primarily be used to assess how nutrient load reduction measures starting in the 1990s have affected surface water nutrient concentrations. However, nutrient residence times in the Baltic Sea are long, estimated at 9 years for total N and 49 years for total P (Gustafsson et al. 2017), and the interconnectivity among basins may compensate for local nutrient reductions (Savchuk 2018). This makes it difficult to connect specific nutrient load reduction measures to changes in nutrient concentrations. Long SOOP time series with high temporal resolution may aid in distinguishing these changes from high regional and interannual variation.

Still, the broad-scale spatial differences in nutrient concentrations agree with recent basin and drainage area-specific investigations. Since 1993 a slight decrease in phytoplankton primary production has been detected in the southern Baltic Sea, where Chl *a* concentrations are generally lower (Zdun et al. 2021). Despite nutrient load reduction efforts nutrient input from rivers to the Gulf of Finland remain high as do NO_3 and Chl *a* concentrations (Räike et al. 2020).

Alg@line FerryBox water sample data has been used in HELCOM spring bloom duration and biomass production indices for management purposes. HELCOM used Chl *a*, dissolved inorganic N and P, total N and P data from FerryBox to create vernal phytoplankton bloom intensity indices connecting them to dissolved inorganic N concentration in the winter (Fleming and Kaitala 2006; Raateoja et al. 2018). As DSi is generally not considered a limiting nutrient it has not been used as an indicator by HELCOM. However, if increased DSi concentration is partially due to reduced diatom populations, DSi concentration might be considered another potential indicator of the ecological status of the planktonic community. In this case, its possibility to strengthen the diatom/dinoflagellate index might be worth exploring (Wasmund et al. 2017). Given the connection between the benthic DSi and PO_4 fluxes (Tallberg et al. 2017), DSi concentration could also be used in support of present indicators of sediment hypoxia.

Other potential uses for the data include investigation of nutrient ratios and nutrient limitation, post-

spring bloom excess PO_4 and its capacity to fuel summer cyanobacterial blooms (Raateoja et al. 2011), and nutrient depletion ratios during phytoplankton blooms. However, studying these may require adjustments in current sampling frequencies and automated nutrient analysis would be an optimal next step for increasing the frequency of FerryBox nutrient sampling.

As FerryBox systems collect high resolution multi-variable in situ data in near real-time, they can be an asset to other research approaches. One common use is the provision of assimilation data for biogeochemical models and ocean colour applications. In addition, FerryBox data can be used in conjunction with stationary sampling data to increase data coverage (Raateoja et al. 2018). Such an approach could possibly be used to increase the confidence of eutrophication status assessments in the Baltic Sea (Fleming-Lehtinen et al. 2015). SOOPs are an integral part of future coastal observation systems to be used in conjunction with stationary sampling stations, other automated systems, remote sensing and modelling, as e.g. in the JERICO research infrastructure (Joint European Research Infrastructure for Coastal Observatories, Farcy et al. 2019). Such large-scale joint operations require good communication between the research fields to identify gaps in observation coverage. Within their route limits, SOOPs can modify their sampling programme providing an excellent method of fine-tuning the data collection required by the modelling, remote sensing and management communities.

3.2.5. Conclusions

Annual climatologies and long-term trends of nutrient and Chl *a* concentrations from 2007 to 2020 covering a north–south gradient from Helsinki to Travemünde were presented. Chl *a* concentration has remained the same throughout the transect, suggesting that eutrophication has not been alleviated in this area. Concentrations of PO_4 and especially DSi have increased over the past 4 years when compared to 2007–2020 monthly averages. Increased PO_4 concentrations demonstrate how slowly the surface water PO_4 concentrations react to nutrient load reduction efforts as new PO_4 is released from the sediments. Systematic increase of DSi concentrations in major basins of the Baltic Sea might be a reason to consider DSi concentration as a potentially important environmental indicator. This is especially important, because the changing DSi concentration may be related to a major ecological change in the Baltic Sea, the shift from diatom to dinoflagellate-dominated spring blooms. We consider the high spatial resolution and temporal coverage of FerryBox data to be an

important component in the sustained analysis of nutrient concentrations and eutrophication.

Acknowledgements

The study utilised SYKE Alg@line FerryBox infrastructure as a part of the national FINMARI RI consortium. We thank two anonymous reviewers for their constructive comments and Danielle Bansfield for language editing.

Funding

The work has been supported by JERICO-S3 project, funded by the European Commission's H2020 Framework Programme under grant agreement No. 871153 and by the Academy of Finland (SEASINK: Evolving carbon sinks and sources in coastal seas - will ecosystem response temper or aggravate climate change?).

Section 3.3. Copernicus Marine Sea Surface Temperature and chlorophyll-a indicators for two Pacific Islands: a co-construction monitoring framework for an integrated, transdisciplinary, multi-scale approach

Authors: Alexandre Ganachaud, Karina von Schuckmann, Andra Whiteside, Cécile Dupouy, Pierre-Yves Le Meur, Maeva Monier, Simon Van Wynsberge, Antoine de Ramon N'Yeurt, Maria Mañez Costa, Jérôme Aucan, Annette Breckwoldt, Louis Celliers, Pascal Douillet, Sebastian Ferse, Elisabeth Holland, Heath Kelsey, Vandhna Kumar, Simon Nicol, Maraja Riechers, Awneesh Singh, David Varillon

Statement of main outcome: The ocean is an integral part for the three pillars of sustainable development: environment, society and economy. Pressures on the ocean from climate change, pollution, and over exploitation have increased over the past decades, posing unprecedented challenges, particularly for vulnerable communities such as the Large Ocean Island States, and these pressures need to be monitored. This study analyses the time series of Essential Ocean Variables sea surface temperature and chlorophyll-a in coastal reefs of two pilot regions in Fiji and New Caledonia. In situ measurements represent true local conditions, with a necessarily limited coverage in time and space. Remote sensing data have a broad coverage but are necessarily limited in terms of resolution and accuracy in the coastal zone. Our analysis points to the advantage in using these complementary data types for the same geographical areas at small spatial scales close to the coast, and in particular, for high frequencies and extreme events. We discuss the way forward for a co-

constructed monitoring framework, drawing on ongoing initiatives in Oceania, and advocate a methodology for the use of ocean data to support society and economy. Co-construction with stakeholder involvement is paramount for this framework, including policy- and decision-makers, industry, scientists, local and indigenous, governmental and non-governmental organisations, all of whom need sound, multi-disciplinary science advice, targeted expertise, and reliable evidence-based information to make informed timely decisions for the right timescale. Such transdisciplinarity combines scientific, traditional, administrative, technical, and legal knowledge repertoires.

Products used:

Ref. No	Product name and type	Documentation
3.3.1	Gridded chl-a (monthly, L4, ESA-CCI): OCEANCOLOUR_GLO_CHL_L4_REP_OBSERVATIONS_009_093	PUM: https://catalogue.marine.copernicus.eu/documents/PUM/CMEMS-OC-PUM-009-ALL.pdf QUID: https://catalogue.marine.copernicus.eu/documents/QUID/CMEMS-OC-QUID-009-030-032-033-037-081-082-083-085-086-098.pdf
3.3.2	Non-gridded chl-a (daily, L3, ESA-CCI): OCEANCOLOUR_GLO_CHL_L3_REP_OBSERVATIONS_009_065	PUM: https://catalogue.marine.copernicus.eu/documents/PUM/CMEMS-OC-PUM-009-ALL.pdf QUID: https://catalogue.marine.copernicus.eu/documents/QUID/CMEMS-OC-QUID-009-064-065-093.pdf
3.3.3	BULA IRD CAMELIA Alis Oceanographic Cruises	Fichez et al. (2006) Torréon et al. (2004) FICHEZ Renaud (2001) BULA 1 cruise, RV Alis, https://doi.org/10.17600/1100110 TORRETON Jean-Pascal (2002) BULA 2 cruise, RV Alis, https://doi.org/10.17600/2100040 DOUILLET Pascal (2003) BULA 3 cruise, RV Alis, https://doi.org/10.17600/3100050 PRINGAULT Olivier (2003) BULA 4 cruise, RV Alis, https://doi.org/10.17600/3100110 DOUILLET Pascal (2004) BULA 5 cruise, RV Alis, https://doi.org/10.17600/4100060 DOUILLET Pascal (2001) BULA, https://doi.org/10.18142/71
3.3.4	CMEMS Ocean Monitoring Indicator: Global map of chl-a trends GLOBAL_OMI_HEALTH_OceanColour_trend	PUM: https://catalogue.marine.copernicus.eu/documents/PUM/CMEMS-OMI-PUM-HEALTH-GLOBAL-OCEANCOLOUR.pdf

(Continued)

Continued.

Ref. No	Product name and type	Documentation
		QUID: https://catalogue.marine.copernicus.eu/documents/QUID/CMEMS-OMI-QUID-HEALTH-GLOBAL-OCEANCOLOUR.pdf
3.3.5	SST_GLO_SST_L4_REP_OBSERVATIONS_010_024	PUM: https://catalogue.marine.copernicus.eu/documents/PUM/CMEMS-SST-PUM-010-024.pdf QUID: https://catalogue.marine.copernicus.eu/documents/QUID/CMEMS-SST-QUID-010-024.pdf
3.3.6	ReefTEMPS network	http://www.reeftemps.science/en/home/ Cheype et al. (2015), Varillon et al. (2021), Cocquempot et al. (2019)
3.3.7	R/V Seamans cruise, station 5288-019, October 2019	Whittaker (2020)

3.3.1. Introduction

Pressures on the ocean from climate change, pollution, and over-exploitation have increased with a growing world population and over time. With continued environmental stress on the ocean in response to ongoing global warming (e.g. IPCC 2019b, 2021), as well as with the prospective development of new ocean-related economic activities, these problems are only expected to further exacerbate (OECD 2020). The ocean is integral to Small Island Developing States' (SIDS) economies (Dornan et al. 2018; Keen et al. 2018) as their vast Exclusive Economic Zones are much larger than their actual land space (70-fold in Fiji, Gassner et al. 2019), and Pacific islanders have proposed to shift the terminology from SIDSs to Large Ocean Island States (LOIS) (Hau'ofa 2000; Morgan 2021). The SIDS/LOIS are particularly exposed to anthropogenic pressure on the ocean due to low elevation, small land area, narrow ecological zonation, climate sensitive ecosystems and natural resources; insufficient financial, scientific and technical capacities; unique social and political conditions, proportionally (compared to mainland countries) more limited human resources, and local and unique forms of bureaucracies (Magan et al. 2019).

Globally, ocean knowledge is of great benefit to inform policy, decision making, governance and management and therefore to increase the likelihood of developing sustainability (Colglazier 2018; Hermes et al. 2019; Kaiser et al. 2019). The concept of Essential Ocean Variables (EOVs) as implemented by the Global Ocean Observing System (GOOS) is based on relevance

for climate and ocean services, including ocean health (Le Cozannet et al. 2017; Le Traon et al. 2017), and considering feasibility, maturity of the science and measurement techniques, and cost effectiveness (Lindstrom et al. 2012). Similarly, the framework of Global Climate Indicators as introduced by the World Meteorological Organisation (WMO 2017) in the light of SDG 13 'Climate action' includes a subset of key indicators – many of them ocean-related – designed to be comprehensive and understood by non-scientific audiences, and form the basis of their annual Statement of the State of the Global Climate (e.g. WMO 2020) used amongst others by the UN Framework Convention for Climate Change. Within the large scale or global processes, the need to include local and indigenous knowledge in adaptation planning and adaptive management remains a challenge (Celliers et al. 2021).

Sea Surface Temperatures (SST) and Chlorophyll-a (Chl-a) are EOVs for the Earth's ocean system (O'Carroll et al. 2019; Sathyendranath et al. 2019). SST impacts marine ecosystems. Satellite derived SST anomalies, and derived indicators (e.g. degree heating weeks (DHW) coral bleaching alert) directly provide relevant information in near-real time that can be used by managers. Monitoring and forecasting local thermal regimes are important for understanding and protecting potential refugia for coral species (Foo and Asner 2020; Schoepf et al. 2020), or managing aquaculture activities (Van Wynsberge et al. 2020). For instance, a warning of abnormal conditions is useful to initiate more intensive *in situ* monitoring, or prepare for action in case of bleaching (Heron et al. 2016; Andréfouët et al. 2018; Sully et al. 2019; Skirving et al. 2020).

The EOVI Chl-a is a proxy for the amount of photosynthetic plankton in the ocean, which is an indicator of carbon uptake, productivity and overall health of the ocean (e.g. Martinez et al. 2009; Mélin et al. 2017). Together with nutrients and suspended sediments, Chl-a is also an indicator of water quality, one of the pressures on vulnerable ecosystems such as the seagrass beds and coral reefs (Devlin et al. 2020; Vollbrecht et al. 2021). At the local scale, it is used to monitor changes in coastal lagoon water quality (Dupouy et al. 2018a; Vollbrecht et al. 2021); it also impacts larval recruitment (Wilson et al. 2018). For instance, Putra et al. (2021) showed that most of the potential fishing ground in Riau Islands (Indonesia) were linked to Chl-a increases associated with different monsoon types. Understanding the drivers of Chl-a variations is therefore important to marine spatial planning efforts and managing marine ecosystems, but the access and ability to make use of such data around Fiji are not yet available to stakeholders (Gassner et al. 2019; MACBIO project – Marine

and Coastal Biodiversity in the Pacific Island Countries²).

Here we analyse SST and Chl-a, as measured at regional (remote sensing/CMEMS products) and local (in situ) scales in two Pacific Islands, Fiji and New Caledonia, to provide insights about CMEMS products' usefulness and limitations for local ecosystem management. These products are often developed for broader applications and not designed for specific local needs. In our discussion, we, therefore, advocate the importance of a local, specific and transdisciplinary approach to co-construct data products that best serve scientists, administrations, authorities, managers, business, and local communities to support ocean sustainability in the long term. We discuss future ways to tackle the missing elements (plural knowledge and norm repertoires of various actors) in the construction of relevant indicators and monitoring frameworks.

3.3.2. Two EOVI indicators in Fiji and New Caledonia

3.3.2.1. Data used

For SST, we used large-scale satellite observations from the ESA CCI project (product ref. 3.3.5). This satellite-derived SST product provides a bulk SST, equivalent to water temperature at 20 cm below the sea surface (Product ref. 3.3.5). We will refer to it as SSTSAT. The inputs to the system are SSTs at 10:30 am and pm local time which means that the SST provided by this product roughly corresponds to the daily average. SSTSAT anomalies are relative to the daily SSTSAT climatology from January 1st to December 31st of the ESA CCI data period. SSTSAT extracted from the product were used directly, without any further processing. The SSTSAT values from this product were compared to local in-situ SST observations for Fiji and New Caledonia using sites from the ReefTEMPS observing network (product ref. 3.3.6), which is part of the French Research Infrastructure for Coastal Oceans and Seashores (ILICO), and also known as the Pacific Insular Coastal Waters Observation Network. ReefTEMPS consists of a number of monitoring platforms at 6–60 m depth scattered around 20 Pacific Island countries, with 30 monitoring stations in New Caledonia, and 11 in Fiji (Cheypte et al. 2015; Cocquempot et al. 2019; Varillon et al. 2021). For the purpose of the current analysis, one station in Fiji and four in New Caledonia were selected to maximise the mutual temporal coverage of remote sensing and in-situ measurements.

For Chl-a, we jointly use four different data products, i.e. a monthly gridded (product ref 3.3.1) and daily non-gridded CMEMS (product ref 3.3.2) remote sensing, the

CMEMS Ocean Monitoring indicator (product ref 3.3.4). These Chl-a satellite products are designed for open ocean use – what are called *Case 1 waters* whose optical signal is dominated mainly by phytoplankton present at low concentrations – and are not designed to be used in optically complex coastal waters – called *Case 2 waters* (IOCCG 2000). Lagoon waters would require adapted algorithms such as the one issued from the comparison of MODIS and in situ Chl-a concentration coincidences all around New Caledonia (Case 1 and 2 waters, Wattelez et al. 2016) and that are yet to be applied to other lagoons. Therefore, only CMEMS data offshore (Case 1 waters) were selected for this study, and only the evolution of offshore waters is discussed. These are compared with *in situ* data collected during five oceanographic cruises South of Fiji from 2001 to 2004 (Bula programme, by IRD / UR CAMELIA, ANSTO and U. South Pacific, product ref. 3.3.3). In-situ Chl-a data were measured after filtration on a 0.7 µm GF/F filter and extraction of the phytoplankton retained in methanol (Chifflet et al. 2004). In addition, a Chl a data point south of the region (178.79° E, 18.48° S) was used to represent the 'bluest water' (product ref. 3.3.7).

3.3.2.2. Regional results from satellite products

3.3.2.2.1. Ocean temperatures. Over the periods that span available in situ data, SSTSAT changes are characterised by surface warming around Fiji and New Caledonia between 2013 and 2019 (Figure 3.3.1(a)), and in the north-eastern part including Fiji between 1997 and 2019 with more than 0.02°C per year (Figure 3.3.1(b)). For comparison, global mean SST increased at a rate of $0.015 \pm 0.001^\circ\text{C}$ per year over the period 1982–2019 (CMEMS 2021b). In contrast, the area north-east of New Caledonia (Figure 3.3.1(b)) showed cooling conditions over the period 1997–2019 at rates of around -0.01°C per year, while the area south-west of New Caledonia showed surface warming conditions over this period, at rates between 0 and 0.02°C per year. Cravatte et al. (2009) and Quinn et al. (1998) found such strong spatial variability in ocean surface warming over many time scales (see also Sun et al. 2017). In the western tropical Pacific, SST vary strongly with the modes of the El Niño Southern Oscillation at interannual time scales, thereby influencing trend calculations over these short periods (e.g. Gouriou and Delcroix 2002).

3.3.2.2.2. Chl-a. The Chl-a trend over the period 1997–2019 is characterised by a decrease between the New Caledonia and Vanuatu archipelagos of more than 1%, and an increase south of Fiji at rates of more than 1% per year (Figure 3.3.1(c)). These trends in biomass of phytoplankton are weak relative to global ocean changes

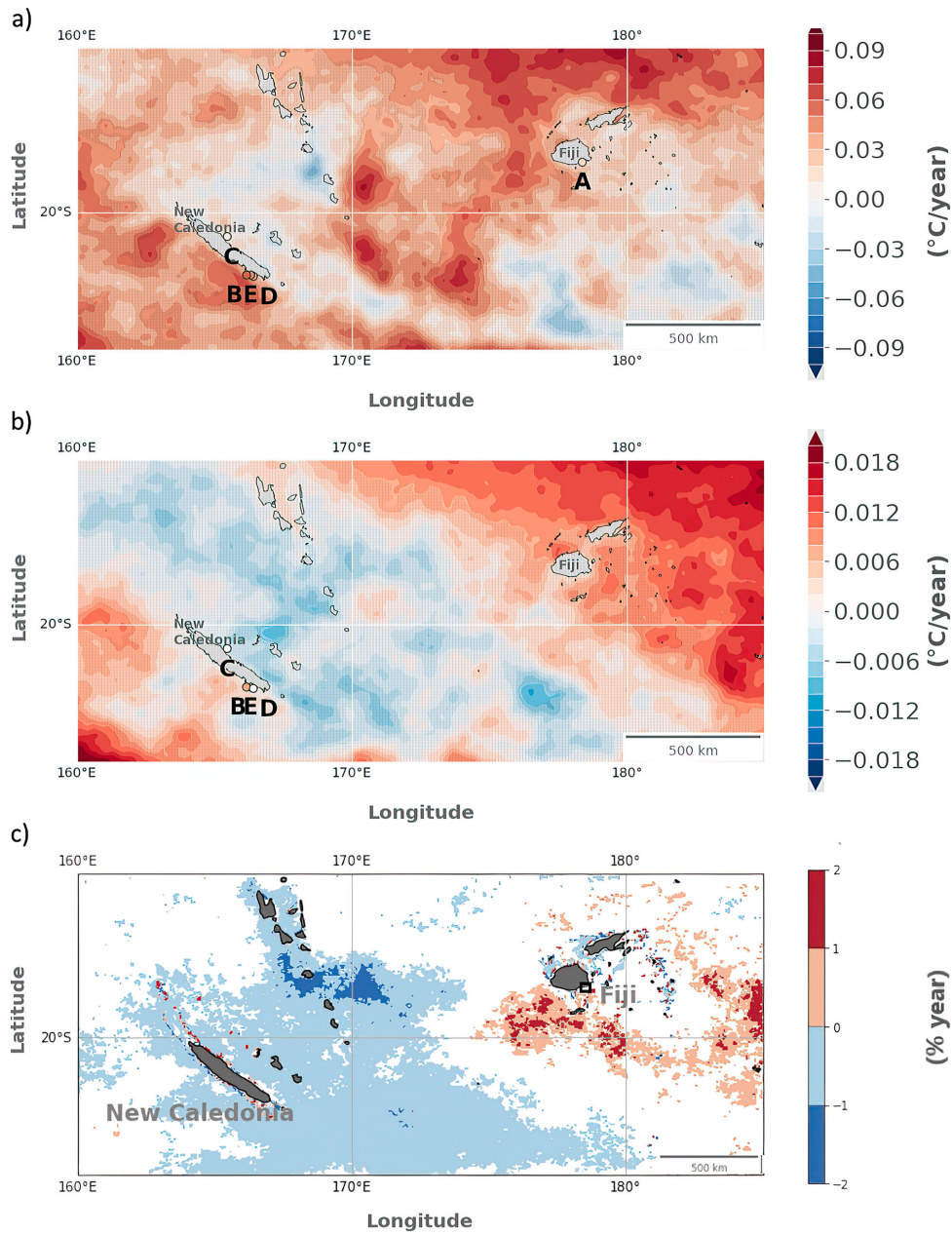


Figure 3.3.1. SST & Chl-a: Trend of Sea Surface Temperature (average yearly anomalies) as derived from product ref. 3.3.5 over the period (a) 2013–2019 and (b) 1997–2019 (units: °C per year). The two periods have been chosen to overlap with the availability of in-situ records. Coloured circles indicate corresponding trend estimates as derived from in-situ observations (product ref. 3.3.6, see Figure 3.3.4). Note the difference in colour scales in the two plots (c) Chl-a trend (units: % per year) over the period 1997–2019 from product ref. 3.3.3. White pixels are not statistically significant.

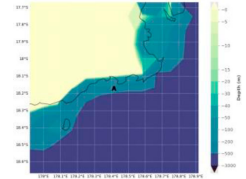
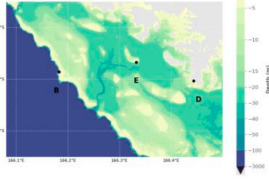
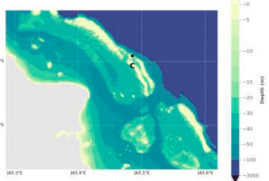
(– 6–10% per year, CMEMS 2021a) and regional Western Pacific changes (–3% to 3% for the same period, Holland et al. 2019). Observations of either a decrease or an increase of Chl-a towards an island in different archipelagoes of the Western tropical Pacific have been attributed to island mass effects (Dandonneau and Charpy 1985). Such variations in Chl-a may originate from a large range of triggering factors including physical environment changes altering the supply of essential nutrients, already found at a large scale in the Pacific Ocean (Dupouy et al. 2004; Martinez et al. 2009). Chl-a trends might also result from changes in phytoplankton species which have different optical properties (e.g. an increase in the proportion of diazotrophs vs picoplankton, a major component of phytoplankton in the region; Dupouy et al. 2018b).

Evaluating phytoplankton composition change over this long period of time would require algorithms for discriminating phytoplankton groups based on CMEMS reflectance observations (IOCCG 2021).

3.3.2.3. Regional to local results: Comparison with in situ data

3.3.2.3.1. Ocean temperatures. SSTSAT trends compared well with in-situ observations during both overlapping study periods (Figure 3.3.1 and Table 3.3.1). However, pointwise examination of the time series reveals a small, systematic underestimation in satellite data. For example, the Suva Reef (Viti Levu Island, Fiji) recorded an in-situ warming rate of $0.024 \pm 0.01^\circ\text{C}$ per year (December 2012 to December 2019), whereas the satellite-derived estimate is barely significant at

Table 3.3.1. In situ temperature meta data and correlation coefficients for the comparison with SSTSAT. Station positions on regional scales, and overlapping time series lengths are provided in Figures 3.3.1 and 3.3.2, respectively. The significance level at 95% would be 0.55 if we had only 10 independent samples and 0.38 for 20 samples. Maps are based on Etopo5 in Fiji, and a high resolution SHOM DEM in New Caledonia.

Platform	Date begin Date end	Depth (m)	Situation Map	Correlation from daily (monthly) values
A-Fiji Suva Reef, Viti Levu 02	21/12/2012 04/03/2020	12	–18.15975 178.3999 	0.78 (0.9)
B-NCL Fausse Passe de Uitoe 01	22/05/1992 02/12/2019	11	–22.28586 166.1832 	0.77 (0.86)
C-NCL Poindimié 01	09/12/1996 08/06/2021	12.5	–20.89183 165.485 	0.87 (0.93)
D-NCL Anse Vata 01	16/04/1997 19/10/2021	2	–22.30376 166.44331	0.75 (0.88)
E-NCL Récif du Prony 01	12/01/1996 28/10/2021	10.5	–22.26733 166.3325	0.84 (0.89)

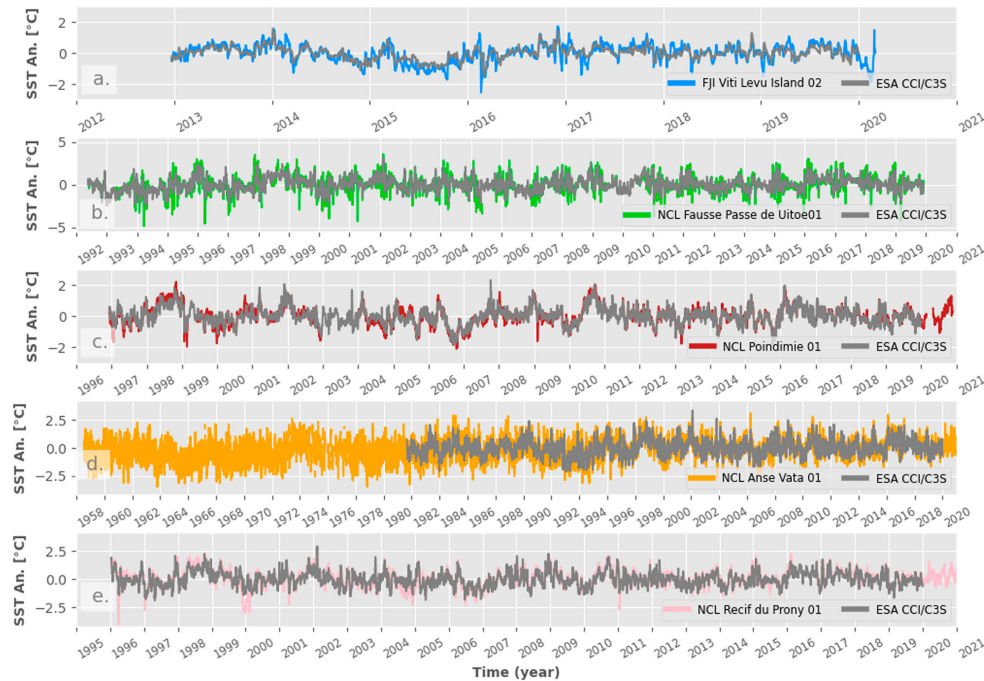


Figure 3.3.2. Time series of daily in-situ SST anomalies at some measurement platforms (coloured lines) in Fiji and New Caledonia of the ReefTEMPS observing network (product ref. 3.3.6). Station locations (a) Suva Reef, Viti Levu, Fiji; (b) Uitoe01, New Caledonia; (c) Poindimié, New Caledonia; (d) Anse Vata, New Caledonia; (e) Prony, New Caledonia] are indicated in the maps of Figure 3.3.1. Satellite derived daily SSTSAT (product ref. 3.3.5) anomalies closest to each measurement platform have been added, respectively (grey line). Anomalies were calculated with respect to the annual climatology over the overlap periods.

0.009 ± 0.007 (Table 3.3.2). For New Caledonia at Poindimié, which is located in the north-eastern part of the country, the surface ocean warming trend is non-significant over the 25 years from both in situ and SSTSAT (Table 3.3.2). These in situ variations in local trends are related to the large spatial variability in trends (Figure 3.3.1) and to numerous local effects, combined with a high variability at interannual timescales (Quinn et al. 1998). At the southwestern part of New Caledonia, both stations Uitoe01 (Figure 3.3.4(b)) and Anse Vata (Figure 3.3.4(b)) show surface warming rates close to the global mean average, with Anse Vata covering the period February 1958 to early 2020. Rates of temperature change as derived from the satellite data underestimate the warming at these locations, in particular at Anse Vata (−36%) and Viti Levu (−62%).

Daily satellite and in situ time series correlations are all above 0.75, well above the significance level (Table 3.3.1). The maximum correlation was found for the logger deployed on the reef slope at Poindimié (0.87),

which is of the same order of magnitude as correlations found between SSTSAT and coastal temperature reported by other coral reef studies (Smale and Wernberg 2009; Van Wynsberge et al. 2017; Gomez et al. 2020). With respect to extreme amplitudes, the coloured, regular peaks in Figure 3.3.3 with the overlain satellite series in grey shows a prominent underestimation by satellite products. For a 'hot extreme' definition at two standard deviation, SSTSAT is on average lower by 0.9°C (Uitoé); 0.7°C (Vata); 0.4°C (Prony); 0.4°C (Viti Levu) and 0.3°C (Poindimié), with common excursions at 2°. Equivalently, SSTSAT can overestimate cold temperature by up to 4°C. Previous studies concluded that differences between SSTSAT and temperature recorded by *in situ* sensors deployed on outer reef slopes or in open and exposed lagoons were mostly due to vertical stratification (including a skin effect) of water and localised upwelling along the reef slope that generates lower *in situ* temperature than SSTSAT (Sheppard 2009; Castillo and Lima 2010; Claar et al. 2020). These

Table 3.3.2. Trend calculations during overlapping periods for SST time series from in situ reef loggers (ref 3.3.6) and the remote sensing product (ref 3.3.2).

Station	Station trend (°C/year)	ESA trend (°C/year)	Period
A- FJI Viti Levu Island 02	0.024 ± 0.01	0.009 ± 0.007	21/12/2012 to 31/12/2019
B- NCL Fausse Passe de Uitoe01	0.016 ± 0.002	0.013 ± 0.002	22/05/1992 to 02/12/2019
C- NCL Poindimié01	-0.0001 ± 0.002	-0.003 ± 0.002	09/12/1996 to 31/12/2019
D- NCL Anse Vata 01	0.011 ± 0.001	0.007 ± 0.001	01/09/1981 to 31/12/2019
E- NCL Récif du Prony 01	0.0048 ± 0.002	0.0001 ± 0.002	12/01/1996 to 31/12/2019

processes are unlikely to generate an underestimation of satellite-derived products which, particularly during summer months, are likely to result from higher variability in shallow coastal waters (see, e.g. the shallower sensor D-NCL Anse Vata located near the coast). This higher variability of temperature at local scale could not be captured by the spatial resolution of SSTSAT products (Stobart et al. 2008; Van Wynsberge et al. 2017; Gomez et al. 2020; Van Wynsberge et al. 2020). The underestimation of extremes that we find here

requires further analysis and needs to be adapted to relevant extreme indicators, e.g. DHW versus anomalies (see subsection 3.1 below) (Figure 3.3.2).

3.3.2.3.2. Chl-a. Just south of Fiji (Figure 3.3.3(A)), daily (Figure 3.3.3(B)) and monthly (Figure 3.3.3(B)) images depict differences during the months of April and September within the same year. These two dates were chosen to illustrate a case of high Chl-a (> 0.6 mg.m⁻³) south of Fiji, extending as a large plume off the coast towards the South (April), and a case of low Chl-a (< 0.4 mg.m⁻³) and no plume (September). For comparison, tropical oligotrophic open ocean Chl-a ranges from 0 to 0.35 mg.m⁻³ (Dupouy et al. 2018b). For the dates of the Bula cruises, CMEMS daily data were available only on September 2, 2003. Very few daily non-gridded data (product ref 3.3.2, Figure 3.3.3(B)) are available due to heavy cloud cover over this highly convective region, in particular over land and near coasts (Vincent et al. 2011). As a result, we had to rely on the monthly gridded composites (product ref 3.3.4) for our comparison with in-situ Chl-a observations.

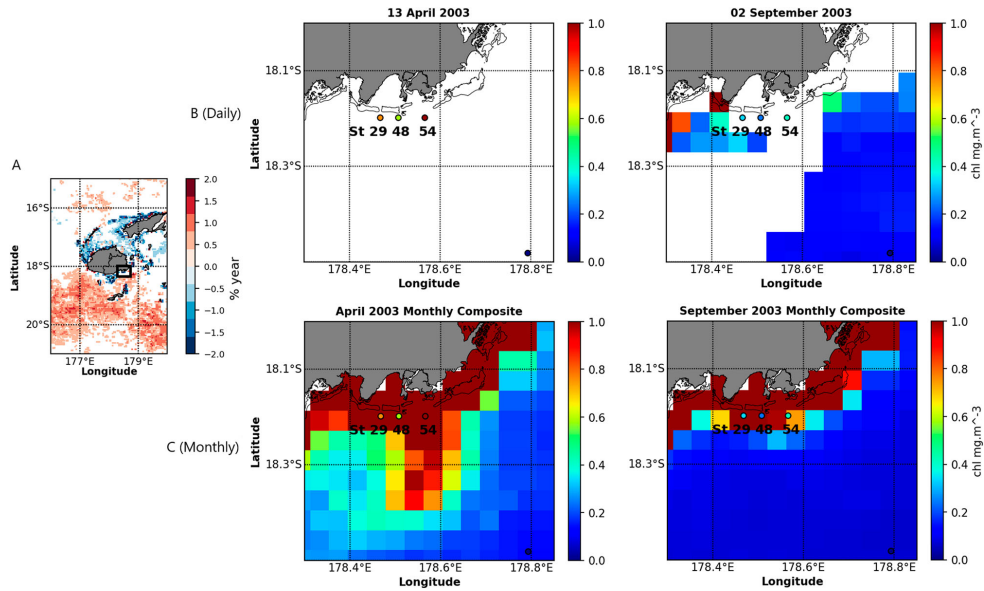


Figure 3.3.3. Chl-a observations: (A) Study area (black outlined box) in proximity to the wider Fiji zone, with Chl-a change (from product ref 3.3.1) (B) Chl-a in the proximity of Fiji in April and September 2003 for the day of the Bula cruise (product ref 3.3.2). In situ data are represented by the coloured circles, on the same colour scale (product ref 3.3.3) (C) Same as (A) based on the monthly Chl-a product (product ref 3.3.1), for April 2003 and September 2003. The two off-shore stations discussed are station 29 and station 48. Station 54 was discarded because of the Rewa river influence. The black dot to the south (178.79°E, 18.48°S) in ‘bluest water’ corresponds to a station sampled on October 2009 (product 3.3.7).

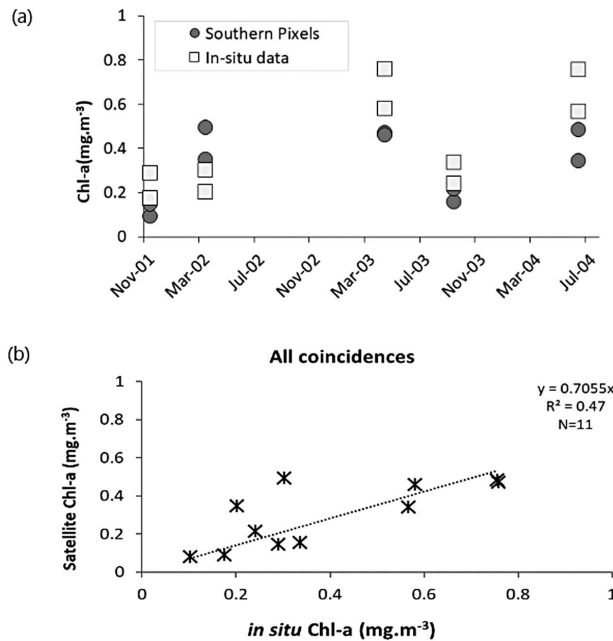


Figure 3.3.4. (a) Chl-a time series of monthly satellite-derived CMEMS Chl-a (product ref. 3.3.1) south of the position of the Bula stations 29 and 48 (grey bullets 'Southern Pixels'), and in situ Chl-a (product ref. 3.3.3) measured by fluorimetry (open squares) for the 5 Bula cruises (Bula 1: 6–11 Nov 2001, Bula 2: 12–19 March 2002, Bula 3: 12–22 May 2003 Bula 4: August 30–September 9, 2003; Bula 5: 5–15 June 2004) and for the S288 Seamans October 2019 cruise (b) Linear regression graph for Bula + Seamans data.

Among the Bula cruise data, two stations (St 29 and St 48) were sampled in open waters (Case 1 waters, behind the reef passages in Figure 3.3.3(B,C)). April and September monthly CMEMS products show Case 2 waters (in brown) near the coast. To avoid contamination by land in the CMEMS Case 2 waters, we selected pixels directly to the south of those stations for our comparisons. Station 54 is at the same distance from the coast, but was discarded because it is under the influence of the Rewa river output (Singh and Aung 2008) with high variability in Chl-a values linked to heavy and episodic sediment loads (Fichez et al. 2006).

Monthly satellite and instantaneous in-situ Chl-a for stations 29 and 48 are correlated despite the high temporal and spatial interpolations or smoothing (Figure 3.3.4(a)). The correlation is significant at 99% ($r^2 = 0.47$, $N = 11$) (Figure 3.3.4(b)).

Temporal evolution of monthly satellite Chl-a at these stations during the 1997–2021 period shows. An increase in variability of Chl-a in 2007 and 2011 at all stations (Figure 3.3.5). The generally higher mean Chl-a value at station 54 (mean Chl-a = 0.53 mg.m^{-3}) confirms the impact of the Rewa river episodic

runoffs. It superimposes with seasonal and interannual cycles observed at stations 29 (mean Chl-a = 0.37 mg.m^{-3}) and 48 (mean Chl-a = 0.47 mg.m^{-3}). The Rewa River also increases the number exceedances of a 0.53 mg.m^{-3} threshold: 33% of the time for station 54, 24% for station 48 and 5% for station 29. In contrast, the reference point far south of the 3 stations experiences low Chl-a and a more regular seasonal cycle.

3.3.3. Discussion

3.3.3.1. Strengths and weaknesses of the EOVS SST and chl-a products as indicators

We used five pilot sites in New Caledonia and Viti Levu in Fiji to provide insights about CMEMS SSTSAT and Chl-a products strengths and limitations (subsection 3.3.2.2.3 above) for potential application in an ecosystem monitoring and management framework. We found that the bias in SSTSAT products is important when considering extreme events, but acceptable when characterising long-term local changes, with respect to previous studies that find stronger biases (e.g. Sheppard 2009; Castillo and Lima 2010). This may be explained by

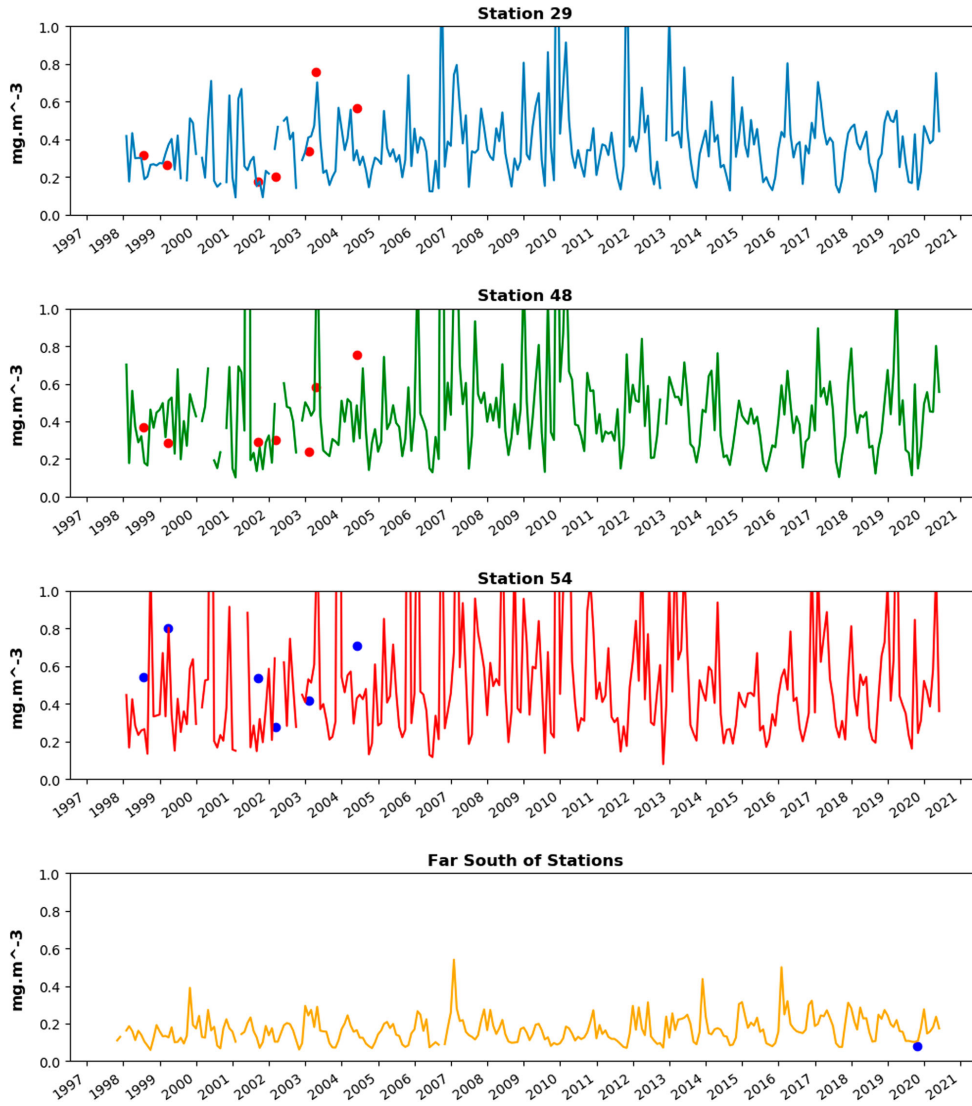


Figure 3.3.5. Satellite-derived monthly Chl-a (ref. 3.3.1) at a pixel just south of the in-situ stations st 29, st 48, st 54 and our reference point to the south (see Figure 3.3.3(B)). St 54 is heavily impacted by the Rewa river and therefore not included in the correlation analysis. Variability is much lower at the reference point to the south. The red and blue dots indicate in the Bula situ data (ref. 3.3.3).

the fact that these sites are either well-flushed with open-ocean waters (sites B-NCL, C-NCL, and A-Fiji), or face a lagoon that includes SSTSAT product pixels (sites D-NCL & E-NCL). Trend biases found here may therefore be unrepresentative of other reef and lagoon configurations that can be encountered in the Pacific

region. Extreme warm ocean temperature, or ‘Marine Heat Waves’ (Holbrook et al. 2019; Oliver et al. 2021; Dayan et al. 2022; de Boisseson et al. 2022), which have major influences on ecosystems, are underestimated although their observation and predictions are essential for marine managers for adaptation and

mitigation efforts. Specific analyses are necessary to assess precisely the relation between in situ and satellite-derived time series extremes (Holbrook et al. 2019).

SSTSAT products can provide gridded data on a quasi-real time basis, offering both adequate spatial and temporal resolution. The highest spatial resolution gridded product (L4) is 1 km (Merchant et al. 2019, product ref. 3.3.5), but its effective resolution is coarser. It is relevant for sufficiently wide water bodies (Van Wynsberge et al. 2020) but not for many coastal areas, in particular the complex lagoons and coral reefs relevant to the monitoring aspirations of this study. In contrast, in situ temperature loggers provide high accuracy on a small-scale local level. For coral bleaching applications, *in-situ* loggers can detect very localised temperature peaks caused by poor water circulation, local weather conditions, and water column stratification, or mass exchanges between inner lagoons and outer reef areas. Loggers, however, often provide short time series or series affected by gaps which limit their use for monitoring climate change. To properly describe a given coastal area for monitoring purposes, sensors must be deployed to capture a diversity of depth and reef locations, though very few have real-time transmission possibilities, which limits their practical use in many remote coral reefs. Modelling *in situ* temperature from SSTSAT on the basis of (shorter) temperature time series from loggers (Van Wynsberge et al. 2017) provides a promising downscaling approach to reconstruct long time series at the very local scale, but must be performed case-by-case to account for local specificities in hydrodynamics, reef configuration as well as lagoon size and depth (Van Wynsberge et al. 2017; Reid et al. 2020).

Our results have also explored the relevance of Chl-a products to environmental management. Ocean colour offshore the barrier reefs and south of the Fiji in-situ stations provides the decadal trends and responses of phytoplankton biomass through its Chl-a concentration. The observed increases in Chl-a may originate from the influence of terrestrial inputs such as sediment and dissolved organic matter transports, and ultimately can trace the dissemination of contaminants and responses of pelagic communities to increased nutrient inputs around Fiji (Fichez et al. 2006; Gassner et al. 2019), with potential effects on fish species and fish recruitments in offshore waters around the Fijian reefs. Chl-a increases can also indicate a change in phytoplankton composition (Dupouy et al. 2018a). As for temperatures, the biological activity and associated coastal water colour are influenced by many factors including small scale oceanic processes, human activities and sediment input, and it remains critical to relate

satellite data to in situ data before any usage in a monitoring framework.

In situ Chl-a data are much harder to acquire than temperature data, and therefore rare. Our Fijian case study illustrates that a monthly CMEMS Case 1 product partially reproduces the in-situ, instantaneous data for the 5 dates considered here. Case 2 Chl-a pixels were not used as they require different and adapted algorithms. Despite its design for large scale applications, the monthly CMEMS product shows a significant relationship with the limited coastal in situ data set that is available (Figure 3.3.4(b)), with some biases. It may therefore contain temporal and spatial information on oceanic variability around the islands, but its further use for monitoring is subject to validation with in situ Chl-a.

Our analyses of temperature and Chl-a time series therefore point to the advantage in having both in situ and remote sensing data for the same geographical areas. In-situ data are essential for accuracy monitoring at small spatial scales (e.g. local reef temperature, coastal ocean water quality), and in particular for extreme events. In situ measurements represent true local conditions, but with a necessarily limited coverage in time and space; whereas remote sensing data have broader coverage but are necessarily limited in terms of resolution and local accuracy. The corresponding data products and interfaces need therefore to be design according to local needs, as we discuss below.

3.3.3.2. A potential way forward: A co-construction monitoring framework using an integrated, transdisciplinary, multi-scale approach

Unprecedented and amplified impacts of ocean climate change occur at local scales, and adaptation measures (including socio-technical, political, cultural and or institutional innovations) and strategies need to be informed and designed at the regional and local levels. Actions need to be implemented in an integrated, transdisciplinary and multi-scale framework (Máñez Costa et al. 2017; Rölfer et al. 2020; Celliers et al. 2021). The UN Decade of Ocean Science for Sustainable Development provides a foundation to help achieve this objective and to ensure science responds to the needs of society 'to reverse the decline in Ocean health' by promoting codesign approaches (Ryabinin et al. 2019; GOOS 2022). Ocean products that are designed under global frameworks offer critical insights on general ocean change, variability and their drivers, but it may either be under-utilised or mis-utilised at local scales for various reasons: (1) other factors may need to be considered when working on mitigation or adaptation of an ecosystem (ecosystem/nexus approach); (2) the

understanding by local actors about ocean climate change consequences may differ substantially from the scientific understanding underpinning the global monitoring frameworks; (3) local specificities challenge the downscaling or upscaling techniques; and (4) potential consequences can generate unanticipated and negative local effects.

To address these issues in Oceania and following Belmont Forum and Ocean Decade initiatives, we promote here the following considerations for stakeholders, including scientists, public officers and citizens of the Pacific Islands to share common objectives and actions in order to achieve environmental sustainability when designing monitoring systems:³

- (1) *Ecosystem approach* (Skern-Mauritzen et al. 2016; Liu et al. 2018): Consideration of an ensemble of stressors, including environmental, socio-economic, cultural and political aspects (Zhang et al. 2021).
- (2) *Shared understanding*: Local understanding and representation climate change impacts depends on knowledge, values, drivers, barriers and opportunities. The accessibility and utility of products for stakeholders needs to come with a shared understanding of climate change impacts and indicators (Kaiser et al. 2019; Mackenzie et al. 2019; Vargas-Nguyen et al. 2020).
- (3) *Scalability in coastal areas*: Globally based indicators may miss important issues as revealed by local experience and combining and matching needs and knowledges produced at different scales and from different ontological viewpoints entails combining heterogeneous elements that cannot be ‘added’ to one another in many cases (‘non-scalability’) (Tsing 2012, 2015), nor generalised to other places (see Bergthaller et al. 2014 on ‘the practice of environing’).⁴
- (4) *Forecast ethics*: Delivery of forecast products can have heavy consequences, given uncertainties, or generation of inequalities from unbalanced capacities to use it, and therefore needs to come with ethical considerations that include engagement and equity for end users (Hobday et al. 2019).

To produce those relevant indicators, extend existing EOVs (or implement new EOVs), and build interest and ability to use them, bottom-up driven consultations and developments are essential steps (e.g. Claudet et al. 2020). Such participative framework can foster an enriching dialogue, provide new insights about socio-ecological processes, and contribute to augment the perception of unprecedented ocean

changes (Johannes 1981; Hviding 2005; Singh et al. 2021). Indigenous peoples and local communities (IPLC) can actively contribute to the process.⁵ For instance, IPLC knowledge in combination with remote sensing allowed efficient mapping of the tropical marine habitat of the Solomon Islands (Lauer and Aswani 2008). Combined analysis of fishermen’s local knowledge with remote sensing data for SSTSAT and Chl-a can lead to participatory mapping of fishing grounds (Rahimi bin Rosli 2017; Mason et al. 2019) and support marine conservation and management (Aswani and Hamilton 2004; Aswani and Lauer 2006). (See McNamara et al. (2020) and Chambers et al. (2021) for a review of such co-constructed projects for sustainability.) The identification and synthesis of data and knowledge sources by structured consultation with project partners, scientists, and stakeholders is therefore needed to take the next steps toward a co-designed monitoring framework (Vargas-Nguyen et al. 2020), including locally based and globally produced knowledge (Hviding 2003; Strang 2009; Sterling et al. 2017).

In Oceania, these efforts will come in support of ongoing projects, in particular, the SPC-lead Pacific Community Centre for Ocean Science (PCCOS) programme⁶ for delivering integrated scientific services supporting ocean management, governance and observations; the Pacific Data Hub⁷ as well as the Digital Earth Pacific⁸ that aim at gathering available data and make it available for Pacific Member States to make more informed decisions and report their progress toward the United Nations SDGs,⁹ and the recent USP/UNC Master in sustainability.

Section 3.4. Consistent data set of coastal sea level: The synergy between tidal gauge data and numerical modelling

Authors: Sebastian Grayek, Emil Stanev, Nam Pham, Antonio Bonaduce, Joanna Staneva

Statement of main outcome: The multiannual (1993–2020) variability of sea level in the Baltic Sea is reconstructed by applying a Kalman filter approach. This technique learns how to generate data sets with the same statistics as the training data set, which in the studied case was taken from the CMEMS Baltic MFC operational model. It is demonstrated that using tide gauge data and statistical characteristics of the Baltic Sea from the model enables the generation of a high-resolution reconstruction of the sea surface height. Results obtained in this study demonstrated that the reconstruction method offers comprehensive high-resolution estimates (space and time) of sea level variability in the

Baltic Sea based on tide gauge observations with high temporal resolution (e.g. hourly). The approach represents a valuable extension to the existing observing capabilities from altimetry, which do not capture sub-daily variations of sea level (e.g. storm surges). At the same time, the method consumes only a small fraction of the computational resources required by an assimilative model with comparable temporal/spatial resolution.

Product used:

Ref. No.	Product name and type	Documentation
3.4.1	BALTICSEA_ANALYSISFORECAST_PHY_003_006 Model analyses	PUM: https://catalogue.marine.copernicus.eu/documents/PUM/CMEMS-BAL-PUM-003-006.pdf QUID: https://catalogue.marine.copernicus.eu/documents/QUID/CMEMS-BAL-QUID-003-006.pdf
3.4.2	BALTICSEA_REANALYSIS_PHY_003_011 Model reanalysis	PUM: https://catalogue.marine.copernicus.eu/documents/PUM/CMEMS-BAL-PUM-003-011.pdf QUID: https://catalogue.marine.copernicus.eu/documents/QUID/CMEMS-BAL-QUID-003-011.pdf
3.4.3	INSITU_BAL_NRT_OBSERVATIONS_013_032 In-Situ Data	PUM: https://catalogue.marine.copernicus.eu/documents/PUM/CMEMS-INS-PUM-013.pdf QUID: https://catalogue.marine.copernicus.eu/documents/QUID/CMEMS-INS-QUID-013-030-036.pdf
3.4.4	ERA5 Copernicus Climate Change Service (C3S) (2017): ERA5: Fifth generation of ECMWF atmospheric reanalyses of the global climate. Copernicus Climate Change Service Climate Data Store (CDS), 2021.	https://climate.copernicus.eu/climate-reanalysis
3.4.5	Baltic Sea reconstruction SSH data.	Method after Zhang et al. (2020)

3.4.1. Introduction

Regional sea level variability and trends in the Baltic Sea have been largely studied using tidal gauge measurements. Satellite altimetry added critical additional information in the last 30 years (Madsen et al. 2015). However, different measurement techniques have different advantages and drawbacks. Satellite-derived sea level information, which has revolutionised oceanography and climate science, particularly addressing global and large-scale change, are of limited use when addressing the near-coastal short periodic variability. However, advancements are underway, and new satellite missions characterised by better spatial and temporal sampling pave the way for improvements of coastal sea level research (e.g. CCI 2020; Dieng et al. 2021; Prandi et al. 2021). The importance of enhanced altimetry for coastal and sea-ice covered areas in the Baltic is demonstrated by Passaro et al. (2021).

Tidal gauges provide precise estimates with high resolution in time in specific locations at the coast, but do not provide information about the basin-wide patterns of sea level. Furthermore, these data are not continuous; different gauges do not always operate simultaneously; there are gaps in many of the records. A question arises as to whether one can combine data from gauges and independent 2D maps of sea level (from models) with the aim of producing a consistent data set (covering all coastal locations at the same times and with high temporal resolution). A similar exercise has been undertaken recently by Zhang et al. (2020) for the North Sea and by Madsen et al. (2019) for the Baltic Sea. However, the reconstructions of Zhang et al. (2020) covered rather short periods. The ones of Madsen et al. (2019) were provided for the period 1900–2014, however their resolution was rather coarse. In the present paper, we use a Kalman filter technique and apply it for a thirty-year period, which is approximately the length of the available altimeter data series. This period is long enough to address climate modes such as the North Atlantic Oscillation (NAO), which are known to be a major driver of sea level variability in the Baltic Sea (Andersson 2002; Hünnicke et al. 2015).

The Baltic Sea is a relatively shallow basin where dynamics are largely determined by wind-driven processes (Jacob and Stanev 2017; Hordoir et al. 2018; Placke et al. 2021). Another important driver of sea level in this basin comes from fresh water fluxes. Because of its small size and the rather narrow connection with the open ocean, tides are small and do not penetrate much further than into the straits connecting the North and Baltic Seas (Stanev et al. 2015). At short time scales, standing waves dominate the variability

with approximate periods of 31, 26, 22, and 20 h (Wüßner and Krauss 1979). These eigenfrequencies for the Baltic were confirmed by Meier (1996). Jönsson et al. (2008) demonstrated that basin oscillations can be regarded as an ensemble of weakly coupled ‘gulf modes’ or ‘harbor modes’ in the individual sub-basins.

The present study uses model data and tidal gauge observations as a basis for the analysis of sea level variability. The aim is to (1) illustrate the capabilities of the method used to reconstruct basic patterns of sea level variability, (2) identify the patterns of long-term variability of sea level in the Baltic Sea, (3) assess specific characteristics in the sea level variability in recent years, and (4) identify possible improvements for future estimates.

3.4.2 Methods and data used

The reconstruction method uses the techniques described by Schulz-Stellenfleth and Stanev (2010) and is similar to the approach described by Frolov et al. (2008). This method has been used by Grayek et al. (2011) to derive basin scale estimates of surface temperature and salinity in the German Bight from FerryBox measurements. Recently, Zhang et al. (2020) applied it to reconstruction of the basin-wide sea-level variability in the North Sea. They demonstrated that the method enables high skill, comparable to the skill of a method based on generative adversarial networks (Goodfellow et al. 2014; Gurumurthy et al. 2017).

The method estimates for the entire Baltic Sea comprehensive hourly maps of sea surface height (SSH) according to a priori information on spatial covariance of SSH using a linear combination of measurements from coastal stations (in our example up to 28 tidal gauges). The tide gauge data comes from the historical and near real-time data set of the Copernicus Marine Environment Monitoring Services (CMEMS) ‘Baltic Sea – In Situ Near Real Time Observations’ product (Copernicus Marine In Situ TAC Data Management Team 2020, product ref. 3.4.3). Another 46 tide-gauge stations from the same data set are used as independent data for validation. The original CMEMS data has a high temporal sampling (between 10 min and 1 h). In this study, we use hourly gauge data, hence higher frequency observations were subsampled to one hour. For a better reading, we will use in the following text the abbreviations ‘TGD-P28’ and ‘TGD-P46’ for the hourly data sets containing the 28 tide-gauges for reconstruction and the 46 tide-gauges for validation, respectively. The positions of the tide-gauge stations together with the names and abbreviations of the stations used for the reconstruction are shown in Figure 3.4.1. The ‘Auxiliary Data’ section

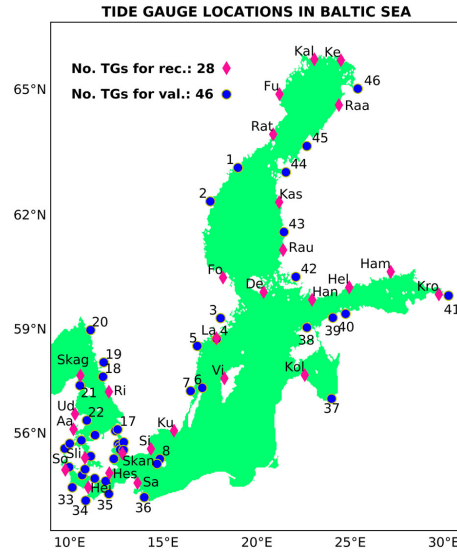


Figure 3.4.1. Tide gauge locations in the Baltic Sea. The names of the tide gauges used for validation (blue circles) are given in the ‘Auxiliary Data’ section. The list of abbreviations and names of the tide gauges used for reconstruction TGD-P28, (pink diamonds) we show also here. Aa, Aarhus; De, Degerby; Fo, Forsmark; Fu, Furuogrund; Ham, Hamina; Han, Hanko; Hei, Heiligenhafen; Hel, Helsinki; Hes, Hesnaes; Kal, KalixStoron; Kas, Kaskinen; Kem, Kemi; Kol, Kolka; Kro, Kronstadt; Ku, Kungsholmsfort; La, LandsortNorra; Raa, Raahe; Rat, Ratan; Rau, Rauma; Ri, Ringhals; Sa, Sassnitz; Sim, Simrishamn; Skag, Skagen; Skan, Skanor; Sli, Slipshavn; So, Sonderborg; Ud, Udbyhoej; Vi, Visby. Products used: ref. 3.4.3 (TGD-P28, TGD-P46).

includes a complete list of all tide gauge station’s positions, names and their abbreviations.

For the training of the reconstruction algorithm, we use as proxy data for the period 01/01/2019–31/12/2019 outputs from the operational model of the SMHI (Swedish Meteorological and Hydrological Institute) BAL MFC-NEMO (product ref. 3.4.1). These data are referred to as the ‘Baltic Sea Physics Analysis and Forecast’ product of the CMEMS Baltic Monitoring and Forecasting Centre (BAL MFC). We will use the abbreviation ‘ANL’ for this data set further on in the text. We define the global state vector \mathbf{x} as the data set, which contains hourly maps of SSH over the entire Baltic Sea. The measurement vector \mathbf{y} is assumed to represent the observations from the coastal stations (see Figure 3.4.1). In our training step, we use for the measurement vector proxy measurements from the model and postulate the following relationship.

$$\mathbf{y} = H\mathbf{x}, \quad (3.4.1)$$

where H is called the linear measurement operator. These proxy measurements are without temporal gaps or measurement errors. In the following, it is assumed that the state vector \mathbf{x} and the measurement vector \mathbf{y} have their temporal mean removed, thus, they describe the departures of sea level \mathbf{x}' from a reference sea level \bar{x}_i , which is considered as the temporal mean over the training period (01 January 2019–31 December 2019).

The task for the training is to find a linear reconstruction matrix A , which applied to the data in the positions of observations (gauge stations), could reconstruct the Sea Level Anomaly (SLA) over the entire area. Such reconstruction would be optimal if the cost function

$$J(A) = \sum_{j=1}^q \mathbf{x}(t_j) - A\mathbf{y}(t_j)^2 \quad (3.4.2)$$

is minimum, where q is the number of hourly maps used for the training. This would ensure that the reconstruction error is as small as possible. Schulz-Stellenfleth and Stanev (2010) showed that $J(A)$ is minimum if A is the Kalman gain matrix

$$A = PH^T(HPH^T + R)^{-1} \quad (3.4.3)$$

where P is the background covariance matrix for the state \mathbf{x} and R is the observation error matrix for the measurements \mathbf{y} . There are some limitations to the method and we refer to the work of Janjić et al. (2018) for more details on how to overcome them. In the present work, we use for R a diagonal matrix with a constant observation error of 1 cm. For P we use empirical orthogonal functions (EOFs; Preisendorfer and Mobley 1988) of the entire Baltic Sea estimated during the training period. A well-known advantage of the described design is that only a few EOFs are needed to give a good approximation of the covariance information in P , which significantly reduces the dimension of the reconstruction problem and makes the calculation of A efficient. In order to catch the long-time variability over decades, which for the Baltic Sea represents a marginal part of the total variance, we build P from the leading 30 EOFs, which describe more than 99.5% of the total variance. An analyses of these EOFs can be found in the appendix of the study (Appendix A; Analyses of proxy data used for the training of the reconstruction method.).

Figure 3.4.2 illustrates the validation of the training, quantified as the mapped root mean square error (RMSE) of the reconstruction for the training period,

$$\text{RMSE}_i = \sqrt{\frac{1}{q} \sum_{j=1}^q (\mathbf{x}_i(t_j) - A_i\mathbf{y}(t_j))^2} \quad (3.4.4)$$

where i denotes the individual position. Because the design of the training provides perfect observations for the method (no measurement errors), the errors in the reconstruction emerge from the missing linear correlation between the observed and the remote positions in the training data set. It is not surprising that the lowest errors are found along the coast and close to the position of gauge stations because these regions can be expected to have higher linear correlation with the data in the gauge stations. RMSEs in the region of the Skagerrak, Kattegat, Great Belt, Sound and the eastern part of the Gulf of Finland are in general higher, due to limitations of the reconstruction approach to reproduce the complex dynamics in these regions. Higher errors in the Bornholm basin and along the Polish coast are due to the lack of observations there (compare Figure 3.4.1).

The application of the Kalman filter approach described above, as well as the application of generative adversarial networks to reconstructing basin wide sea level in the North Sea has been addressed in detail by Zhang et al. (2020). Advantages and limitation of the method are described in that study, therefore, we will not repeat here the exercise of these authors but give a brief overview. One message of their study was that substituting the proxy (model gauges) by data from real observations decreases the quality of the reconstruction skill. One reason for this is that the correlation patterns of the training data set not necessarily mirror correlations between real observations, which limits the reproducibility of the real observations in the reconstruction. The decomposition of correlation patterns

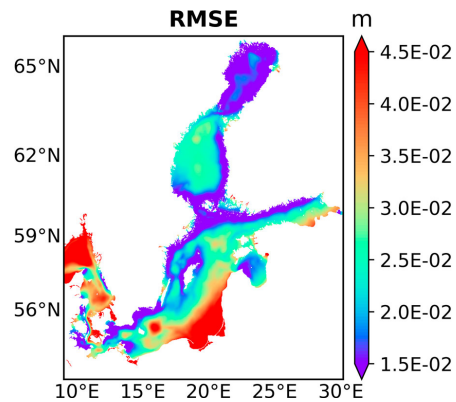


Figure 3.4.2. The performance of the reconstruction method expressed as the RMSE difference between the global state \mathbf{x} and its reconstruction during the training period. Product used: ref. 3.4.1 (ANL).

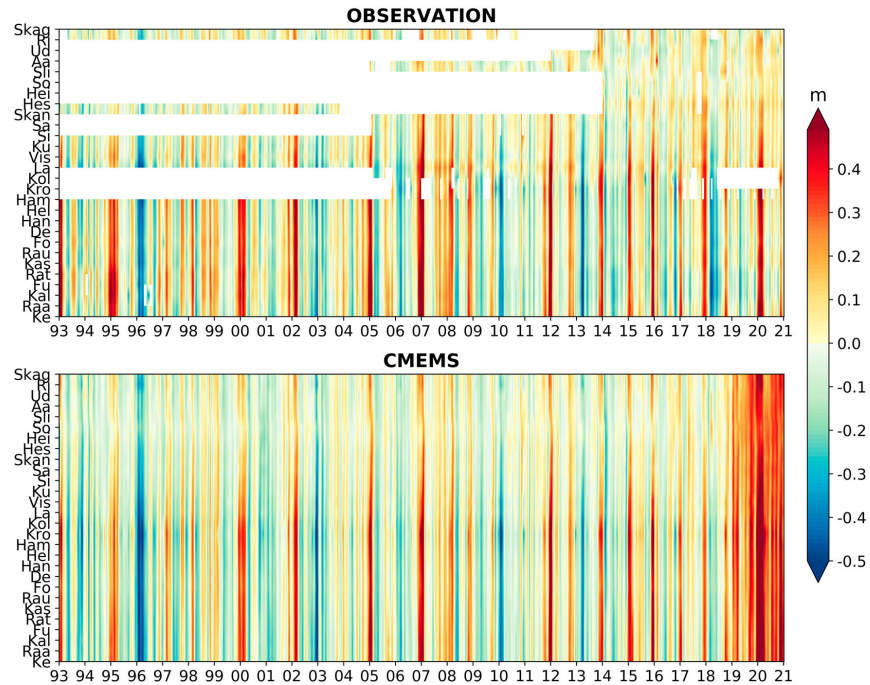


Figure 3.4.3. Comparison between tide gauge observations (top) and numerical simulations (bottom) in the locations used for training (28 tide-gauge locations, compare Figure 3.4.1), but for the longer than training period. Products used: ref. 3.4.1 (ANL), ref. 3.4.2 (REA) and ref. 3.4.3 (TGD-P28).

into EOFs is only partially able to overcome this limitation. In general, the method is better able to deal with missing or underestimated correlations than overestimated or spurious correlations, with smooth training data dominated by a few periodic signals with a limited number of frequencies (e.g. tides) giving more vulnerable EOFs. In the present work, we will propose an extended approach, which could be considered as an enhancement of model data by real observations. We build our approach on strengthening the synergy between observations and numerical simulations. Expressed in another way, the method can be considered as a posteriori ‘assimilation’ of coastal data. The advantage over the method described in Zhang et al. (2020) is that, instead of reconstructing the observations, we reconstruct the misfit between the observations and the numerical simulations, which we believe to have a better chance to be representable by the correlation patterns of the training data than the observations themselves.

The reconstruction period (1993–2020), which we target is longer than the training period, that is the model

solution and observations are independent data from the ones used in the training. We use the same reconstruction matrix A as derived during the training phase. However, as mentioned above, instead of using proxy measurements, as we did during the training phase, we will use in the following real measurements from the data set TGD-P28. We will denote the real observation as y_o . The subscript ‘o’ stands for ‘observations’. Our basic assumption is that the background covariance matrix P is representative not only for the training period, but also for the validation period. The algorithm uses SSH fields, not SLA, from numerical simulations as a first guess and calculates updated fields based on real measurements. Simulation data for the year 2020 is derived from the same CMEMS product (ANL, product ref. 3.4.1) as the training data set. The period from 1993 to 2018 is available from the ‘Baltic Sea Physics Reanalysis’ CMEMS product (product ref. 3.4.2), see Hordoir et al. (2015) and Pemberton et al. (2017), for which we will use the abbreviation ‘REA’, in the following. For the longer reconstruction period, the linear measurement operator H and the reconstruction matrix A have to be considered as time dependent because

Table 3.4.1. Covered period and purpose for all data sets used during the training and application of the reconstruction algorithm. The abbreviation ‘ANL’ and ‘REA’ refer to the ‘Baltic Sea Physics Analysis and Forecast’ and ‘Baltic Sea Physics Reanalysis’ CMEMS products, respectively (product ref. 3.4.1 and ref. 3.4.2). ‘TGD-P28’ and ‘TGD-P46’ indicate the tide-gauge data sets including the 28 stations used for reconstruction and the 46 stations used for independent validation. Both data sets are derived from the ‘Baltic Sea – In Situ Near Real Time Observations’ CMEMS product (product ref. 3.4.3). ‘ERA5’ refers to the atmospheric data from the Fifth generation of ECMWF atmospheric reanalyses of the global climate product (product ref. 3.4.4) from the Copernicus Climate Change Service Climate Data Store (CDS). ‘REC’ stands for the SSH reconstruction based on Equation 3.4.5 (product ref. 3.4.5).

	Training	Application (REC)
Covered period of data sets	01/01/2019–31/12/2019	01/01/1993–31/12/2020 (if not stated otherwise)
Background Covariance	ANL	ANL (01/01/2019–31/12/2019)
First Guess for reconstruction	None	REA (01/01/1993–31/12/2018) ANL (01/01/2019–31/12/2020)
Observations for reconstruction	ANL, at positions of TGD-P28	TGD-P28
Validation	ANL	REA (01/01/1993–31/12/2018) ANL (01/01/2019–31/12/2020) TGD-P28 TGD-P46
Analyses	None	TGD-P46 ERA5

continuous observations over the whole validation period are not available from all gauges. Accordingly, the reconstructed state (\mathbf{x}_r) for the time t_j (hourly maps during the reconstruction) is presented as

$$\mathbf{x}_r(t_j) = \mathbf{x}(t_j) + A(t_j)[\mathbf{y}_o(t_j) - H(t_j)\mathbf{x}(t_j)] \quad (3.4.5)$$

This equation can be regarded as correction of model estimate $\mathbf{x}(t_j)$ by the second term on the right-hand side. In the case of using proxy data from the model instead of real observations $\mathbf{y}_o(t_j) - H(t_j)\mathbf{x}(t_j) = 0$, the solution is $\mathbf{x}(t_j)$. The deviation between coastal observations and model data on the coast tends to correct $\mathbf{x}(t_j)$ basin wide. As far as biases are concerned, because of the different training and reconstructing periods, they are in the range of few millimeters, which is far below the achievable accuracy for the reconstruction method (see Figure 3.4.2). Therefore, they are not considered. Quantifying the effect of possible biases in additional experiments (not presented here) showed little to no gain in the reconstruction’s performance. We will use in the following text the abbreviation ‘REC’ for the reconstructed state estimates (product ref. 3.4.5).

Figure 3.4.3 illustrates the availability of gauge measurements in the TGD-P28 data set and their consistency with the REA and ANL data from the Baltic Sea CMEMS numerical simulations. Basic SSH events during the period covered by REA (1993–2018) are coherent in the two data sets and no obvious bias is observed for this period. For the rest of the time (2019–2020), which is covered by the ANL data, we find a positive bias in comparison to the TGD-P28 data. To understand the reason for this, we performed experiments with an independent model that included the same region. These experiments showed a comparable bias in SSH after 2018. Subsequent analyses of the forcing data for the lateral open boundaries (CMEMS) and the surface (ERA5, product ref. 3.4.4) showed no suspicious changes in the spatial patterns or absolute values between 2017 and 2019, so we suspect that noise accumulation is the cause of the bias. However, a more detailed investigation in the future may prove otherwise. Another problem is that in the transition area between the North Sea and Baltic Sea, continuous observations are available only after 2013. Because of these two reasons, it is expected that the performance of the reconstruction will be inferior in that region for the period before 2013 and in the time after 2018.

Table 3.4.1 summarises for all data sets used during the training and application of the reconstruction algorithm the period covered, the intended use, and their abbreviation in the text. In addition, the corresponding product references are given in the table’s caption where appropriate.

3.4.3. Results

The validation of the reconstruction is performed at the coastal station positions and takes into consideration the measurements, which are not used in the reconstruction. Figure 3.4.4 shows a comparison between the reconstructed sea-level signals and those retrieved from observation- and model-based data sets. In particular, we assess the reconstruction in terms of correlation with the observations (left), and skill compared to CMEMS simulations (right). The latter is defined as

$$\text{RMSE}_r = \sqrt{\frac{1}{N} \sum_{j=1}^N [H_j \mathbf{x}_r(t_j) - y_o(t_j)]^2} \quad (3.4.6)$$

$$\text{RMSE}_c = \sqrt{\frac{1}{N} \sum_{j=1}^N [H_j \mathbf{x}(t_j) - y_o(t_j)]^2} \quad (3.4.7)$$

$$\text{SKILL} = 1 - \frac{\text{RMSE}_r}{\text{RMSE}_c} \quad (3.4.8)$$

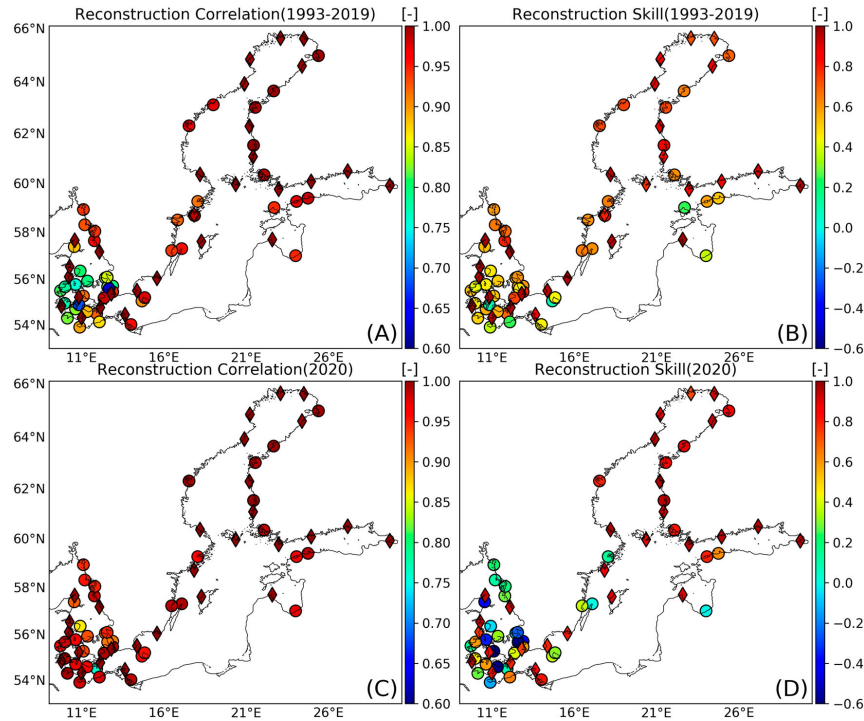


Figure 3.4.4. Correlation against observations (left-hand side) and Skill against SMHI data (right-hand side) of the reconstructions for the periods 1993–2019 (top) and 2020 (bottom) at the 46 independent (circles) and 28 dependent (diamonds) tide gauge locations. Products used: ref. 3.4.1 (ANL), ref. 3.4.2 (REA), ref. 3.4.3 (TGD-P28, TGD-P46) and ref. 3.4.5 (REC).

where $RMSE_r$ and $RMSE_c$ are the errors obtained by comparing the observations with the reconstructed sea-level and CMEMS model outputs, respectively. N is the number of available observations during the investigated periods. Results are shown for two periods: 1993–2019 (top) and for 2020 (bottom). The first period is covered by the REA data set and the part of the ANL data (2019, product ref. 3.4.1) that was used for training. The second period is covered by the portion of the ANL data (2020) that is independent from the training. The diamond and circle symbols correspond to the gauge locations that were used (TGD-P28) or not used (TGD-P46) in the reconstruction, respectively. The general conclusion is that the correlation and the skill of reconstruction are good, except for the straits connecting the North and Baltic Seas. This is probably related to the limited ability of the reconstruction design to reproduce the dynamics in this region. We have already addressed this issue in the validation of the training period (see Figure 3.4.2). Another reason for the inferior

performance is the lack of observations in the area. In general, the gaps in the time series of measurements during the period 1993–2019 (see Figure 3.4.3) affect the quality of the reconstructions. In contrast, if we consider a period when continuous in-situ records were available, the correlation between observations and reconstructions improves significantly (e.g. in 2020, Figure 3.4.4(C)). Whereas we attribute the concurrent decrease of the skill for the region (compare Figure 3.4.4(B) and Figure 3.4.4(D)) to a better performance of the ANL simulation rather than to a lowered performance of the reconstruction. There are other regions, such as the Gulf of Riga, where the validation is rather poor in both periods (circle symbols in Figure 3.4.4(B, D)). For this area, the data set of the only tide gauge station used for reconstruction, ‘Kolka’ (Kol), has significant gaps in both periods. However, high negative skills are found only for 2020 and at some stations in the transition zone between the North Sea and the Baltic Sea and the straits, where skills are generally low (see

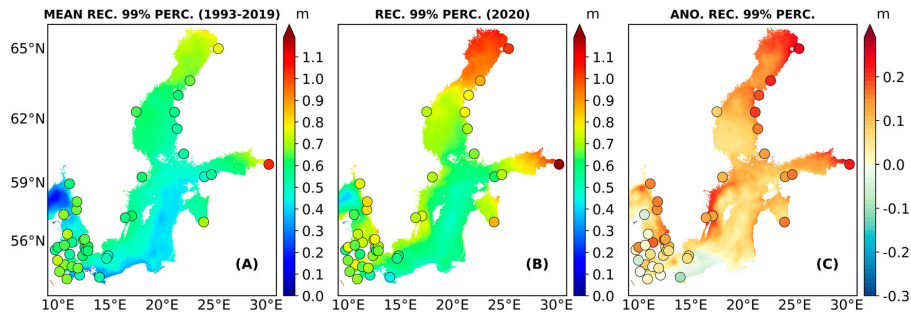


Figure 3.4.5. Mean yearly 99% percentile of SSH for the period 1993–2019 (A), the year 2020 (B) and the anomalies of the values in 2020 from the values of the rest of the period (C). The coloured maps and dots show the values derived from the reconstructions (REC) and independent tide gauges (TGD-P46), respectively. Tide gauge locations with insufficient observations are not shown in the panels. Products used: ref. 3.4.3 (TGD-P46) and ref. 3.4.5 (REC).

above). Further validation and statistics on the reconstructed data can be found in the appendix of the study (Appendix B; Extended validation and statistics of the reconstructed data).

The panels in Figure 3.4.5 show SSH 99th percentiles obtained considering the data sets REC and TGD-P46, where colours of the circular symbols represent the 99th percentiles as seen in the tide gauge data. The basin-wide reconstruction agrees well at the coastal stations with the independent coastal observations. The results show that over the period 1993–2019, the SSH extreme values reach maximum in the easternmost part of the Bay of Finland, as well as in the northernmost part of the Bothnia Bay (Figure 3.4.5(A)), which

are even intensified in these areas in 2020 (Figure 3.4.5(B,C)). In addition, the Swedish coast shows stronger-than-average values in 2020 (Figure 3.4.5(B,C)).

In the following, we address sea-level variations on interannual to longer time scales. Climate modes such as the NAO are known to be a major driver of sea level variability in this area and on these time scales. To further investigate the relationship between regional and global variability, we compare the reconstructed sea level anomaly over the period 1993–2020 with the NAO index at the regional scale during the winter season (December–January–February, DJF). As can be seen in Figure 3.4.6(A), the correlation between the reconstructed sea level anomaly and the NAO index reaches

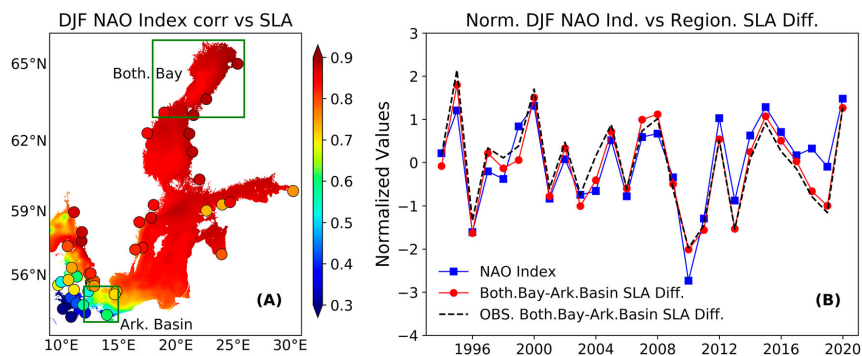


Figure 3.4.6. Correlation coefficient of the reconstructed sea level anomaly (map) and tide gauge observation (coloured circles) with the North Atlantic Oscillation (NAO) index during winter season (DJF, December–January–February) for the period 1993–2020 (A). Time series of the normalised DJF NAO index and normalised mean SSH differences between the Bothnia Bay and Arkona Basin (B) from REC (red solid line) and from TGD-P46 observations (black dashed line). Observations in the northern box (‘Botnian Bay’) are represented by the measurements derived from the stations: Kemi, KalixStoron, Furuogrund, Ratan, Skagsudde, Vaasa, Pietarsaari, Raahe and Oulu; Observations in the southern box (‘Arkona Basin’) are represented by the measurements derived from the stations: Simrishamn, Skanor, Rodvig, Hesnaes, Sassnitz, Koserow and Tejn. Products used: ref. 3.4.3 (TGD-P46), ref. 3.4.4 (ERA5) and ref. 3.4.5 (REC).

values above 0.8 in the inner Baltic Sea, while lower values are observed in the transition area to the North Sea. Similar results are provided by the comparison between the NAO index and the independent tide gauge data (TGD-P46, circles in [Figure 3.4.6\(A\)](#)) in the region, which generally supports the results obtained from the reconstruction. This regional change in the response to the NAO may be related to the complex dynamics in the region, which emerge from the interaction between the transport through the straits and the bathymetry (see e.g. [Haid et al. 2020](#)). Regions where the correlation coefficients derived from the tide gauge data and the values derived from the reconstruction differ are the Gulf of Riga and the Gulf of Finland. Here, the reconstruction slightly overestimates the correlation. The discrepancies along the southern coast and in the eastern part of the Gulf of Finland suggest that the spatial correlation patterns in this region may in fact be more complex than the reconstruction results suggest. In addition, we want to analyse the response of our reconstructed sea level anomaly to the NAO by evaluating the difference between the mean sea level anomaly at the southwestern opening of the Baltic Sea, the Arkona Basin, and the northern tip of the basin, the Bothnian Bay. Both regions are shown as green frames in the figure. The results of the reconstructed data (red solid line in [Figure 3.4.6\(B\)](#)) show the agreement between the normalised reconstructed sea level differences and the NAO index for the winter season and emphasise the influence of the large-scale external wind conditions on the sea level variability in the Baltic Sea. This result is confirmed by comparing the climate index with the observed sea level records (black dashed line in [Figure 3.4.6\(B\)](#)). The strong influence of the atmospheric patterns on the temporal evolution, shown in [Figure 3.4.6](#), indicates that the Baltic Sea can be considered as an almost perfect responder to the NAO, in line with the results of [Andersson \(2002\)](#) and [Passaro et al. \(2021\)](#).

3.4.4. Conclusions

Multi-year (1993–2020) sea level variability in the Baltic Sea is reconstructed using a combination of tide gauge observations (TGD-P28) and model-based data (ANL and REA). The results have shown that the dynamic model simulation (ANL) are able to provide a reliable basis for describing the spatial sea level correlation patterns, which are needed as an initial assumption for the reconstruction process. In addition, our study has demonstrated the ability of the algorithm to reconstruct sea level anomalies on different space and time scales.

Validation of the reconstruction algorithm with training data from the model simulation showed that it has limited ability to compensate for the unfortunate lack of tide gauge data along the Polish coast. Lower reconstruction performance is expected here and in the Bornholm Basin region, but could not be evaluated due to lack of other validation options. In addition, reconstruction performance in the transition zone between the North Sea and the Baltic Sea was shown to decrease during periods of lower local data coverage. The low correlation in this area with observations in the rest of the basin may also indicate that the region is governed by complex dynamics (see also [Zhang et al. 2016](#); [Stanev et al. 2018](#); [Haid et al. 2020](#)).

Our results showed that the extreme sea level anomalies in 2020 reached unusually strong values compared to the 1993–2019 baseline, especially in the northernmost and easternmost parts of the basin. Moreover, the strong relationship between sea level change in the Baltic Sea and the NAO was quantified.

Large parts of the Baltic Sea coast are endangered by storm surges. Due to their potential to cause devastating damages, the precise prediction of form, timing and duration of storm surges has a high societal impact. In order to achieve this high forecast skill, state-of-the-art model systems rely on the practices of observation data assimilation. However, the temporal availability of altimeter observations is often not high enough to catch storm surges with duration of hours to days. The results obtained in this study demonstrated that: reconstruction methods offer comprehensive high-resolution estimates (space and time) of sea level variability in the Baltic Sea based on tide gauge observations at high temporal resolution (e.g. hourly). This approach can be a valuable extension of existing observational capabilities from remote sensing ([Passaro et al. 2021](#)), as it can be used to fill temporal gaps typical of any observing system and track the temporal evolution of sea level patterns at high resolution. At the same time, the method consumes only a fraction of the computational resources required by an assimilative model with comparable temporal and spatial resolution.

Acknowledgments

The production of the results presented in this study used computational resources of the MISTRAL cluster system of the Deutsches Klimarechenzentrum (DKRZ) granted by its Scientific Steering Committee (WLA) under project ID bu1213.

Section 3.5. Wave climate extremes in the Mediterranean Sea obtained from a wave reanalysis for the period 1993–2020

Authors: Anna Zacharioudaki, Michalis Ravdas, Gerassimos Korres

Statement of main outcome: Climate change can alter the extreme wave climate of the Mediterranean Sea and consequently modify the risk posed on maritime structures and coastal environments. The annual 99th percentile of Significant Wave Height (SWH) – a measure of extremes – has increased almost everywhere in the basin during the last 28 years at a maximum rate of 0.026 m/year. The most significant upward trends were found in the south-eastern Levantine and eastern Alboran Seas, followed by the Adriatic Sea and contained areas of the Tyrrhenian. The same areas were found to be prone in terms of changes in wave storm characteristics such as frequency, intensity and duration, embedding statistically significant positive trends over this period. Additional regions with consistent positive trends include the Catalan coast and its offshore and the coast of Valencia, around the western end of the island of Crete and the north-east Aegean. Negative trends are not uncommon in wave storm intensity and duration, yet not statistically significant. No negative trends have been identified in wave storm frequency. A large inter-annual variability is associated with the results. These findings are valuable to engineers and stakeholders towards alleviating any additional risk posed on the marine sector and coastal activities by climate change.

Data use:

Ref. No.	Product name and type	Documentation
3.5.1	MEDSEA_MUTLIYEAR_WAV_006_012	PUM: https://catalogue.marine.copernicus.eu/documents/PUM/CMEMS-MED-PUM-006-012.pdf QUID: https://catalogue.marine.copernicus.eu/documents/QUID/CMEMS-MED-QUID-006-012.pdf
3.5.2	INSITU_GLO_WAVE_REP_OBSERVATIONS_013_045	PUM: https://marine.copernicus.eu/documents/PUM/CMEMS-INS-PUM-013-045.pdf QUID: http://marine.copernicus.eu/documents/QUID/CMEMS-INS-QUID-013-045.pdf
3.5.3	In-situ observations from moored Italian wave buoys obtained from ISPRA, Italy	URL: http://dati.isprambiente.it/

(Continued)

Continued.

Ref. No.	Product name and type	Documentation
3.5.4	WAVE_GLO_WAV_L3_SWH_NRT_OBSERVATIONS_014_001	PUM: http://marine.copernicus.eu/documents/PUM/CMEMS-WAV-PUM-014-001-002-003.pdf QUID: http://marine.copernicus.eu/documents/QUID/CMEMS-WAV-QUID-014-001.pdf
3.5.5	CERSAT – IFREMER merged along-track altimeter observations	URL: ftp://ftp.ifremer.fr/ifremer/cersat/products/swath/altimeters/waves/documentation

3.5.1. Introduction

The study of extreme wave climate and wave storms is very important and of great relevance to engineering practice. It is crucial for the design and safety control of marine vessels, of offshore and coastal structures (e.g. oil/gas platforms, aquaculture, wind and wave farms), as well as coastal infrastructure (e.g. ports, roads, touristic facilities) (e.g. Gouldby et al. 2014). They are responsible for coastal flooding and affect coastal erosion (e.g. Harley et al. 2017). Climate change results in long-term changes of the extreme wave climate (e.g. Lobeto et al. 2021). Thus, for long-term sustainable planning of marine and coastal activities, the understanding of inter-annual variability and of climatic trends is also very important. Historic and future wave climate changes may require adaptation measures. For example, an increase in the frequency, intensity, and/or duration of wave storm events over a certain region may require enhanced protection from coastal hazards, re-direction of shipping routes or re-enforcement of marine structures (e.g. Bitner-Gregersen et al. 2013; Kirezci et al. 2020). It may increase downtime of operations at sea and it might require advanced systems of alert (e.g. Reeve et al. 2011; Camus et al. 2019; Spinoni et al. 2020).

Several studies have examined the extreme wave climate of the Mediterranean Sea (e.g. Zacharioudaki et al. 2015; Sartini et al. 2017; Morales-Márquez et al. 2020; De Leo et al. 2020) with a number of them focusing on wave storm characteristics (e.g. Zacharioudaki et al. 2015; Besio et al. 2017; Amarouche and Akpinar 2021; Martzikos et al. 2021). The vast majority of these recent studies have relied on wave hindcasts that cover a long time period and have a high resolution. Nevertheless, coarser resolution global studies that use satellite observations (e.g. Young and Ribal 2019) or local studies that use buoy measurements (e.g.

Martzikos et al. 2021) can be found. However, the time frequency of the satellite sampling is considered inadequate for well capturing storm peaks in the highly variable environment of the Mediterranean Sea whereas the spatial sampling of the in-situ observations is not appropriate for studying medium to large-scale wave climate. In addition, data inhomogeneities and gaps are often encountered in observational datasets. As a result, in-situ and satellite observations are mostly used to calibrate and validate the wave models.

In this paper, we study the extreme wave climate of the Mediterranean Sea focusing on wave storm characteristics such as wave storm frequency, intensity and duration. The long-term average statistics, climatic trends and inter-annual variability are examined. The focus is on the spatiotemporal distribution of wave extremes rather than the atmospheric conditions producing them (e.g. Sartini et al. 2017; Morales-Márquez et al. 2020; Amarouche et al. 2021). To this aim, we use a 28-year high resolution wave reanalysis, forced by the ERA5 reanalysis winds, and a peaks over threshold (POT) approach to identify individual wave storm events. It is well known that the quality of a wave hindcast/reanalysis largely depends on the quality of the reanalysis wind forcing fields, which are continually improving. ERA5 is the most recent, publicly available, state-of-the-art global wind reanalysis dataset that has reached a time and space resolution that is adequately high so as to enable a proper assessment of the wave climate extremes in the highly variable environment of the Mediterranean Sea. In addition, the spatial resolution of the wave model, which is the highest used in similar studies involving the full Mediterranean Sea, is able to adequately resolve the fine bathymetric features in the basin caused by the presence of numerous islands, semi-enclosed sub-basins and bays. The assimilation of altimeter SWH, the consideration of wave-current interaction through the input of reanalysis surface currents along with the account of Atlantic swell through nesting to an Atlantic Ocean model are additional characteristics of the wave reanalysis used in this study that are expected to increase the accuracy of the computed extreme wave climate statistics.

3.5.2. Method

The wave reanalysis delivered by the Mediterranean Monitoring and Forecasting Centre (Med-MFC, product 3.5.1) provides hourly instantaneous fields of SWH at 0.041° horizontal resolution covering the Mediterranean Sea and extending up to -18.125°E into the Atlantic Ocean. It is based on the latest

version of the state-of-the-art WAM wave model (WAMDI Group 1988; Komen et al. 1994). It is run in shallow water mode and is extensively tuned for the Mediterranean Sea. It is forced by hourly ERA5 reanalysis winds at about 30 km resolution. It inputs Med-MFC daily averaged surface currents to account for wave-current interaction, it is nested to a coarser resolution (1/6°) Atlantic model to properly account for swell passing in the Mediterranean Sea through the Strait of Gibraltar and assimilates all along-track satellite SWH observations available since 1993 (data are scarce before this year). It is noted that CMEMS has adopted year 1993 as the starting year for its reanalysis products so as to cover the period over which adequate inter-calibrated satellite observations exist for data assimilation.

A detailed description of the system can be found in the Product User Manual (PUM) and Quality Information Document (QUID) available in the CMEMS webpage (see product table). In the latter document, the product is thoroughly validated against in-situ and satellite data, products 3.5.2, 3.5.3 and 3.5.4, 3.5.5 respectively. In this work, a summary of the results is provided. In addition, yearly values of the agreement between collocated reanalysis and observed 99th percentile SWH will be presented for in-situ and satellite data respectively for the period 1993–2018. Observations from 53 wave buoys and 8 satellite altimetry missions have been used to perform the inter-comparisons. All the details of this procedure can be found in the QUID.

Different methodologies exist to isolate wave storms from a time-series of wave data (e.g. Besio et al. 2017; Amarouche and Akpınar 2021). Here, the methodology of Weisse and Günther (2007), modified by Zacharioudaki et al. (2015), is applied. In particular, the pointwise long-term 1993–2020 99th percentile SWH (Figure 3.5.2 (a)) is used as a threshold to determine severe wave conditions, referred to as wave storms. It is noted that there is not a largely accepted method for the selection of the threshold value (Ciavola and Coco 2017; Harley 2017). Values between the 90th and 99th percentile SWH are often encountered in the literature (e.g. Masselink et al. 2014; De Leo et al. 2020). In general, a high threshold is a valid choice when the data sample is sufficiently large and when the focus is on the most extreme events. Having set the threshold, the number of wave storm events is defined as the number of independent events that exceed this threshold. To assure the independency of the events, a spacing of 72 h between them has been adopted (e.g. Debernard and Røed 2008; Meucci et al. 2018). The intensity of each wave storm is defined as the difference between the maximum SWH

that occurred during the storm and the local 99th percentile threshold. Finally, the wave storm duration is the time the storm's SWH remained above the threshold. Based on annual values over the period 1993–2020, maps of average climate statistics and trends of the aforementioned quantities are obtained. Trends are computed using the non-parametric Sen's slope estimator for robust linear regression and are tested for statistical significance using the non-parametric Mann-Kendall test at the 5% significance level (i.e. p -value ≤ 0.05). These estimators are much less sensitive to outliers and skewed distributions compared to simple linear regression methods.

In addition to the long-term pointwise approach, described above, the inter-annual variability of the aforementioned quantities were investigated for a number of Mediterranean sub-regions giving us the possibility to identify sub-trends present within the 28-year period. In this case, the hourly modelled SWH was averaged over pre-defined sub-regions. The resulting regionally averaged time-series was then used to apply the methodology outlined in the previous paragraph.

3.5.3. Results and discussion

Overall, the significant wave height is accurately simulated by the model (QUID, product 3.5.2). Considering the Mediterranean Sea as a whole, the typical difference with in-situ and satellite observations (RMSE) is 0.23 ± 0.012 m (mean of yearly values \pm standard deviation) and 0.24 ± 0.01 m respectively, the BIAS is -0.06 ± 0.022 m and -0.05 ± 0.011 m, the Scatter Index (SI) is 0.27 ± 0.015 and 0.17 ± 0.006 whilst the Correlation Coefficient (R) is 0.95 ± 0.001 and 0.96 ± 0.004

respectively. Spatially, the model performs optimally at offshore wave buoy locations and well-exposed Mediterranean sub-regions. Within enclosed basins and near the coast, unresolved topography by the wind and wave models and fetch limitations cause the wave model performance to deteriorate. To put the above results into context, the model skill of this study is compared to the high resolution study of Amarouche and Akpinar (2021). Specifically, they used a SWAN wave model hindcast (Amarouche et al. 2019) at an horizontal resolution of 0.033° , forced by reanalysis winds at a resolution similar to that of ERA5, to study the storm wave climate and trends in the Western Mediterranean Sea. Their model skill was evaluated against in-situ observations resulting in an average SI of 0.3 and an average R of 0.93 for their full domain. Qualification metrics at individual buoy locations indicate that our reanalysis performs better at all common offshore locations used. In the nearshore, the two studies produce very similar statistics with the study of Amarouche and Akpinar (2021) occasionally having a small advantage over our study. This is attributed to the higher resolution of their wave hindcast that better resolves the coast.

Focusing on the extremes, Figure 3.5.1 shows a very good agreement between reanalysis and first-guess 99th percentile SWH and collocated wave buoy and satellite observations respectively, merged over the Mediterranean Sea. The depicted differences do not exceed 0.3 m with the model mostly underestimating extreme wave heights. A higher model underestimation appears to occur in the period 1993–2000, mostly for the model-buoy comparison.

The 1993–2020 long-term 99th percentile SWH (hereafter referred to as threshold) and the climatic

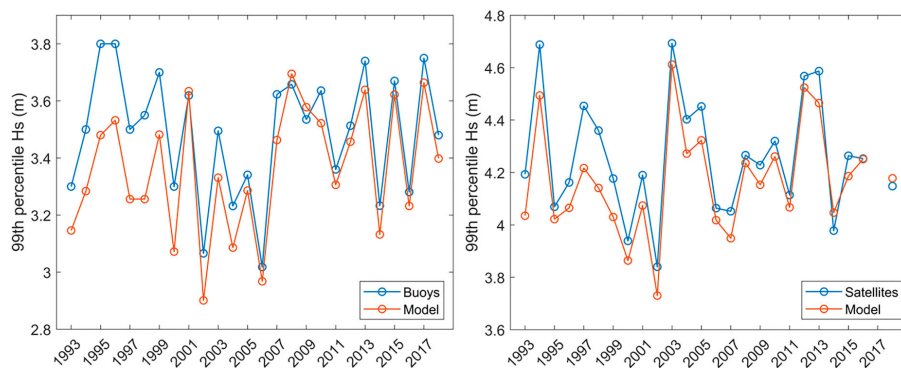


Figure 3.5.1. Yearly values of collocated reanalysis (product 3.5.1) and observed 99th percentile of SWH computed by merging wave buoy (left panel; products 3.5.2, 3.5.3) and satellite (right panel; products 3.5.4, 3.5.5) observations respectively in the Mediterranean Sea.

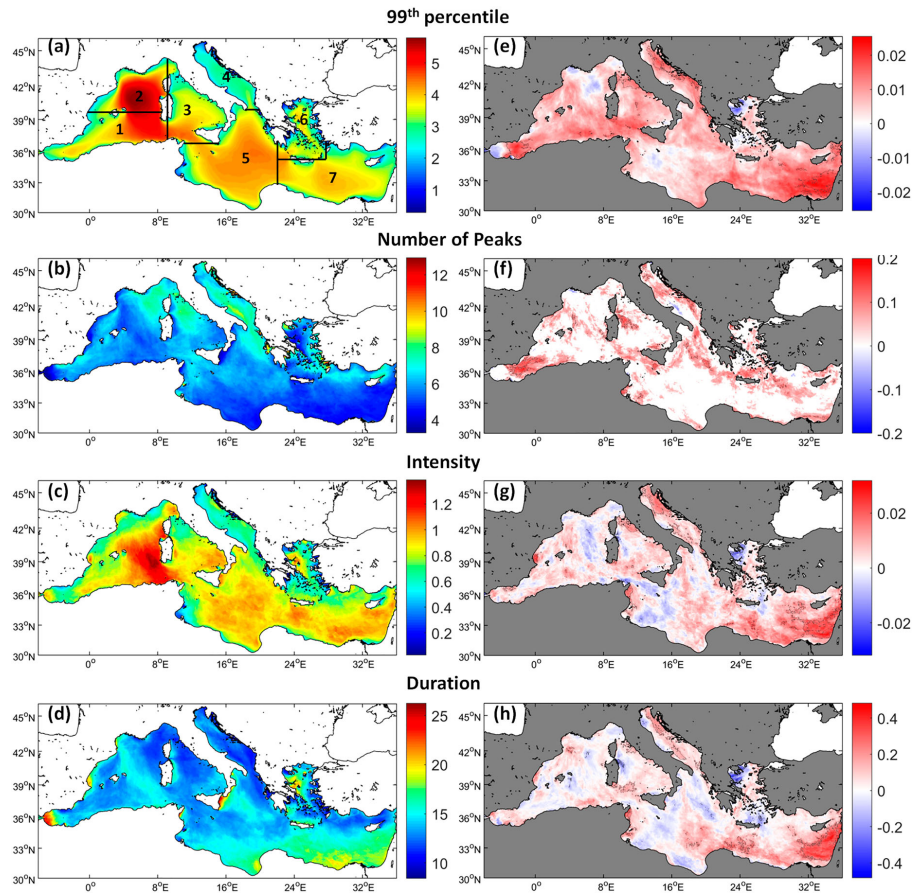


Figure 3.5.2. (a) POT threshold: 1993–2020 long-term 99th percentile of SWH (m) and 1993–2020 average of (b) annual number of events exceeding the 99th percentile, (c) their average intensity (m) and (d) their average duration (hours); (e) 1993–2020 trends of the annual 99th percentile SWH, (f) the annual number of events exceeding the long-term 1993–2020 99th percentile, (g) their average intensity and (h) their average duration. Areas of statistically significant trends at the 5% significance level are within grey contours. The numbers shown in plot (a) denote regions and are used in Figure 3.5.3.

averages of the annual wave storm characteristics are shown in the left panels of Figure 3.5.2. The 99th percentile SWH (Figure 3.5.1(a)) is in alignment with previous studies (e.g. Sartini et al. 2017; Álvarez Fanjul et al. 2019; Morales-Márquez et al. 2020) where the reader may also find information on the atmospheric drivers related to the observed patterns. The average annual number of events exceeding the threshold (Figure 3.5.2(b)) is 4–7 in most of the Mediterranean Sea. The highest number of wave storms (9–13) predominantly occur within regions that are characterised by a mild wave climate. Regions which are characterised by a

stronger extreme wave climate and are additionally affected with a relatively high frequency of wave storms occur west of the island of Corsica (8–9 events) as well as offshore from the Catalan coast, in the Strait of Sicily and northern Ionian Sea (6–8 events). Martzikos et al. (2021) and Amarouche and Akpınar (2021) used lower thresholds and different methods for wave storm analysis and computed values of 10–14 at coastal locations and 10–16 over the western Mediterranean Sea respectively. The average annual wave storm intensities (Figure 3.5.2(c)) have a range of 0.03–1.4 m. In general, high intensities are found over areas of high

thresholds (Figure 3.5.2(a)). An obvious exception is observed seawards from the Gulf of Lion, where the maximum intensities (1.2–1.4 m) are shifted southwards relative to the maximum thresholds, below about 42°N. Enhanced intensities (≈ 1 m) in relation to the threshold are observed in a number of regions including the area east of the Strait of Gibraltar, along the coast of Valencia, Liguria and southern Italy, south of Crete and in the eastern Levantine. The average annual wave storm duration (Figure 3.5.2(d)) has a range of 8–27 h. Most of the aforementioned regions, showing enhanced intensities relative to the threshold, also appear to have high wave storm durations (except Liguria). The results on wave storm intensity and duration fall in line with those in Martzikos et al. (2021) whilst similar durations are stated by Lionello et al. (2006) in relation to Mediterranean cyclones. On the other hand, Zacharioudaki et al. (2015) report higher values of wave storm intensities and durations in the Hellenic Seas which might be because their wave model was found to overestimate wave extremes.

The 1993–2020 trends of the annual values of the 99th percentile SWH are shown in Figure 3.5.2(e). The annual 99th percentile SWH shows widespread positive trends over the period 1993–2020. The trend slope reaches values up to 0.026 m/year with maximum values over the south-eastern Levantine Sea, followed by the eastern Alboran Sea. High values are also found over the south-western Mediterranean Sea between 5° W and 12° W, in the Adriatic Sea, and in other parts of the Levantine. Statistically significant trends (within grey contours in Figure 3.5.2(e–h)) are also found within these regions. These trends are spatially extended in the eastern Alboran Sea, between Corsica and Italy, along the western Adriatic, and over the eastern Levantine basin. Negative trends in the north-west Aegean Sea, around the Strait of Gibraltar, in the eastern part of the Gulf of Lion moving offshore towards the southeast, and in a small part of the western Ionian do not exceed -0.018 m/year and are not statistically significant. Comparison with previous studies revealed the sensitivity of trend estimates on the chosen percentile and on the underlying long-term time-period and/or short-term sub-annual period (e.g. only winters) selected for the analysis. Young and Ribal (2019) also found mostly positive trends at similar rates in the Mediterranean Sea over the period 1985–2018. Also, trend estimates of the winter annual mean SWH (not shown) are in very good agreement with those presented in Timmermans et al. (2020) when using the same period. Nevertheless, Morales-Márquez et al. (2020) found extreme waves trends that are

predominantly negative in the Mediterranean Sea for the period 1979–2009. Similarities and differences are found between our results and those of De Leo et al. (2020) produced for the period 1979–2018. As mentioned in the introduction, this study is mostly interested on the wave climate rather than the forcing wind statistics. Nevertheless, it is worth noticing that an equivalent analysis on the forcing wind speeds (U10) produced 99th percentile U10 trends (not shown) that are in very good alignment with those shown in Figure 3.5.2(e). The agreement is both on the spatial pattern of trend values and on their statistical significance. In the case of U10, maximum positive trends of statistical significance, found in the south-eastern Levantine, the Alboran Sea and the Adriatic Sea, reach values of about 0.05–0.06 m/s/year. Also, the statistically significant positive trends are more spatially extended in the case of U10 in relation to the area covered in the case of SWH.

Figure 3.5.2(f–h) shows the 1993–2020 trends of the wave storm characteristics whose climatic averages were shown in the corresponding left panels of Figure 3.5.2. Regarding the annual number of wave storm events, this is mostly unchanged or has increased within the examined period (Figure 3.5.2(f)). Statistically significant positive slopes are few and largely localised. The most spatially extended region of statistically significant increase is the eastern Alboran Sea, i.e. the area of maximum slope at 0.2 events/year. On the other hand, Cavicchia et al. (2014) and González-Alemán et al. (2019), focusing on Medicanes, found that their frequency is projected to decrease in future climate change scenarios whilst a moderate increase is projected for their intensity. In Figure 3.5.2, wave storm intensity and duration have maximum positive slopes in the eastern Levantine Sea with values of 0.032 m/year (Figure 3.5.2(g)) and 0.482 h/year (Figure 3.5.2(h)) respectively. These are statistically significant. Somewhat smaller but significant rates are also observed in the western part of the Levantine basin. The Adriatic Sea, the area between Corsica and mainland Italy, and the west coast of Tunisia also show statistically significant positive trends. Intensity alone is increasing significantly (≈ 0.03 m/year) along the coast of Valencia while duration does so along the south Tyrrhenian exit. In general, statistically significant positive trends in wave storm characteristics do translate to significant trends in the overall extreme wave climate (Figure 3.5.2(e)). Also, there are regions where all wave storm characteristics do show positive trends, even if not statistically significant, such as the Catalan coast and offshore, over the southern extremity of the Tyrrhenian Sea, a considerable part of the

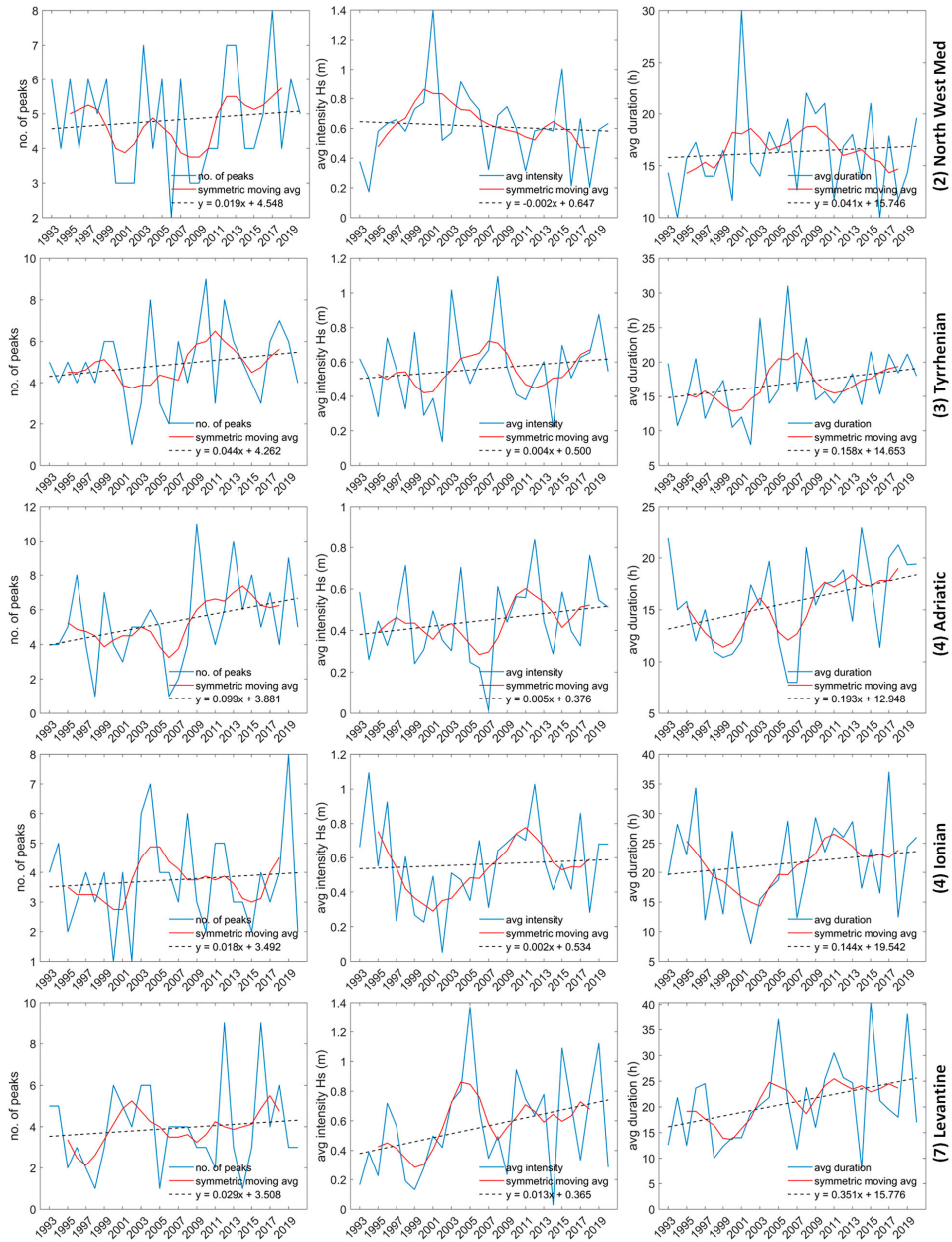


Figure 3.5.3. 1993–2020 inter-annual variability of the annual number of events exceeding the long-term 1993–2020 99th percentile SWH, their average intensity and duration, computed for the sub-regions of the Mediterranean Sea defined in Figure 3.5.2(a) (relevant numbers in Figure 3.5.2(a) are shown in front of the name of the sub-region on the right side of the panels in Figure 3.5.3).

Adriatic Sea, around the western end of Crete island, in the north-east Aegean as well as in parts of the Levantine Sea. Negative trends in intensity and duration reach -0.024 m/year and -0.43 h/year respectively and are not statistically significant. The greatest decrease in wave storm severity is found in the north-east Aegean Sea. Widespread decrease is also seen west of Corsica and Sardinia in the offshore, in the western Ionian Sea and Sicily Strait, and east of the island of Crete. Despite using different methodologies, the wave storm intensity trend directions obtained herein have a lot of similarities with those obtained in Amarouche and Akpınar (2021) for the western Mediterranean Sea for the period 1979–2019; the most apparent discrepancy is found in the Tyrrhenian Sea. Comparing the results in Figure 3.5.2(f–h) to equivalent results obtained for U10 (not shown), a correspondence between U10 and SWH trends is mostly observed, corroborating the causal relationship of wind speed and SWH. In the case of U10, the annual number of storm events shows more widespread positive trends that are statistically significant over more regions compared to those found for SWH. In terms of intensity and duration, a similar spatial pattern of trends is found for the two variables. The Levantine Sea shows the most significant positive trends reaching values of 0.06 m/s/year and 0.3 h/year in U10 storm intensity and duration respectively.

Figure 3.5.3 shows the inter-annual variation of the wave storm characteristics after averaging SWH over the regions defined in Figure 3.5.2(a). The sub-regions generally show large inter-annual variability in wave storm characteristics (also the case for Regions 1, 6, not shown). Strong positive trends in the annual 99th percentile SWH (not shown) are found for the Tyrrhenian and Levantine Seas (p -value ≈ 1) and for the Adriatic (p -value = 0.03). In the Tyrrhenian, an enhanced positive trend in wave storm duration is found whilst in the Levantine both intensity and duration show statistically significant positive trends. In the Adriatic Sea, it is the frequency of occurrence and the duration of the wave storms that show statistically significant increases. For the north west Mediterranean and the Ionian Sea, although the 1993–2020 trend slopes are not statistically significant, statistically significant sub-trends are encountered. In both regions, a turning point occurs around year 2000. Thus, in the former region, a significant positive trend is found in the number of peaks since year 2000 accompanied by a significant decrease in wave storm intensity. In the latter region, significant negative sub-trends are found in the earlier years in wave storm intensity and duration that become significantly positive in the period 1998–2017.

3.5.4. Conclusions

The present study assessed the extreme wave climate of the Mediterranean Sea over the last 28 years, using a high resolution wave reanalysis forced by the ERA5 high resolution global reanalysis. Adopting a Peaks over Threshold approach, the study focused on the characteristics of the most extreme wave storms and on their climatic trends and inter-annual variability.

It was found that the annual 99th percentile SWH, a measure of the overall extreme wave conditions of an area, exhibits an increasing trend almost over the entire Mediterranean Sea. The maximum trend slopes (0.026 m/year), significant at the 5% significance level, occur in the east Levantine Sea and eastern Alboran Sea. In the former basin, the increase could be linked to a statistically significant increase in wave storm intensity (up to 0.032 m/year) and duration (up to 0.48 h/year), also present in other, more localised, areas of the basin. In the latter, it is the wave storm frequency that increased significantly (up to 0.2 events/year) in the last 28 years. The Adriatic Sea also exhibits, spatially extended, statistically significant positive slopes in the 99th percentile SWH, wave storm intensity and duration. The Tyrrhenian Sea, mainly its north and south ends, is also active in terms of significant increases in wave extremes. In general, wave storm frequency exhibited only zero or positive slopes but mostly statistically insignificant. Negative slopes were computed for wave storm intensity and duration but, again, of no statistical significance. Nevertheless, considering the northwest Mediterranean Sea as a whole, statistically significant negative trends in wave storm intensity were computed for the period since year 2000. The same year was also found to be a turning point between negative and positive trends of statistical significance for the wave storminess of the Ionian Sea. Generally, the inter-annual variability of the wave storm characteristics was found to be large.

The estimated changes in the extreme wave regime of the basin are important for the identification of areas that are more vulnerable to hazards linked to climate change and a valuable tool for engineers and stakeholders in terms of sustainable development of maritime activities. For example, it is along the eastern Spanish coast – where a positive slope in all wave storm characteristics is computed in this study and is statistically significant in terms of wave storm intensity at the coast of Valencia – that Storm Gloria, a record breaking storm in terms of SWH, occurred in January of 2020, causing great damage to the coast (Amores et al. 2020; de Alfonso et al. 2021; Alvarez-Fanjul et al., 2022). By extrapolation, there is a higher probability

of occurrence of similar events over regions where a significant increase in wave storminess is estimated over the last 28 years. This, in combination with a broader evaluation of a region in terms of topography, socio-economic activity, sea-level changes etc, can help prescribe a vulnerability index, and, in accordance, the degree and type of intervention in terms of protective measures.

Section 3.6. Surface warming of the Tyrrhenian Sea and local extreme events over the last four decades

Authors: Naomi Krauzig, Enrico Zambianchi, Pierpaolo Falco, Pieter Groenemeijer, Karina von Schuckmann

Statement of main outcome: The Tyrrhenian Sea, one of the most potentially vulnerable sub-basins of the Mediterranean Sea, experienced continuous warming since the early 1980s with increasing occurrences of extreme warm surface conditions during recent years. These conditions enhance the likelihood of ecological impacts with economic consequences, especially during strong marine heatwaves in summer. Our overview provides new insight into seasonal changes and anomalies of the surface warming in the Tyrrhenian Sea, addressing crucial information for aquaculture management and marine conservation efforts. Additionally, this section presents for the first time reported extreme weather events that led to damages, injuries, or fatalities in the highly populated area surrounding the Tyrrhenian Sea. These events are already among the most serious challenges to society in coping with a changing climate. Systematic monitoring of the amplifying socio-economic and environmental impacts is therefore critical for risk assessments and the development of feasible adaptation strategies.

Products used:

Ref. No.	Product name and type	Documentation
3.6.1	SST_MED_SST_L4_REP_OBSERVATIONS_010_021 (Remote sensing) Reprocessed Mediterranean Sea high resolution L4 sea surface temperature	PUM: http://marine.copernicus.eu/documents/PUM/CMEMS-SST-PUM-010-021-022.pdf QUID: http://marine.copernicus.eu/documents/QUID/CMEMS-SST-QUID-010-021-022.pdf Pisano et al. (2016)
3.6.2	SST_MED_SST_L4_NRT_OBSERVATIONS_010_004 (Remote sensing) Near real time Mediterranean	PUM: http://marine.copernicus.eu/documents/PUM/

(Continued)

Continued.

Ref. No.	Product name and type	Documentation
	Sea high and ultra-high resolution L4 sea surface temperature	CMEMS-OSI-PUM-010-004-006-012-013.pdf QUID: http://marine.copernicus.eu/documents/QUID/CMEMS-OSI-QUID-010-004-006-012-013.pdf Buongiorno Nardelli et al. (2013) Data source: https://cds.climate.copernicus.eu/cdsapp#!/dataset/reanalysis-era5-pressure-levels?tab=form Overview: https://cds.climate.copernicus.eu/cdsapp#!/dataset/reanalysis-era5-single-levels?tab=overview
3.6.3	ERA5 (Reanalysis) Hourly atmospheric reanalysis data on single (CAPE, CIN, CP) and on pressure levels (SH)	Data source: https://cds.climate.copernicus.eu/cdsapp#!/dataset/reanalysis-era5-pressure-levels?tab=form Overview: https://cds.climate.copernicus.eu/cdsapp#!/dataset/reanalysis-era5-single-levels?tab=overview
3.6.4	European Severe Weather Database ESWD (Observations) Quality-controlled extreme event data which endanger people and/or lead to significant property damage	Data source: https://eswd.eu/#lookupanchor Overview: https://www.esrl.org/cms/wp-content/uploads/20140509-ESWD_criteria.pdf Dotzek et al. (2009)

3.6.1. Introduction

The Intergovernmental Panel on Climate Change (IPCC) fifth Assessment Report (AR5) of 2014 already affirmed that our climate and its extremes are changing and that associated projected risks will continue to increase as global mean temperature rises (IPCC AR5 2014). The latest IPCC Special Reports concerning the impacts of climate change on land (IPCC SRCL 2019) and on the ocean and cryosphere (IPCC SROCC 2020) emphasise the severity of impacts from extreme events for human systems and ecosystems.

While IPCC AR5 provided evidence that the surface and upper ocean has warmed significantly since 1970 (IPCC AR5 2014), SROCC and the newest Assessment Report (AR6) confirmed that the occurrence of extreme ocean temperatures poses an even higher risk than long-term warming (IPCC SROCC 2020; IPCC AR6 2021). Events of warm temperature anomalies in the ocean prompt substantial disruptions to marine ecosystems and their services (Mills et al. 2013; Rivett et al. 2014; Hobday et al. 2016; Frölicher and Laufkötter 2018;

Smale et al. 2019). Known as marine heatwaves (MHW, Hobday et al. 2016), these extreme events describe abrupt but prolonged periods of high sea surface temperatures (SSTs) that have the potential to extend, or even intensify deeper in the water column (e.g. Schaeffer and Roughan 2017; Bensoussan et al. 2019; Elzahaby and Schaeffer 2019; Darmaraki et al. 2019; see also De Boisseson et al. in Section 3.3) through processes like detrainment and subduction (Holbrook et al. 2020; Elzahaby et al. 2021), the action of downwelling favourable winds (Schaeffer and Roughan, 2107) or possibly by the classically investigated mechanisms of internal wave- and tide- induced mixing (e.g. Wunsch and Ferrari 2004).

MHWs have become more frequent, extensive and intense (Frölicher and Laufkötter 2018; Oliver et al. 2018) with detrimental impacts on organism distributions, ecosystem functions and fisheries productivity with cascading impacts on economies and societies (e.g. Oliver et al. 2018; Darmaraki et al. 2019; IPCC SROCC 2020). Whereas MHWs have received considerable attention in recent years, much less has been documented on their cold equivalent, known as marine cold-spells (MCSs, Schlegel et al. 2017; Feng et al. 2020) that also have the potential to severely impact organisms and ecosystems (Lirman et al. 2011; Szekeres et al. 2016; Wakelin et al. 2021).

As in the ocean, extreme events in the atmosphere such as heatwaves, heavy precipitation and floods, droughts and storms have been shown to affect human societies and ecosystems in a fundamental manner (Parmesan et al. 2000; IPCC AR5 2014; IPCC SRCLL 2019). The latest IPCC reports provide overwhelming evidence that several extreme weather events are already changing under global warming, increasing the risk of pervasive and in some cases irreversible impacts such as loss of life, damages to buildings, agricultural production and natural capital (IPCC SRCLL 2019).

Due to the intensification of extreme atmospheric and oceanic events (Hirabayashi et al. 2013; IPCC AR5 2014; Kundzewicz et al. 2017; IPCC SRCLL 2019; IPCC AR6 2021), relevant studies at global scale have increased significantly in the last few years. However, the impacts on ecosystems and human societies depend primarily on regional trends and the local manifestation of global-scale changes (IPCC SROCC 2020). In addition, science-based information and monitoring at regional and local scales is necessary for sufficient risk assessment and the development of feasible adaptation strategies (Cheng et al. 2021). Thus, in Mediterranean context, it is critical to focus on individual sub-basins, especially those with very high population density

along their surrounding coasts. The target of our investigation, the Tyrrhenian basin, is the most populated semi-enclosed one (UNEP/MAP 2012) and therefore one of the most potentially vulnerable basins in the Mediterranean Sea (Smith et al. 2014). Furthermore, the Tyrrhenian Sea stands out because its response to global warming differs from that of the Mediterranean Sea as a whole (Krauzig et al. 2020) even though it interacts hydrologically and dynamically with the central Mediterranean in the south (Poulain and Zambianchi 2007; Rinaldi et al. 2010) and with the Ligurian Sea in the north (e.g. Astraldi and Gasparini 1994; Marullo et al. 1994; Vignudelli et al. 2000; Pisano et al. 2020). Even though the necessity of local studies has become evident, specific assessments of extreme atmospheric and oceanic events are still missing. To this end, our section provides insights into the prevalence of MHWs and MCSs in the Tyrrhenian Sea and serves as a constructive first step to understand the increasing risks of extreme weather events in the surrounding area.

3.6.2. Methodology

This study takes advantage of the longest freely available high-resolution satellite-derived L4 SST dataset from the Copernicus Marine Environment Monitoring Service (CMEMS product Ref. No. 3.6.1 and 3.6.2), as well as the fifth generation of ECMWF atmospheric reanalysis (ERA5 product Ref. No. 3.6.3) from the Copernicus Climate Change Service Climate Data Store in order to analyse them together with reports of extreme weather events from the European Severe Weather Database (ESWD product Ref. No. 3.6.4) over a period of nearly four decades (1982–2020).

The spatio-temporal variability of the mentioned SST and atmospheric data was studied by analysing the intra- and inter-annual geographical and climatological distributions of averages, anomalies and trends within the geographical boundaries of the Tyrrhenian Sea. If not indicated otherwise, all mentioned time series (daily, monthly, seasonal, yearly) were based on the spatial average of this area over the entire 39-year study period whereas the anomalies were computed against the 1982–2014 core climatology. Hot extremes were defined as the top 10% (90th percentile) of the daily SSTs and cold extremes as the daily SSTs at the bottom 10% (10th percentile).

Accordingly, following Hobday et al. (2016) and Schlegel et al. (2017), MHWs and MCSs were categorised as anomalous warm and cold events that last at least five days, with temperatures exceeding the seasonally varying threshold computed for each day based on the climatological period 1982–2014. Two

events with a temporal gap of less than 2 days were treated as a single joint event. After the events were defined, a set of metrics was calculated including maximum and mean intensity (measured as anomalies relative to the climatological mean, in °C), duration (time from start to end dates, in days), total number of MHW/MCS days, and cumulative intensity (the integrated intensity over the duration of the event, analogous to degree-heating-days; °C days). MCS intensities are calculated as negative values (i.e. anomalies) and are reported in the text as such. When comparing MHW and MCS intensities the absolute values for these metrics were used.

The intra-annual warming was investigated by analysing the SST data over the winter (DJF), spring (MAM), summer (JJA) and autumn (SON) months, while metrics of SST phenology were used to assess changes in the seasonal cycle. More specifically, summer transition and duration metrics for each year were derived from daily SST data based on the first day and the number of days that exceeded the climatological summer mean, respectively. Hereinafter the duration of the warm summer refers to the length of the within-year period with SST higher than the selected threshold.

For the same time span, all available quality-controlled reports of extreme weather events in the area within 0.5 degrees from the coastline of the Tyrrhenian Sea were investigated. The events consist of 9 main types (avalanches, funnel clouds, severe hail, lightning, heavy precipitation and snow, tornadoes, whirlwinds and windstorms) that were associated with private and public damages, registered injuries and fatalities. The data from these reports were used solely as an indication since the number of reported events that lead to significant impacts does not correspond necessarily to exact the occurrence of extreme weather events. In addition, the available information concerning the 10 deadliest events was investigated, while changes in the lower tropospheric moisture content (specific humidity at 700 hPa), convective available potential energy (CAPE) and convective inhibition (CIN) were analysed for the same time span. All trend estimates were based on ordinary least squares linear regression. The corresponding uncertainties were defined by standard errors, whereas the statistical significance (at least 95% level) of the trends was examined through the Mann-Kendall test (Mann 1945; Kendall 1962).

3.6.3. Results

3.6.3.1. Long-term surface warming

The SST of the Tyrrhenian Sea has been rising significantly (95% confidence range) during the period

1982–2020. The long-term SST trend ($0.037 \pm 0.003^\circ\text{C}/\text{year}$) during the last four decades led to a mean cumulative warming of $1.443 \pm 0.117^\circ\text{C}$ over the entire basin. However, the warming is not uniform throughout the different time periods and displays significant spatial dependence (Figure 3.6.1) as the SST in the Tyrrhenian Sea experiences large interannual and long-term variability driven by local and large-scale processes (Krauzig et al. 2020).

The basin-wide averaged temperature change during 2006–2017 was much lower than the long-term trend (Figure 3.6.1(b)). Whereas, during the following years 2018, 2019 and 2020 an unprecedented strong surface warming was reported (the different phases are highlighted in Figure 3.6.2), leading to record values of basin-wide annual mean SSTs of 19.49°C , 19.61°C and 19.71°C , respectively. These record values surpassed even the annual mean SST of 2003 (19.38°C) which had held the title of the warmest year due to the extreme high summer SSTs that occurred during the well-known European heatwave in 2003 (Olita et al. 2007; Hobday et al. 2018).

By analysing further the intra-annual characteristics of the observed surface warming, changes in the seasonal cycle became evident. While the basin-wide SST trends are generally stronger in summer ($0.054 \pm 0.003^\circ\text{C}/\text{year}$), a continuous tendency towards longer warm summer periods was found (see Figure 3.6.2). More specifically, the duration of the warm season has increased from 1982 to 2020 by more than a month (trends in Figure 3.6.2(b)) as the season is starting ~ 21 days earlier and ending ~ 11 days later. These findings are alarming since even smaller changes in the seasonal SST cycle have been shown to influence the behaviour, growth, reproduction and survival of marine species (Edwards and Richardson 2004).

3.6.3.2. Extreme thermal events

The persistence of extreme thermal events in the Tyrrhenian Sea was additionally investigated. MHW events occurred on average at least twice a year, with maximum intensities of 2.44°C that lasted almost 14 days during 1982–2020. The strongest MHW occurred in 2003 and was characterised by an averaged maximum intensity of 5.64°C that lasted the entire summer. The corresponding highest daily SST ever measured occurred on 23rd August 2003 with an exceptional basin-wide temperature of 28.7°C . Whereas their cold equivalent, MCS events, occurred on average once a year with maximum intensities of -2.17°C that persisted ~ 11 days. The most intense individual MCS reached a basin-wide maximum intensity of -4.32°C in 1984. Respectively,

the coldest basin-wide daily SST ever measured occurred on 29th February of 1984 with record low SST of 11.8°C.

Moreover, as assessed in IPCC SROCC and AR6 for the global ocean (IPCC SROCC 2020; IPCC AR6 2021), also the Tyrrhenian Sea showed significant changes in the magnitude and frequency of MHWs and MCSs over the past 4 decades. The results in Figure 3.6.3 reveal an increase in the frequency of MHWs with almost 5 additional events and exceeding anomalies of +0.59°C that last approximately 7 days longer. Moreover, the total number of annual MHW days has been increasing

by almost 2 days each year, leading to a cumulative number of ~74 more extreme warm days whilst more than half (54.25%) of the days with MHWs occurred in the last decade alone.

The frequency of MCSs, on the other hand, has been decreasing over the last 4 decades, leading to 4 fewer annual events which are characterised by less intense cold anomalies (+0.14°C) and approximately 4 days shorter durations. The total number of annual MCS days has been decreasing by more than 1 day each year, leading to a cumulative number of ~51 fewer extreme cold days.

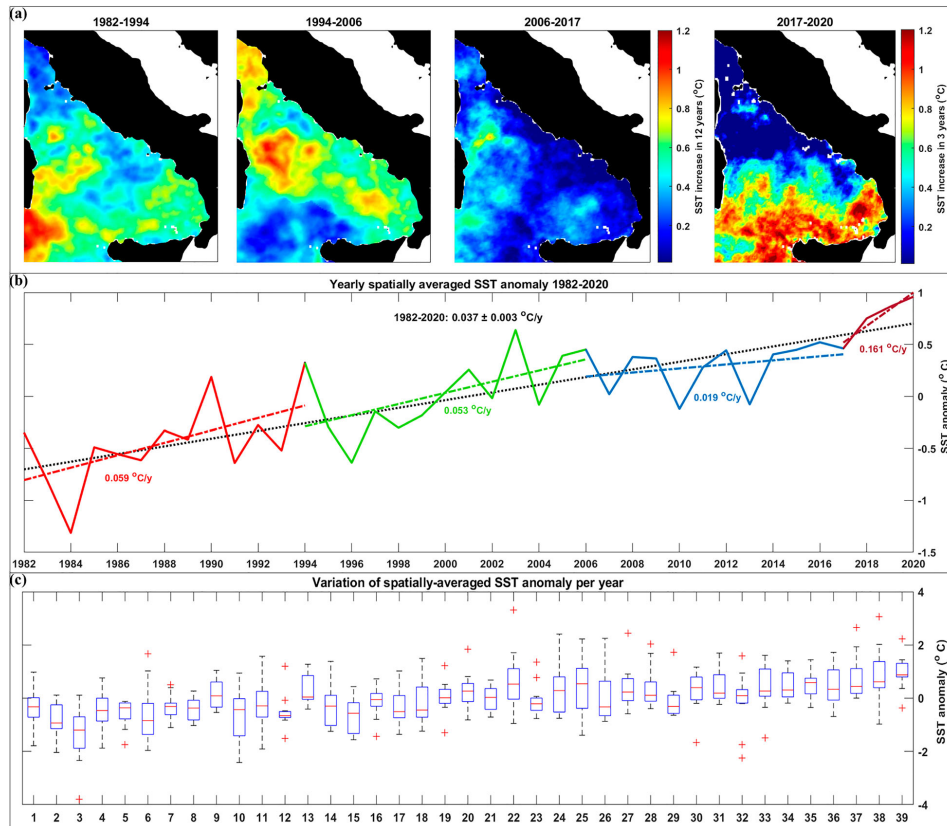


Figure 3.6.1. (a) Spatial distribution of the SST warming during the periods: 1982–1993, 1994–2005, 2006–2017 and 2017–2020. The uneven length of the periods was chosen so as to highlight the different phases in the change. Note the temporal difference in the colourbar. (b) Yearly values of the spatially averaged SST anomaly with trends (at 95% confidence level) per individual period (coloured lines) and for the whole-time span (black dotted line). (c) Boxplot representing the SST anomaly variation for each year: on each box, the central mark indicates the median, and the bottom and top edges of the box indicate the 25th and 75th percentiles, respectively. The whiskers extend to the most extreme data points not considered outliers, and the outliers are plotted individually using the '+' symbol. All graphical representations are based on the satellite-derived SST CMEMS products (Ref. No. 3.6.1 and 3.6.2).

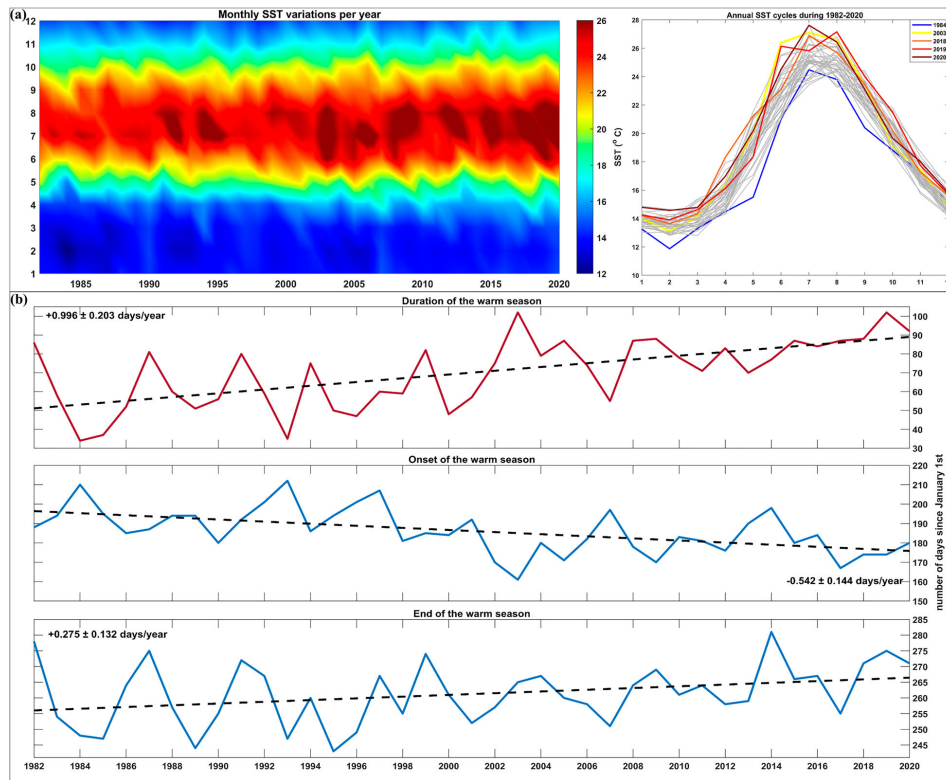


Figure 3.6.2. (a) Hovmöller diagram (left) and intra-annual variations (right) of the spatially averaged SST per year, indicating significant changes in the seasonal cycle during 1982–2020. The monthly SST variations of the coldest year (1984), the three warmest years (2018, 2019, 2020) and the year of the European heatwave (2003) are highlighted for comparison with blue, shades of red and yellow, respectively. (b) SST phenology changes over the study area for the 39-year study period, showing the trend (at 95% confidence level) of the summer days (top), the summer onset (middle) and the trend of the summer end (bottom) based on the satellite-derived SST CMEMS product (Ref. No. 3.6.1 and 3.6.2).

3.6.3.3. Extreme weather events

As in the ocean, extreme events in the atmosphere are also expected to have changed during the last decades with significant effects on human societies and ecosystems (IPCC SRCCCL 2019; IPCC AR6 2021). In the coastal area surrounding the Tyrrhenian Sea, 5445 extreme weather events have been reported in the last 39 years. The events consist of 9 main types (Figure 3.6.4) that were associated with numerous private and public damages, 541 registered injuries and 249 fatalities (based on the analysis of ESWD Ref. No. 3.6.4).

Using these reports as an indication of severe socio-economic impacts, it seems that the most catastrophic event type was heavy precipitation as it caused most (67%) of the registered fatalities (Figure 3.6.4(d,e))

and frequently represented the main cause of severe damages. Reports of these extreme precipitation events and the resulting flash floods have shown an amplification of their frequency as well as of their severity, which can be attributed to the fact that more events were reported over time. In addition, 9 out of the top 10 deadliest events occurred in the last 12 years and were all caused by heavy precipitation.

3.6.4. Discussion and conclusions

Human communities in close connection with the ocean environment are particularly exposed to the occurring changes in the ocean and more than ever a long term, comprehensive and systematic monitoring, assessment and reporting of the ocean are required to

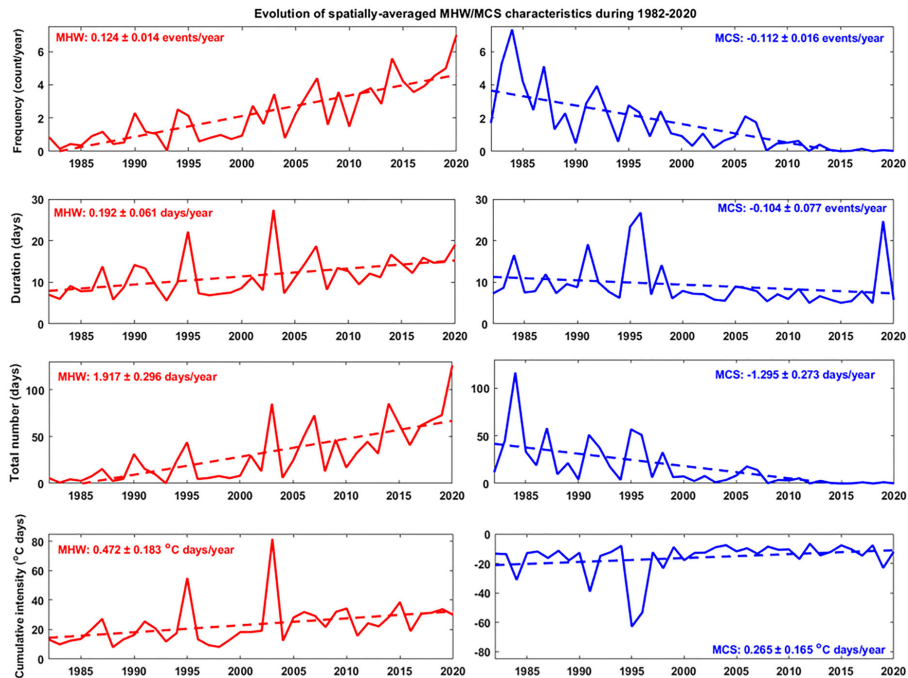


Figure 3.6.3. Time series of the annual basin-wide-averaged MHW (red) and MCS (blue) metrics together with their linear trends for the whole-time span (dotted line). These metrics were calculated following Hobday et al. (2016) and Schlegel et al. (2017) based on the daily satellite-derived SST CMEMS products (Ref. No. 3.6.1 and 3.6.2). Mean values are in units of annual event count (frequency), days (duration and total number of days with anomalous temperatures) and °C days for the integrated temperature anomaly during the event, equivalent to the sum of all daily intensity values (cumulative intensity). Trends (at 95% confidence level) are in the same units as the mean, per year.

ensure a sustainable science-based management for societal benefit (IPCC SROCC 2020).

Taking advantage of the longest freely available high-resolution satellite-derived SST dataset from the Copernicus Marine Environment Monitoring Service, we have shown that the surface temperatures in the Tyrrhenian Sea have been rising over the last 39 years with an average rate of 0.037°C/y which led to an accumulated warming of more than 1.44°C throughout the entire basin. The strong warming trend agrees with recent estimates concerning the Western Mediterranean Sea (0.036°C/y) during the period 1982–2018 (Pisano et al. 2020). The significant difference in the temporal SST variability of the two regions however (Krauzig et al. 2020), underlines the importance of local studies on sub-basin scales.

The long-term warming of the Tyrrhenian Sea was dominated by high increases of SST during the warm seasons, leading to significantly earlier and longer warm summer periods with an average extension of

roughly 1 day every year. Given that the seasonal cycle accounts for the majority of the total SST variance, a lengthening of the warm summer season by more than a month is expected to have profound climatological and socio-ecological impacts (Kushnir et al. 2002; Keeling et al. 2010; Liu et al. 2020).

Additionally, as surface temperatures have been rising significantly during the last four decades, cold spells have become rarer and less severe, while marine heatwaves have become more severe, prolonged, and frequent. Even though changes in MHW/MCS frequency, intensity and duration are not simply a result of increasing mean SSTs (see also the discussion in section 1.7 by Dayan et al.), the projected SST warming under current greenhouse gas emission levels is expected to have a strong effect on MHW events (Collins et al. 2019; Oliver 2019).

Wakelin et al. (2021) pointed out, that the impact of MHWs on marine ecosystems depends on the duration and amplitude of each event compared with the

timescales of the ecological response and the susceptibility of the various components of the ecosystem. While some species might be able to gradually acclimatise to increasing temperatures in the presence of a long-term warming trend, species that are already living in the warmer end of their thermal preference spectrum

are likely to exceed critical temperature thresholds during MHW events (e.g. Marba and Duarte 2010). Furthermore, as warming trends favour a more stratified upper ocean (Li et al. 2020), impacts from accumulated heat stress and stratification are expected to surpass the coping capability of pelagic marine ecosystems and

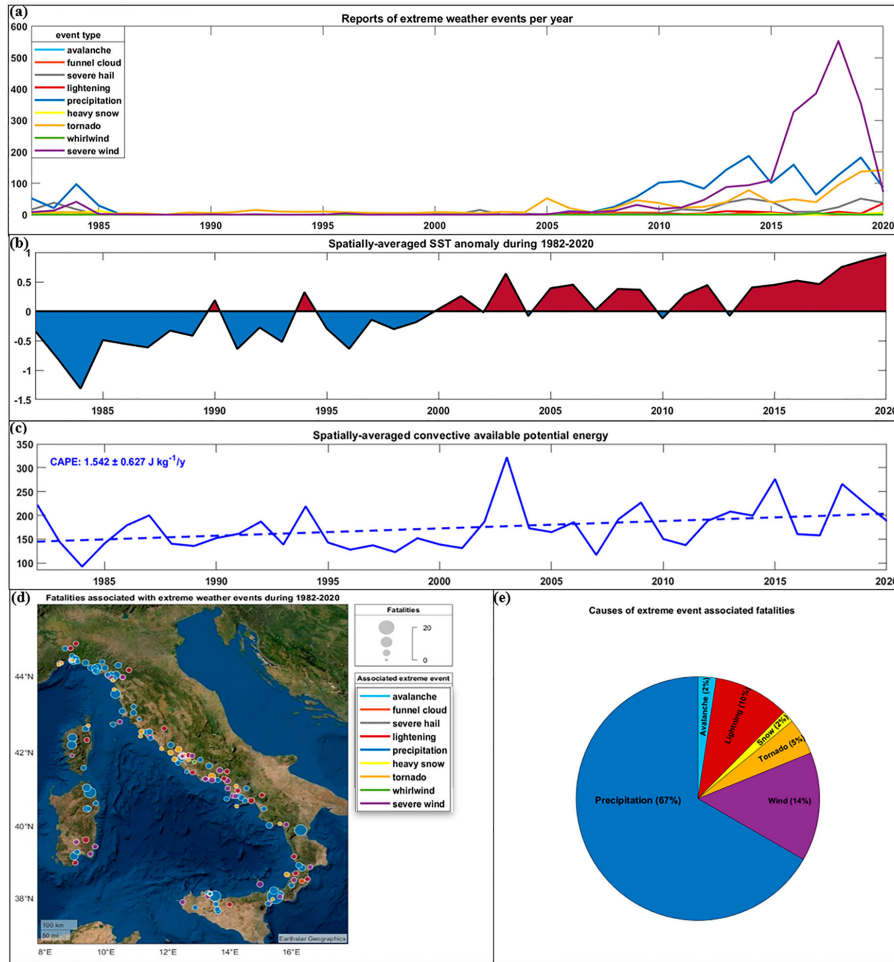


Figure 3.6.4. (a) Reported occurrences of extreme weather events (ESWD Ref. No. 3.6.4) in the coastal area (up to 0.5 degrees from the coastline) of the Tyrrhenian Sea. (b) Yearly values of the spatially averaged SST anomaly (CMEMS Ref. No. 3.6.1 and 3.6.2) indicating negative and positive anomalies with blue and red colours, respectively. (c) Yearly values of the spatially averaged convective available potential energy (CAPE) indicating the evolution of the mean atmospheric instability that can be used to assess the potential for the development of convection leading to severe weather events (ERA 5 Ref. No. 3.6.3). (d) Spatial distribution of the ESWD severe weather events associated with fatalities during the last 4 decades. Each circle represents the geographic location of an extreme event that caused fatalities, while the size indicates the severity (number of fatalities) and the colour the specific type of the event (ESWD Ref. No. 3.6.4). (e) Percentage of each extreme weather type that caused fatalities across the selected area during 1982–2020 based on reports from the European Severe Weather Database (ESWD Ref. No. 3.6.4).

primary production (Cavole et al. 2016; Jacox et al. 2016; Smale et al. 2019).

At the same time, increasing numbers of extreme weather events with catastrophic impacts have been reported in the highly populated area surrounding the Tyrrhenian Sea. According to the latest IPCC reports (IPCC SROCC 2020; IPCC AR6 2021), confidence has increased that some extremes will become even more frequent, widespread and intense during the twenty-first century at global scale. These events are among the most serious challenges to society in coping with a changing climate. In the Tyrrhenian Sea, the amplification of magnitude and frequency of reported extreme weather events led to significantly more damages, injuries and fatalities throughout the last 4 decades. Especially the increasing extreme precipitation events and the resulting flash floods have had catastrophic socio-economic impacts, costing at least 166 people their lives and leaving severe damages behind. Whilst flash floods are already considered the most frequent and among the costliest and deadliest natural disasters worldwide (Munich RE, NatCat Service; Swiss RE, 2015) the corresponding extreme precipitation events are expected to almost double per degree of further global warming (Myhre et al. 2019).

Several studies (Trenberth et al. 2015; Volosciuk et al. 2016; Dittus et al. 2018; Pastor et al. 2018) have shown that extreme precipitation events can be influenced by high SST through the recharge of moisture and heat and its contribution to increased conditional convective instability (i.e. Pastor et al. 2001; Lebeaupin et al. 2006; Alexander et al. 2009; Rebora et al. 2013; Messmer et al. 2017). Indeed, the overall trends in lower tropospheric moisture content (Specific humidity at 700 hPa: $+6.16 \pm 1.49 \times 10^{-6} \text{ kg kg}^{-1}/\text{y}$) and convective available potential energy (CAPE: $+1.54 \pm 0.63 \text{ J kg}^{-1}/\text{y}$, Figure 3.6.4 (d)) could be a first indication that changes in thermodynamic instability and factors leading to convective initiation (following Taszarek et al. 2021) have become more favourable for heavy precipitation events. Further research into the potential role of SST changes in the occurrence of extreme precipitation events is therefore a promising avenue.

Our study provides insights into the prevalence of anomalous thermal events in the Tyrrhenian Sea and serves as a constructive first step to understand the risks of extreme weather events in the surrounding area. In the framework of climate change, these extremes and their nature need to be periodically monitored and analysed for future scenario projections that could help stakeholders in the establishment of mitigation and adaptation policies.

Section 3.7. Winter nutrient content as a basic proxy of ocean fertility

Authors: Donata Melaku Canu, Ginevra Rosati, Gianpiero Cossarini, Célia Laurent, Giorgio Bolzon, Cosimo Solidoro

Statement of main outcome: The capability of the oceans to sustain a productive and healthy ecosystem is one of the most important ecosystem services provided by the sea. Indeed, society is increasingly asking for indicators able to capture and deliver quantitative information on the spatial and year-to-year variability of these important ocean properties, also in order to support the implementation of sustainable approaches to marine spatial planning and to exploitation of biotic ocean resources.

Here we propose to compute ecosystem indicators related to trophic status and ocean fertility, derived from combinations of nutrient availability, primary productivity, chlorophyll, and fish landings. In particular, the abundance of nutrients in surface layers just after the winter mixing determines how fertile a region can be in the following spring and summer, since primary productivity relies on nutrient assimilation from the photic layer.

Several indices can be used to assess the trophic level of a water body and as a proxy of ocean fertility, from total chlorophyll concentration to multivariate indices such as TRIX and data on fish landings. Here we compute some of those indices and test whether or not they can be predicted in advance, as a function of the winter conditions described by CMEMS products.

Our results highlight that for most of the Mediterranean sub-basin the winter surface nutrient content, defined as the integral of nutrient concentration between the surface and the typical pycnocline depth of the sub-basin, can be used to predict months in advance the total amount of phytoplankton biomass to be developed in the following warm seasons, and in some cases provide some indications also on fish landings. This measure can therefore be considered as a first order index, and a predictor, of ocean fertility.

Products used in the analysis and documentation links:

Ref no.	Data name	Documentation	Type of product
3.7.1.	MEDSEA_MULTIYEAR_BIO_006_008	PUM: http://marine.copernicus.eu/documents/PUM/CMEMS-MED-PUM-006-008.pdf	Model data

(Continued)

Continued.

Ref no.	Data name	Documentation	Type of product
3.7.2	MEDSEA_MULTIYEAR_PHY_006_004	<p>QUID: http://marine.copernicus.eu/documents/QUID/CMEMS-MED-QUID-006-008.pdf</p> <p>PUM: https://catalogue.marine.copernicus.eu/documents/PUM/CMEMS-MED-PUM-006-004.pdf</p> <p>QUID: https://catalogue.marine.copernicus.eu/documents/QUID/CMEMS-MED-QUID-006-004.pdf</p>	Model data
3.7.3	Fishery Statistical Collections Global Production	http://www.fao.org/fishery/statistics/global-production/en	In-situ

3.7.1. Introduction

In mid-latitude seas, often the plankton blooms start at the end of winter, as soon as light and temperature are suitable for photosynthesis and proceed as long as the inorganic nutrient dissolved in the upper part of the water column -originally homogenous because of winter mixing- is depleted. Indeed, the surface warming brought by the incoming spring creates a stratification which prevents - or strongly reduces- the vertical supply of nutrients from below the pycnocline up to the surface layers. At the same time, the stratification keeps the planktonic organisms in the upper part of the water column and if the critical depth (sensu Sverdrup, see Sverdrup 1953) is deeper than the pycnocline, the bloom develops as a subsurface spring bloom and lasts until the concentration of the most limiting nutrient in the upper part of the water column is close to zero. Meantime, part of the phytoplankton biomass is grazed by zooplankton and channelled along the food webs up to fishes (Mann and Lazier 2006; Libralato and Solidoro 2009). Therefore one might consider that, every year, all the nutrient in the upper part of the water column is later on assimilated by autotrophic organisms, and that the total amount of plankton biomass grown in a year is somehow constrained by the availability of nutrient in winter, computed as the sum of nutrients from

the surface to the depth of the pycnocline (that will develop in the spring). Note that -as long as surface nutrient concentration during summer is close to zero- the surface concentration of winter can also be seen as the amount of nutrient brought to the surface during the cold season, and therefore as a winter nutrient fertilization index.

Here we tested this hypothesis by checking of the existence of a significant correlation between such a winter surface nutrient index, hereafter labelled 'wsnc' and the total amount of phytoplankton developed in spring and summer, by analysing the time series of those variables provided by 21 years long reanalysis of biogeochemical properties in the Mediterranean Sea, MEDSEA_MULTIYEAR_BGC_006_008, for each of 8 Mediterranean sub-basins (Cossarini et al. 2021).

We also test the possibilities of predicting yearly fish biomass estimates provided by FAO (www.fao.org/fishery/statistics/global-production/en), as a function of winter environmental variables, again for different Mediterranean sub-basins.

Other approaches can be used to explore the relationships between environmental properties and sea productivities (e.g. Rose et al. 2010; Béjaoui et al. 2018; Peck et al. 2018). Here we chose to focus our analysis only on the existence of the above-mentioned correlations, in order to test if, and to what extent, simple and easy to compute indices (such as *wsnc*) can capture and provide useful and important information on ocean productivity.

3.7.2. Methods

We based our analysis on the CMEMS reanalysis of biogeochemical and physical variables in the Mediterranean Sea (Data Ref #: 3.7.1, 3.7.2). Starting from the monthly mean profiles, we computed monthly values of integrated chlorophyll and integrated nutrients over the upper layers (from surface to a cut-off depth) from 1999 to 2019 (21 years providing 252 data points for each variable) and for each of the 8 Mediterranean sub-basins normally considered in CMEMS, i.e. Alboran Sea (ALB) the South Western Mediterranean (SWM), the North Western Mediterranean (NWM), the Tyrrhenian Sea (TYR), the Adriatic Sea (ADR), the Aegean Sea (AEG), the Ionian Sea (ION), the Levantine Sea (LEV). The cut-off depths for the integration of variables were evaluated by inspecting the time evolution of chlorophyll profiles and identifying the depth above which the time variability of chlorophyll concentration became very low, and much lower than above. In this way, we set the cut-off depth to 150 m in the

Western Mediterranean Sea and to 200 m in the Eastern Mediterranean Sea, with the exception of the Adriatic Sea, where biogeochemical dynamics are mostly occurring in the top 100 m. The spatially integrated monthly values were then aggregated to derive seasonal values.

As an example, the winter surface nutrient index, *wsnc*, is defined as

$$wsnc = \sum_{i=\text{jan}}^{\text{march}} \sum_{j=1}^{zc} nuti_{i,j} \quad (3.7.1)$$

where *zc* is the cut-off depth introduced above, and *nuti_{i,j}* is the concentration of the nutrient limiting phytoplankton growth at depth *j*.

A correlation matrix has then been computed among all couples of integrated variables, and simple and multiple linear regression models developed for synthesising annual biogeochemical variability.

The data set was then integrated with FAO fishery landings data from 1999 to 2018 (Data Ref #: 3.7.3) available for subbasins NWM, TYR, ION, LEV, ADR, and AEG, and used to investigate relationships between winter nutrient fertilization, plankton dynamics and fish landings, through the use of multiple linear regression models.

Finally, the climatology of *wsnc* is produced, in order to highlight standard reference behaviour and year-to-year variability.

3.7.3. Results

The correlation plots for the Mediterranean sub-basins show parameter distribution and correlation for each variable pair. Figure 3.7.1 depicts the plot for one of the sub-basins (ION) as an example. Table 3.7.1 provides a summary of the results. The analysis shows that phytoplankton biomasses and chlorophyll concentrations were significantly correlated to PO₄ and NO_x concentrations in most cases (Table 3.7.1), except the ALB subbasin where no relation was found, likely because of the strong influence of the Gibraltar Strait. For the SWM and TYR the correlations coefficients for phytoplankton biomasses are about 0.4, but in the SWM the correlation is significant only for PO₄ and not for NO_x. In the NWM, AEG, ION and LEV coefficients are higher and significant. The correlations coefficients for chlorophyll tend to be lower than those for biomasses, except for the Adriatic Sea where chlorophyll seems to be better predicted. We note that while chlorophyll is frequently used as an indicator of productivity, chlorophyll is only a proxy of plankton biomass, which remains a much more direct and meaningful indicator of plankton productivity. Indeed, the Carbon to Chlorophyll ratio in plankton can vary quite a lot, as a

function of nutrient limitation, light, and cell state (Geider et al. 1998; Lazzari et al. 2012).

As for biomass, factors others than nutrients can contribute to defining plankton dynamics, including irradiance and water transparency, vertical diffusion, the sinking rate of planktonic cells, and grazing pressure (Jamar et al. 1977; Mann and Lazier 2006), so that it is not surprising to see that different regions present different correlations between nutrients and plankton biomass. In particular, the correlation can decrease whenever horizontal processes become as significant as vertical processes, as well as in spatially highly heterogenous regions, where a single spatially averaged value cannot provide a sufficiently detailed picture of the system. The relationships between nutrients and fish abundance is even more complex, since different species of fish feed on different preys and have different trophic levels and therefore some species are more loosely related to plankton biomass than others. Furthermore, in this study we used the FAO landings data, that are fishery dependent observations bound to overestimate commercially valuable species relative to others.

The analysis of correlations including fish landing data, where available, shows weak or no linear correlation, in most sub-basins (Table 3.7.1).

Taking into account more than one predictor, the results of the multiple regressions indicate that in the eastern part of the Mediterranean, EMED (sum of LEV, AEG, ADR, ION subbasins), 65% of the variation of summer chlorophyll and 69% of the variation of summer phytoplankton biomasses can be explained taking into account winter nutrients, salinity and/or temperature, while in the western Mediterranean, WMED, the variability explained amounts to 85% for chlorophyll and 90% for biomasses.

The resulting regression equations are given in Table 3.7.2, together with the best models for fish landing data. Multiple regression analyses have the capability to significantly predict fish landings when past dynamics are included. In particular, we found that a model (model M1, Equation 3.7.2) taking into account the landing of the previous year and the summer temperature of the current year is a good predictor for NWM, TYR, AEG, ION and LEV (Table 3.7.2). However, in NWM, TYR, and LEV, the relation with temperature is not significant, and thus the equation is reduced to a simple linear model (Table 3.7.2).

For the ADR sub-basin, a more complex model (M2, Equation 3.7.3) has to be used, taking into account winter temperature and the zooplankton biomass observed two years in advance, but no landings of previous years. This regression model is also a better predictor than the previous one in the LEV subbasin, but in this case the catches of the previous year remain relevant and winter

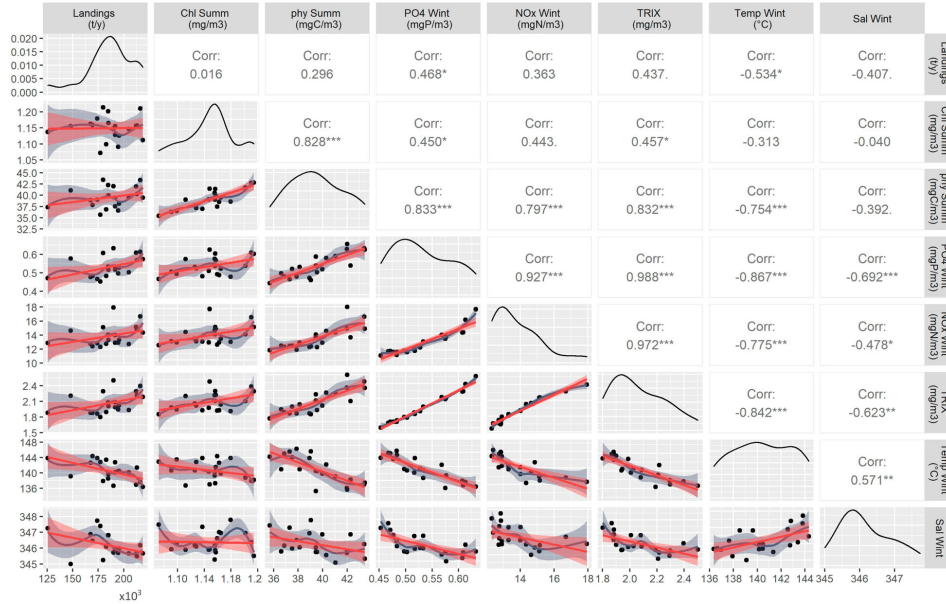


Figure 3.7.1. Correlation plot for the biogeochemical dynamics in the Ionian Sea. ‘Summ’ is computed as the sum of June, July and August concentrations, while ‘Wint’ is the sum of January, February and March values. Chl is for chlorophyll (mg/m3), phy is for phytoplankton carbon biomasses (mgC/m3), PO4 is for phosphate (mgP/m3), NOx is for nitrate and nitrite (mgN/m3), TRIX is a trophic index calculated as $TRIX = \frac{1}{1.2}(\log NOx + \log PO4 + \log Chl + 1.5)$ (Vollenweider et al. 1988), Temp is water temperature and Sal is salinity. Significance levels: **** = 0, *** < 0.001, ** < 0.01, * < 0.05, ' ' n.s.

temperature is not important. If those models are combined, temperature becomes less significant.

$$M1 \quad FishL_y = f(FishL_{y-1}, Temp_{sum}) \quad (3.7.2)$$

$$M2 \quad FishL_y = f(FishL_{y-1}, Zoo_{y-2}, Temp_{win}) \quad (3.7.3)$$

Other significant correlations used as predictors the winter surface nutrient concentrations observed two years in advance, possibly suggesting that fish dynamics depend on biogeochemical properties over longer time

intervals, as well as the TRIX index (Vollenweider et al. 1998) of the previous summer, again stressing the relevance of taking into consideration the importance of the trophic level over time scales longer than a year, and possibly related to the lifespan of fish. In all of these models, however, the contribution of nutrient (or TRIX) predictors is lower than the contribution of previous year catches. These results offer further support to the conclusion that fish population dynamics is affected by environmental conditions through the

Table 3.7.1. Synthesis of the correlation coefficients between winter nutrient concentrations and summer phytoplankton biomasses and chlorophyll concentrations, and fish landings for Mediterranean Sea sub-basins. Grey numbers indicate non-significant correlations.

Winter nut	Mediterranean sub-basins							
	ALB	SWM	NWM	TYR	ADR	AEG	ION	LEV
<i>Phytoplankton biomasses</i>								
PO4	<0	0.40 [#]	0.69***	0.41 [#]	-0.63**	0.75***	0.84***	0.55*
NOx	~0	0.29	0.68**	0.44*	-0.55*	0.82***	0.80***	0.58**
<i>Chlorophyll</i>								
PO4	~0	0.36	0.47*	-0.45	0.48*	0.56*	0.45*	0.17
NOx	~0	0.22	0.45*	-0.20	0.30	0.68**	0.44 [#]	0.29
<i>Fish</i>								
PO4	nd	nd	0.41 [#]	0.37	0.41*	0.31	0.47*	~0
NOx	nd	Nd	0.40 [#]	0.32	0.18	0.29	0.36	~0

Notes: Significance levels: **** = 0, *** < 0.001, ** < 0.01, * < 0.05, ' ' n.s.

Table 3.7.2. Significant regressions for Mediterranean Sea sub-basins from the multiple regression analysis carried out with Chlorophyll, Phytoplankton biomass, landings data and CMEMS biogeochemical variables.

		Multiple regression models
WMED	Chlorophyll	$Chl_{sum} = 4.29 + 0.62 PO_{4\ win} - 0.024 NO_{x\ win} - 0.031 Sal_{win} - 0.006 Temp_{win}$
EMD		$Chl_{sum} = -1.1038 + 1.5407 PO_{4\ win} - 0.0367 NO_{x\ win} + 0.0110 Sal_{win} + 0.0045 Temp_{win}$
WMED	Phytoplankton biomass	$PhyC_{sum} = 213 + 40.4 PO_{4\ win} - 1.03 NO_{x\ win} - 1.54 Sal_{win} + 0.48 Temp_{win}$
EMED		$PhyC_{sum} = 20 + 60.8 PO_{4\ win} - 0.97 NO_{x\ win} - 0.09 Sal_{win} + 0.04 Temp_{win}$
NWM	Fish landings: example of significant model	$FishL(y) = 9.281 \cdot 10^5 + 8.939 \cdot 10^{-1} FishL(y-1)$
TYR		$FishL(y) = 3.204 \cdot 10^4 + 5.8 \cdot 10^{-1} FishL(y-1)$
AEG		$FishL(y) = 4.203 \cdot 10^5 + 4.867 \cdot 10^{-1} FishL(y-1) - 7.042 \cdot 10^3 Temp_S(y)$
ION		$FishL(y) = 1.117 \cdot 10^6 + 3.511 \cdot 10^{-1} FishL(y-1) - 6.168 \cdot 10^3 Temp_S(y)$
ADR		$FishL(y) = 5.878 \cdot 10^4 + 2.176 \cdot 10^3 Temp_W(y) - 1.307 \cdot 10^3 ZooC(y-2)$
LEV		$FishL(y) = -8.17 \cdot 10^4 + 8.564 \cdot 10^{-1} FishL(y-1) + 1.1018 \cdot 10^3 ZooC(y-2)$

year	adr	aeg	ion	lev	nwm	swm	tyr
1999	0.05	-0.09	0.25	-0.03	0.20	0.15	0.22
2000	0.04	-0.02	0.18	0.07	0.19	0.12	0.10
2001	0.03	-0.01	0.05	0.07	0.06	0.05	0.01
2002	0.10	0.03	0.02	0.03	0.01	0.06	0.03
2003	0.10	0.11	0.07	0.04	-0.02	0.05	0.04
2004	0.11	0.11	0.09	0.05	-0.03	0.06	0.04
2005	0.04	0.05	0.08	0.04	0.20	0.08	0.09
2006	-0.03	0.08	0.02	0.08	0.18	0.13	0.02
2007	-0.07	0.08	-0.03	0.06	0.00	0.13	0.05
2008	-0.05	0.04	-0.05	0.02	-0.06	0.00	0.03
2009	0.03	0.01	-0.07	0.00	-0.01	-0.04	0.02
2010	0.04	-0.04	-0.05	-0.07	0.06	-0.06	0.01
2011	-0.07	-0.08	-0.05	-0.07	-0.02	-0.03	-0.03
2012	-0.07	0.00	-0.01	0.00	-0.04	-0.07	-0.05
2013	-0.03	-0.03	-0.06	-0.02	0.04	-0.04	-0.06
2014	-0.06	-0.05	-0.10	-0.04	-0.10	-0.06	-0.07
2015	-0.13	-0.02	-0.06	-0.06	-0.11	-0.11	-0.04
2016	-0.08	-0.11	-0.06	-0.09	-0.14	-0.11	-0.09
2017	0.00	-0.03	-0.09	-0.03	-0.20	-0.12	-0.12
2018	0.05	-0.03	-0.10	-0.03	-0.06	-0.06	-0.11
2019	0.01	0.01	-0.03	0.00	-0.14	-0.10	-0.10

Figure 3.7.2. Annual variability of winter surface contents in the different Mediterranean sub-basins, relative to each sub-basin climatological value.

superposition of different processes, including nutrient availability and temperature, but the relationships among these variables are complex and possibly mediated by intermediate variables, such as zooplankton biomass.

$$M3 \quad FishL_y = f(FishL_{y-1}, NO_{x\ win-2}, Temp_{sum}) \tag{3.7.4}$$

$$M4 \quad FishL_y = f(FishL_{y-1}, Trix_{y-1}, Temp_{win}) \tag{3.7.5}$$

Finally, **Figure 3.7.2** provides the evolution of the anomaly of such indices for each of the basins over 1999–2019 highlighting the prevalence of positive anomaly in the first years of this period and negative anomalies in the last decade.

3.7.4. Conclusion

For most of the Mediterranean sub-basins, the winter surface nutrient content index, defined as the integral

of nutrient concentration between the surface and the typical euphotic depth of a sub-basin and over winter months (see Equation (3.7.1)), is significantly correlated to the plankton productivity, captured by the total summer chlorophyll concentration or, even better, by the total phytoplankton biomass. In some cases, fish biomass landing can also be predicted. Therefore, this index can be seen as a basic predictor able to provide indications on the productivity expected in the upcoming spring and summer seasons. The capability to predict chlorophyll and phytoplankton biomass increases when using multiple regression models (i.e. more than one predictor) using both nitrogen and phosphorus but also temperature and salinity values. The use of multiple regression models, however, does not increase the capability of predicting fish landings, unless fish past abundance is considered, in some cases also in conjunction with the winter nutrient concentration of 2 years before. These facts, while confirming that the dynamic underpinning the relationship between fishes and nutrient mixing is more complex than the one between nutrients mixing and plankton, also confirm that such a relationship exists, and that indices based on winter properties can also be informative for sea productivity at the fish level. However, more complex relationships should be considered, and possibly spanning longer time windows. The use of the simpler winter surface nutrient content index therefore appears appropriate as a first order index, and predictor, of ocean fertility.

Notes

1. <https://geoblueplanet.org/>.
2. <http://macbio-pacific.info/Resources/fiji-interactive-atlas/>.
3. This follows the PACPATH initiative (www.pacpath.org) that is targeting co-constructed approaches for addressing SDG 14 goals in Oceania. PACPATH was designed with and within PCCOS/SPC and USP to build on and expand existing networks and transdisciplinary workshops in which there is an opportunity to explore increased degrees of harmony between the understanding of sustainability, political and national interests, and the actions of organisations and people, from the South Pacific regional scale, to coastal community scale.
4. This also raises complex questions of *translations* so that actors can understand each other while acknowledging their different knowledge and norms (e.g. Sterling et al. 2017 regarding the construction of bio-cultural indicators).
5. Since local knowledge of IPLC is often place-specific and strongly linked to practice (e.g. Richards 1993), identity and sovereignty (Bambridge 2016; Bambridge and Le Meur 2018; Bambridge et al. 2021), its combined use with scientific data fosters (1) a spatially broader understanding of the environmental problems; (2) a dialogue around the desired future based on the needs and wishes of IPLC and (3) the design of interfaces between data and participatory methods.

6. <https://www.spc.int/pccos>.
7. www.pacificdata.org.
8. <https://www.spc.int/DigitalEarthPacific>.
9. <https://pacificdata.org/dashboard/17-goals-transform-pacific>.

References

Section 3.1. Potential eutrophication of European waters using satellite derived chlorophyll following the UN Sustainable Development Goal 14 framework

- Agusti S, Martinez-Ayala J, Regaudie-de-Gioux A, Duarte CM. 2017. Oligotrophication and metabolic slowing-down of a NW Mediterranean coastal ecosystem. *Front Mar Sci.* 4:432. doi:10.3389/fmars.2017.00432.
- Alamanos A, Linnane S. 2021. Estimating SDG indicators in data-scarce areas: the transition to the use of new technologies and multidisciplinary studies. *Earth.* 2:635–652. doi:10.3390/earth2030037.
- Anderson DM, Glibert PM, Burkholder JM. 2002. Harmful algal blooms and eutrophication: nutrient sources, composition, and consequences. *Estuaries.* 25:704–726. doi:10.1007/BF02804901.
- Andersen JH, Kallenbach E, Murray C, Ledang AB. 2016. Eutrophication in the Danish parts of the North Sea, Skagerrak and Kattegat 2006–2014. A literature-based status assessment. NIVA Denmark Report. <https://brage.bibsys.no/xmlui/handle/11250/2406499>.
- Anderson K, Ryan B, Sonntag W, Kavvada A, Friedl L. 2017. Earth observation in service of the 2030 agenda for sustainable development. *Geo Spatial Inf Sci.* 20:77–96. doi:10.1080/10095020.2017.1333230.
- Attila J, Kauppila P, Kallio KY, Alasalmi H, Keto V, Bruun E, Koponen S. 2018. Applicability of earth observation chlorophyll-a data in assessment of water status via MERIS – with implications for the use of OLCI sensors. *Remote Sens Environ.* 212:273–287. doi:10.1016/j.rse.2018.02.043.
- Balmer MB, Downing JA. 2011. Carbon dioxide concentrations in eutrophic lakes: undersaturation implies atmospheric uptake. *Inland Waters.* 1(2):125–132. doi:10.5268/IW-1.2.366.
- Baretta-Bekker H, Sell A, Marco-Rius F, Wischniewski J, Walsham P, Malin Mohlin L, Wesslander K, Ruitter H, Gohin F, Enserink L. 2015. The chlorophyll case study in the JMP NS/CS project. Document produced as part of the EU project: ‘Towards joint Monitoring for the North Sea and Celtic Sea’ (Ref: ENV/PP 2012/SEA).
- Brando VE, Sammartino M, Colella S, Bracaglia M, Di Cicco A, D’Alimonte D, Kajiyama T, Kaitala S, Attila J. 2021. Phytoplankton bloom dynamics in the Baltic Sea using a consistently reprocessed time series of multi-sensor reflectance and novel chlorophyll-a retrievals. *Remote Sens.* 13:3071.
- Breitburg D, Levin LA, Oschlies A, Grégoire M, Chavez FP, Conley DJ, Garçon V, Gilbert D, Gutiérrez D, Isensee K,

- Jacinto GS. 2018. Declining oxygen in the global ocean and coastal waters. *Science*. 359(6371):eaam7240.
- Brush MJ, Giani M, Totti C, Testa JM, Faganeli J, Ogrinc N, Kemp MW, Fondi-Umani S. 2020. Eutrophication, harmful algae, oxygen depletion, and acidification. *Coastal Ecosystems in Transition: A Comparative Analysis of the Northern Adriatic and Chesapeake Bay*, 75–104.
- Cai W, Hu X, Huang W. 2011. Acidification of subsurface coastal waters enhanced by eutrophication. *Nature Geosci*. 4:766–770. doi:10.1038/ngeo1297.
- Carvalho L, Mackay EB, Cardoso AC, Baatrup-Pedersen A, Birk S, Blackstock KL, Borics G, Borja A, Feld CK, Ferreira MT, et al. 2019. Protecting and restoring Europe's waters: an analysis of the future development needs of the water framework directive. *Sci Total Environ*. 658:1228–1238. doi:10.1016/j.scitotenv.2018.12.255.
- CMEMS OMI catalogue. 2020. ATLANTIC_OMI_HEALTH_OceanColour_anomalies https://resources.marine.copernicus.eu/?option=com_csw&view=details&product_id=ATLANTIC_OMI_HEALTH_OceanColour_anomalies.
- Colella S, Falcini F, Rinaldi E, Sammartino M, Santoleri R. 2016. Mediterranean ocean colour chlorophyll trends. *PLoS One*. 11(6):e0155756.
- Coppini G, Lyubartsev V, Pinardi N, Colella S, Santoleri R, Christiansen T. 2012. Chl-a trends in European seas estimated using ocean-colour products. *Ocean Science Discussions*. 9:1481–1518. doi:10.5194/osd-9-1481-2012.
- Cristina S, Icely J, Goela PC, DelValls TA, Newton A. 2015. Using remote sensing as a support to the implementation of the European Marine Strategy Framework Directive in SW Portugal. *Cont Shelf Res*. 108:169–177.
- Duarte CM, Regaudie-de-Gioux A, Arrieta JM, Delgado-Huertas A, Agusti S. 2013. The oligotrophic ocean is heterotrophic. *Ann Rev Mar Sci*. 5:551–569.
- Estoque RC. 2020. A review of the sustainability concept and the state of SDG monitoring using remote sensing. *Remote Sens*. 12:1770. doi:10.3390/rs12111770.
- Eurostat. 2021. Sustainable development in the European Union. Monitoring report on progress towards the SDGs in an EU context. ISBN 978-92-76-30698-6, Cat. No: KS-03-21-096-EN-N. doi:10.2785/195273.
- European Environment Agency. 2019a. *Marine Messages II' Navigating the course towards clean, healthy and productive seas through implementation of an ecosystem-based approach*. EEA Report No 17/2019 ISSN 1977-8449.
- European Environment Agency. 2019b. *Nutrient enrichment and eutrophication in Europe's seas. Moving towards a healthy marine environment* EEA Report No 14/2019 ISSN1977-8449.
- Friedland R, Macias DM, Cossarini G, Daewel U, Estournel C, Garcia-Gorriz E, Grizzetti B, Grégoire M, Gustafson B, Kalaroni S, et al. 2021. Effects of nutrient management scenarios on marine eutrophication indicators: a Pan-European, multi-model assessment in support of the Marine Strategy Framework Directive. *Front Mar Sci*. 8. doi:10.3389/fmars.2021.596126.
- Galloway JN, Townsend AR, Erisman JW, Bekunda M, Cai Z, Freney JR, Martinelli LA, Seitzinger SP, Sutton MA. 2008. Transformation of the nitrogen cycle: recent trends, questions, and potential solutions. *Science*. 320(5878):889–892. doi:10.1126/science.1136674.
- GEO Blue Planet. 2021. Global eutrophication monitoring in support of SDG 14. [accessed 2021 Jul 30]. <https://geoblueplanet.org/blue-planet-activities/eutrophication/>.
- Gohin F, Bryère P, Lefebvre A, Sauriau P-G, Savoye N, Vantrepotte V, Bozec Y, Cariou T, Conan P, Coudray S, et al. 2020. Satellite and in situ monitoring of chl-a, turbidity, and total suspended matter in coastal waters: experience of the year 2017 along the French coasts. *J Mar Sci Eng*. 8(9):665. doi:10.3390/jmse8090665.
- Gohin F, Saulquin B, Oger-Jeanerret H, Lozac'h L, Lampert L, Lefebvre A, Riou P, Bruchon F. 2008. Towards a better assessment of the ecological status of coastal waters using satellite-derived chlorophyll-a concentrations. *Remote Sens Environ*. 112:3329–3340.
- Gohin F, Van der Zande D, Tilstone G, Eleveld MA, Lefebvre A, Andrieux-Loyer F, Blauw AN, Bryère P, Devreker D, Garnesson P, et al. 2019. Twenty years of satellite and in situ observations of surface chlorophyll-a from the northern Bay of Biscay to the eastern English Channel. Is the water quality improving? *Remote Sens Environ*. 233:111343. doi:10.1016/j.rse.2019.111343.
- Groetsch PMM, Simis SGH, Eleveld MA, Peters SWM. 2016. Spring blooms in the Baltic Sea have weakened but lengthened from 2000 to 2014. *Biogeosciences*. 13(17):4959–4973. doi:10.5194/bg-13-4959-2016.
- Harvey ET, Kratzer S, Philipson P. 2015. Satellite-based water quality monitoring for improved spatial and temporal retrieval of chlorophyll-a in coastal waters. *Remote Sens Environ*. 158:417–430. doi:10.1016/j.rse.2014.11.017.
- Howarth RW, Anderson D, Cloern J, Elfring C, Hopkinson C, Lapointe B, Malone T, Marcus N, McGlathery K, Sharpley A, Walker D. 2000. Nutrient pollution of coastal rivers, bays and seas. *Issues Ecol*. 7:1–16.
- Howarth RW, Marino R. 2006. Nitrogen as the limiting nutrient for eutrophication in coastal marine ecosystems: evolving views over three decades. *Limnol Oceanogr*. 51(1, part 2). doi:10.4319/lo.2006.51.1_part_2.0364.
- Hutchinson GE. 1969. Eutrophication, past and present. In: *Eutrophication: Causes, Consequences, Correctives*, p. 17–26. National Academy of Sciences, Washington, DC.
- Jickells TD. 1998. Nutrient biogeochemistry of the coastal zone. *Science*. 281:217–222. doi:10.1126/science.281.5374.217.
- Karydis M, Kitsiou D. 2019. *Marine eutrophication: a global perspective*. Boca Raton, FL: CRC Press. 193 pp.
- Malone TC, Newton A. 2020. The globalization of cultural eutrophication in the coastal ocean: causes and consequences. *Front Mar Sci*. 7:670. doi:10.3389/fmars.2020.00670.
- Masó J, Serral I, Domingo-Marimon C, Zabala A. 2020. Earth observations for sustainable development goals monitoring based on essential variables and driver-pressure-state-impact-response indicators. *Int J Digital Earth*. 13(2):217–235. doi:10.1080/17538947.2019.1576787.
- Maúre EDR, Terauchi G, Ishizaka J, Clinton N, DeWitt M. 2021. Globally consistent assessment of coastal eutrophication. *Nat Commun*. 12:6142. doi:10.1038/s41467-021-26391-9.
- Nixon SW. 1995. Coastal marine eutrophication: a definition, social causes, and future concerns. *Ophelia*, 41:199–219.

- OSPAR ICG-EUT. Axe P, Clausen U, Leujak W, Malcolm S, Ruiter H, Prins T, Harvey ET. (2017). Eutrophication status of the OSPAR Maritime Area. Third integrated report on the eutrophication status of the OSPAR Maritime Area.
- Pardo S, Sathyendranath S, Platt T. 2021. 2.4 eutrophic and oligotrophic indicators for the North Atlantic Ocean. *J Oper Oceanogr.* 14(S1):1–185. doi:10.1080/1755876X.2021.1946240.
- Park Y, Ruddick K, Lacroix G. 2010. Detection of algal blooms in European waters based on satellite chlorophyll data from MERIS and MODIS. *Int J Remote Sens.* 31:6567–6583.
- Sathyendranath S, Brewin RJW, Brockmann C, Brotas V, Caltou B, Chuprin A, Cipollini P, Couto AB, Dingle J, Doerffer R, et al. 2019. An ocean-colour time series for use in climate studies: the experience of the ocean-colour climate change initiative (OC-CCI). *Sensors.* 19:4285. doi:10.3390/s19194285.
- Sathyendranath S, Platt T, Kovač Ž, Dingle J, Jackson T, Brewin RJW, Franks P, Marañoń E, Kulk G, Bouman HA. 2020. Reconciling models of primary production and photoacclimation. *Appl Opt.* 59:C100–C114. doi:10.1364/AO.386252.
- Schindler DW. 2006. Recent advances in the understanding and management of eutrophication. *Limnol Oceanogr.* 51:356–363.
- Smith VH. 2003. Eutrophication of freshwater and coastal marine ecosystems a global problem. *Environ Sci Pollut Res.* 10:126–139. doi:10.1065/espr2002.12.142.
- Seitzinger S, Mayorga E. 2016. Nutrient inputs from river systems to coastal waters. In IOC-UNESCO and UNEP, editors. Large marine ecosystems: status and trends. United Nations Environment Programme. Chapter 7.3. p. 179–195. <http://www.getfwap.org/publications/lmes-technical-report>.
- UNEP. 2021. Understanding the State of the Ocean: a global manual on measuring SDG 14.1.1, SDG 14.2.1 and SDG 14.5.1. Nairobi: UNEP.
- Van der Zande D, Lavigne H, Blauw A, Prins T, Desmit X, Eleveld M, Gohin F, Pardo S, Tilstone G, Cardoso Dos Santos J. 2019. Enhance coherence in eutrophication assessments based on chlorophyll, using satellite data as part of the EU project 'Joint monitoring programme of the eutrophication of the North Sea with satellite data' (Ref: DG ENV/MSFD Second Cycle/2016). Activity 2 Report.
- Van Meerssche E, Pinckney JL. 2019. Nutrient loading impacts on estuarine phytoplankton size and community composition: community-based indicators of eutrophication. *Estuaries Coasts.* 42:504–512. doi:10.1007/s12237-018-0470-z.
- VLIZ. 2019. Maritime boundaries geodatabase: maritime boundaries and exclusive economic zones (200NM), version 11. Flanders Marine Institute. doi:10.14284/386.
- Wallace RB, Baumann H, Grear JS, Aller RB, Gobler CJ. 2014. Coastal ocean acidification: the other eutrophication problem. *Estuarine Coastal Shelf Sci.* 148:1–13. doi:10.1016/j.ecss.2014.05.027.
- Williams PJLB, Quay PD, Westberry TK, Behrenfeld MJ. 2013. The oligotrophic ocean is autotrophic. *Ann Rev Mar Sci.* 5:535–549.
- Zingone A, Philips EJ, Harrison PJ. 2010. Multiscale variability of twenty-two coastal phytoplankton time series: a global scale comparison. *Estuaries Coasts.* 33:224–229. doi:10.1007/s12237-009-9261-x.

Section 3.2. Trends in nutrient and chlorophyll a concentrations from FerryBox transect time series in the Baltic Sea

- Andersen JH, Carstensen J, Conley DJ, Dromph C, Fleming-Lehtinen V, Gustafsson BG, Josefson AB, Norkko A, Villnäs A, Murray C. 2017. Long-term temporal and spatial trends in eutrophication status of the Baltic Sea. *Biol Rev.* 92:135–149. doi:10.1111/brv.12221.
- Conley DJ, Björck S, Bonsdorff E, Carstensen J, Destouni G, Gustafsson BG, Hietanen S, Kortekaas M, Kuosa H, Meier HEM, et al. 2009. Hypoxia-related processes in the Baltic Sea. *Environ Sci Technol.* 43(10):3412–3420. doi:10.1021/es802762a.
- Dalsgaard T, De Brabandere L, Hall POJ. 2013. Denitrification in the water column of the central Baltic Sea. *Geochim Cosmochim Acta.* 106:247–260. doi:10.1016/j.gca.2012.12.038.
- Danielsson Å, Papush L, Rahm L. 2008. Alterations in nutrient limitations – scenarios of a changing Baltic Sea. *J Mar Sys.* 73(3–4):263–283. doi:10.1016/j.jmarsys.2007.10.015.
- Deutsch B, Forster S, Wilhelm M, Dippner JW, Voss M. 2010. Denitrification in sediments as a major nitrogen sink in the Baltic Sea: an extrapolation using sediment characteristics. *Biogeosciences.* 7(10):3259–3271. doi:10.5194/bg-7-3259-2010.
- Egge JK, Aksnes DL. 1992. Silicate as regulating nutrient in phytoplankton competition. *Mar Ecol Prog Ser.* 83(2–3):281–289. doi:10.3354/meps083281.
- Farcy P, Durand D, Charria G, Painting SJ, Tamminen T, Collingridge K, Grémare AJ, Delauney L, Puillat I. 2019. Toward a European coastal observing network to provide better answers to science and to societal challenges; the JERICO research infrastructure. *Front Mar Sci.* 6:529. doi:10.3389/fmars.2019.00529.
- Fleming-Lehtinen V, Andersen JH, Carstensen J, Łysiak-Pastuszek E, Murray C, Pyhälä M, Laamanen M. 2015. Recent developments in assessment methodology reveal that the Baltic Sea eutrophication problem is expanding. *Ecol Indic.* 48:380–388. doi:10.1016/j.ecolind.2014.08.022.
- Fleming-Lehtinen V, Laamanen M, Kuosa H, Hahti H, Olsonen R. 2008. Long-term development of inorganic nutrients and chlorophyll α in the open Northern Baltic Sea long-term development of inorganic nutrients and chlorophyll a in the open Northern Baltic Sea. *Ambio.* 37:86–92. doi:10.1579/0044-7447.
- Fleming V, Kaitala S. 2006. Phytoplankton spring bloom intensity index for the Baltic Sea estimated for the years 1992 to 2004. *Hydrobiologia.* 554:57–65. doi:10.1007/s10750-005-1006-7.
- García-García LM, Sivyer D, Devlin M, Painting S, Collingridge K, van der Molen J. 2019. Optimizing monitoring programs: a case study based on the OSPAR eutrophication assessment for UK waters. *Front Mar Sci.* 5:503. doi:10.3389/fmars.2018.00503.
- Graneli E, Wallstrom K, Larsson U, Graneli W, Elmgren R. 1990. Nutrient limitation of primary production in the Baltic Sea area. *Ambio.* 19(3):142–151. doi:10.2307/4313680.
- Grasshoff K, Kremling K, Ehrhardt M. 1999. Methods of seawater analysis. 3rd ed. New York: Wiley-VCH.

- Gustafsson BG, Schenk F, Blenckner T, Eilola K, Meier HEM, Müller-Karulis B, Neumann T, Ruoho-Airola T, Savchuk OP, Zorita E. 2012. Reconstructing the development of Baltic Sea eutrophication 1850–2006. *Ambio*. 41(6):534–548. doi:10.1007/s13280-012-0318-x.
- Gustafsson E, Savchuk OP, Gustafsson BG, Müller-Karulis B. 2017. Key processes in the coupled carbon, nitrogen, and phosphorus cycling of the Baltic Sea. *Biogeochemistry*. 134(3):301–317. doi:10.1007/s10533-017-0361-6.
- HELCOM. 2017. Manual for marine monitoring in the COMBINE program of HELCOM. Last updated: July 2017. <https://helcom.fi/action-areas/monitoring-and-assessment/monitoring-guidelines/combine-manual/>.
- HELCOM. 2018a. State of the Baltic Sea – Second HELCOM holistic assessment, 2011–2016. Baltic Sea Environment Proceedings 155. <http://stateofthebalticsea.helcom.fi/pressures-and-their-status/hazardous-substances/>.
- HELCOM. 2018b. HELCOM thematic assessment of eutrophication 2011–2016. Baltic Sea Environment Proceedings 156. <http://www.helcom.fi/baltic-sea-trends/holistic-assessments/state-of-the-baltic-sea-2018/reports-and-materials/>.
- Humborg C, Smedberg E, Medina MR, Mörth CM. 2008. Changes in dissolved silicate loads to the Baltic Sea – the effects of lakes and reservoirs. *J Mar Sys*. 73(3–4):223–235. doi:10.1016/j.jmarsys.2007.10.014.
- Kahru M, Elmgren R. 2014. Multidecadal time series of satellite-detected accumulations of cyanobacteria in the Baltic Sea. *Biogeosciences*. 11:3619–3633. doi:10.5194/bg-11-3619-2014.
- Klais R, Tamminen T, Kremp A, Spilling K, Olli K. 2011. Decadal-scale changes of dinoflagellates and diatoms in the anomalous Baltic Sea spring bloom. *PLoS One*. 6(6): e21567. doi:10.1371/journal.pone.0021567.
- Köuts M, Maljutenko I, Elken J, Liu Y, Hansson M, Viktorsson L, Raudsepp U. 2021. Recent regime of persistent hypoxia in the Baltic Sea. *Environ Res Commun*. 3:075004. doi:10.1088/2515-7620/ac0cc4.
- Köuts M, Maljutenko I, Liu Y, Raudsepp U. 2021. 2.5 Nitrate, ammonium and phosphate pools in the Baltic Sea. In: Copernicus Marine Service Ocean State Report, Issue 5. *J Oper Oceanogr*. 14(suppl. 1). doi:10.1080/1755876X.2021.1946240.
- Lehtoranta J, Savchuk OP, Elken J, Dahlbo K, Kuosa H, Raateoja M, Kauppila P, Räike A, Pitkänen H. 2017. Atmospheric forcing controlling inter-annual nutrient dynamics in the open Gulf of Finland. *J Mar Sys*. 171:4–20. doi:10.1016/j.jmarsys.2017.02.001.
- Murray CJ, Müller-Karulis B, Carstensen J, Conley DJ, Gustafsson BG, Andersen JH. 2019. Past, present and future eutrophication status of the Baltic Sea. *Front Mar Sci*. 6:2. doi:10.3389/fmars.2019.00002.
- Ohlndieck U, Stühr A, Siegmund H. 2000. Nitrogen fixation by diazotrophic cyanobacteria in the Baltic Sea and transfer of the newly fixed nitrogen to picoplankton organisms. *J Mar Sys*. 25(3–4):213–219. doi:10.1016/S0924-7963(00)00016-6.
- Olofsson M, Klawonn I, Karlson B. 2021. Nitrogen fixation estimates for the Baltic Sea indicate high rates for the previously overlooked Bothnian Sea. *Ambio*. 50(1):203–214. doi:10.1007/s13280-020-01331-x.
- Pilkaityte R, Razinkovas A. 2007. Seasonal changes in phytoplankton composition and nutrient limitation in a shallow Baltic lagoon. *Boreal Environ Res*. 12(5):551–559.
- Raateoja M, Kuosa H, Hällfors S. 2011. Fate of excess phosphorus in the Baltic Sea: a real driving force for cyanobacterial blooms? *J Sea Res*. 65(2):315–321. doi:10.1016/j.seares.2011.01.004.
- Raateoja M, Hällfors H, Kaitala S. 2018. Vernal phytoplankton bloom in the Baltic Sea: intensity and relation to nutrient regime. *J Sea Res*. 138:24–33. doi:10.1016/j.seares.2018.05.003.
- Räike A, Taskinen A, Knuuttila S. 2020. Nutrient export from Finnish rivers into the Baltic Sea has not decreased despite water protection measures. *Ambio*. 49(2):460–474. doi:10.1007/s13280-019-01217-7.
- Rantajarvi E. 2003. Alg@line in 2003: 10 years of innovative plankton monitoring and research and operational information service in the Baltic Sea. Meri Report Series of the Finnish Institute of Marine Research. 48.
- Rantajarvi E, Pitkänen H, Korpinen S, Nurmi M, Ekeboom J, Liljaniemi P, Cederberg T, Suomela J, Paavilainen P, Lahtinen T. 2020. Manual for marine monitoring in Finland 2020–2026. Suomen ympäristökeskuksen raportteja. 47 (in Finnish), 219 pages.
- Rönnerberg C, Bonsdorff E. 2004. Baltic Sea eutrophication: area-specific ecological consequences. *Hydrobiologia*. 514(2002):227–241. doi:10.1023/B:HYDR.0000019238.84989.7f.
- Ruokanen L, Kaitala S, Fleming V, Maunula P. 2003. Alg@line-joint operational unattended phytoplankton monitoring in the Baltic Sea. In: Dahlin H, Flemming NC, Nittis K, Petersson SE, editors. Elsevier oceanography series. Vol. 69. Elsevier; p. 519–522. doi:10.1016/S0422-9894(03)80083-1.
- Savchuk OP. 2018. Large-scale nutrient dynamics in the Baltic Sea, 1970–2016. *Front Mar Sci*. 5:1–20. doi:10.3389/fmars.2018.00095.
- Snoeijs-Leijonmalm P, Schubert H, Radziejewska T. 2017. Biological oceanography of the Baltic Sea. Springer Science & Business Media, Dordrecht.
- Spilling K, Olli K, Lehtoranta J, Kremp A, Tedesco L, Tamelander T, Klais R, Peltonen H, Tamminen T. 2018. Shifting diatom – dinoflagellate dominance during spring bloom in the Baltic Sea and its potential effects on biogeochemical cycling. *Front Mar Sci*. 5:327. doi:10.3389/fmars.2018.00327.
- Spilling K, Tamminen T, Andersen T, Kremp A. 2010. Nutrient kinetics modeled from time series of substrate depletion and growth: dissolved silicate uptake of Baltic Sea spring diatoms. *Mar Biol*. 157(2):427–436. doi:10.1007/s00227-009-1329-4.
- Stal LJ, Albertano P, Bergman B, Von Bröckel K, Gallon JR, Hayes PK, Sivonen K, Walsby AE. 2003. BASIC: Baltic Sea cyanobacteria. An investigation of the structure and dynamics of water blooms of cyanobacteria in the Baltic Sea – responses to a changing environment. *Cont Shelf Res*. 23(17–19):1695–1714. doi:10.1016/j.csr.2003.06.001.
- Tallberg P, Heiskanen AS, Niemistö J, Hall POJ, Lehtoranta J. 2017. Are benthic fluxes important for the availability of Si in the Gulf of Finland? *J Mar Sys*. 171:89–100. doi:10.1016/j.jmarsys.2017.01.010.
- Tamminen T, Andersen T. 2007. Seasonal phytoplankton nutrient limitation patterns as revealed by bioassays over Baltic Sea gradients of salinity and eutrophication. *Mar*

- Ecol Prog Ser. 340(1971):121–138. doi:10.3354/meps340121.
- Wasmund N, Kownacka J, Göbel J, Jaanus A, Johansen M, Jurgensone I, Lehtinen S, Powilleit M. 2017. The diatom/dinoflagellate index as an indicator of ecosystem changes in the Baltic Sea 1. Principle and handling instruction. *Front Mar Sci.* 4:1–13. doi:10.3389/FMARS.2017.00022.
- Wasmund N, Nausch G, Feistel R. 2013. Silicate consumption: an indicator for long-term trends in spring diatom development in the Baltic Sea. *J Plankton Res.* 35(2):393–406. doi:10.1093/plankt/fbs101.
- Zdun A, Stoń-Egiert J, Ficek D, Ostrowska M. 2021. Seasonal and spatial changes of primary production in the Baltic Sea (Europe) based on in situ measurements in the period of 1993–2018. *Front Mar Sci.* 7. doi:10.3389/fmars.2020.604532.
- Section 3.3. Copernicus marine sea surface temperature and chlorophyll-a indicators for two Pacific Islands: a co-construction monitoring framework for an integrated, transdisciplinary, multi-scale approach**
- Andréfouët S, Van Wynsberge S, Kabbadj L, Wabnitz CC, Menkès C, Tamata T, Pahuatini M, Tetairekie I, Teaka I, Scha TA, et al. 2018. Adaptive management for the sustainable exploitation of lagoon resources in remote islands: lessons from a massive El Niño-induced giant clam bleaching event in the Tuamotu atolls (French Polynesia). *Environ Conserv.* 45(1):30–40.
- Aswani S, Hamilton RJ. 2004. Integrating indigenous ecological knowledge and customary sea tenure with marine and social science for conservation of bumphead parrotfish (*Bolbometopon muricatum*) in the Roviana Lagoon, Solomon Islands. *Environ Conserv.* 31:69–83.
- Aswani S, Lauer M. 2006. Incorporating fishermen's local knowledge and behavior into geographical information systems (GIS) for designing marine protected areas in Oceania. *Hum Organ.* 65:81–102.
- Bambridge T, editor. 2016. *The Rahu: legal pluralism in Polynesian traditional management of resources and territories.* Canberra: ANU Press.
- Bambridge T, D'Arcy P, Mawyer A. 2021. *Oceanian sovereignty: rethinking conservation in a sea of islands, Pacific conservation biology.* CSIRO Publishing. doi:10.1071/PC20026.
- Bambridge T, Le Meur P-Y. 2018. Savoirs locaux et biodiversité aux îles Marquises: don, pouvoir et perte. *Revue D'anthropologie des Connaissances.* 12(1):29–55.
- Behera SK, Doi T, Luo J-J. 2021. 3 – air–sea interaction in tropical Pacific: the dynamics of El Niño/southern oscillation (SKBT-T and EA-SI Behera, editors). Elsevier; p. 61–92. doi:10.1016/B978-0-12-818156-0.00005-8.
- Berghthaller H, Emmett R, Johns-Putra A, Kneitz A, Lidström S, McCorristine S, Pérez Ramos I, Phillips D, Rigby K, Robin L. 2014. Mapping common ground: ecocriticism, environmental history, and the environmental humanities. *Environ Human.* 5:261–276.
- de Boisseson E, Balmaseda M, Mayer M, Zuo H. 2022. Section 3.3: a series of marine heatwave events in the northeast Pacific in 2020, in Copernicus Ocean State Report, issue 6. *J Oper Oceanogr.* this issue.
- Castillo KD, Lima FP. 2010. Comparison of in situ and satellite-derived (MODIS-aqua/terra) methods for assessing temperatures on coral reefs. *Limnol Oceanogr Methods.* 8:107–117.
- Celliers L, Costa M, Williams D, Rosendo S. 2021. The 'last mile' for climate data supporting local adaptation. *Global Sustain.* 4:E14. doi:10.1017/sus.2021.12.
- Chambers JM, Wyborn C, Ryan ME, Reid RS, Riechers M, Serban A, Bennett NJ, Cvitanovic C, Fernández-Giménez ME, Galvin KA, Goldstein BE. 2021. Six modes of co-production for sustainability. *Nat Sustain.* 4:983–996. doi:10.1038/s41893-021-00755-x.
- Cheype A, Fiat S, Pelletier B, Ganachaud A, Grelet J, Varillon D, Magron F, Hocdé R. 2015. Système d'information de l'observatoire ReefTEMPS: données de température côtière du Pacifique Sud et Sud-Ouest. *JDEV 2015: Journées Nationales du DEveloppement Logiciel de l'Enseignement Supérieur et Recherche,* Juin 2015, Bordeaux, France.
- Chifflet S, Gérard P, Fichez R. 2004. *Sciences de la Mer. Biologie Marine N°6. Manuel d'analyses chimiques dans l'eau de mer, Nouméa: IRD, 2004, multigr. (Sciences de la Mer. Biologie Marine. Notes Techniques; 6, 82 pages).*
- Claar DC, Cobb KM, Baum JK. 2020. In situ and remotely sensed temperature comparisons on a central Pacific atoll. *Coral Reefs.* 38(6):1343–1349.
- Claudet J, Bopp L, Cheung WWLL, Devillers R, Escobar-Briones E, Haugan P, Heymans JJ, Masson-Delmotte V, Matz-Luck N, Miloslavich P, et al. 2020. A roadmap for using the UN decade of ocean science for sustainable development in support of science, policy, and action. *One Earth.* 2:34–42.
- Cocquempot L, Delacourt C, Paillet J, Riou P, Aucan J, Castelle B, Charria G, Claudet J, Conan P, Coppola L, et al. 2019. Coastal ocean and nearshore observation: a French case study. *Front Mar Sci.* 6(324):17. doi:10.3389/fmars.2019.00324.
- CMEMS. 2021a. Copernicus marine service ocean monitoring indicator framework: global map of chl-a trend for 1997-2019, GLOBAL_OMI_HEALTH_OceanColour_oligo_spg_area_mean. <https://marine.copernicus.eu/access-data/ocean-monitoring-indicators/global-ocean-chlorophyll-trend>.
- CMEMS. 2021b. Global mean sea surface temperature, Copernicus Marine Service (CMEMS) Ocean Monitoring Indicator Framework. <https://marine.copernicus.eu/access-data/ocean-monitoring-indicators/global-ocean-anomaly-time-series-sea-surface-temperature>.
- Colglazier EW. 2018. The sustainable development goals: roadmaps to progress. *Sci Dipl.* 7. <http://www.sciencediplomacy.org/editorial/2018/sdg-roadmaps>.
- Cravatte S, Delcroix T, Zhang D, McPhaden M, Jeloup J. 2009. Observed freshening and warming of the western Pacific warm pool. *Clim Dyn.* doi:10.1007/s00382-009-0526-7.
- Dandonneau Y, Charpy L. 1985. An empirical approach to the island mass effect in the south tropical Pacific based on sea surface chlorophyll concentration. *Deep-Sea Res A.* 29:953–965.
- Dayan H, McAdam R, Masina RS, Speich S. 2022. Section 1.7: diversity of marine heatwave trends across the